Ocean Wind and Wave Parameter Estimation From Ship-Borne X-Band Marine Radar Data

by

©Xinlong Liu, B. Eng., M. Eng.

A thesis submitted to the

School of Graduate Studies

in partial fulfilment of the

requirements for the degree of

Doctor of Philosophy

Faculty of Engineering and Applied Science

Memorial University of Newfoundland

May 2018

St. John's Newfoundland and Labrador

Abstract

Ocean wind and wave parameters are important for the study of oceanography, on- and off-shore activities, and the safety of ship navigation. Conventionally, such parameters have been measured by *in-situ* sensors such as anemometers and buoys. During the last three decades, sea surface observation using X-band marine radar has drawn wide attention since marine radars can image both temporal and spatial variations of the sea surface. In this thesis, novel algorithms for wind and wave parameter retrieval from X-band marine radar data are developed and tested using radar, anemometer, and buoy data collected in a sea trial off the east coast of Canada in the North Atlantic Ocean.

Rain affects radar backscatter and leads to less reliable wind parameters measurements. In this thesis, algorithms are developed to enable reliable wind parameters measurements under rain conditions. Firstly, wind directions are extracted from rain-contaminated radar data using either a 1D or 2D ensemble empirical mode decomposition (EEMD) technique and are seen to compare favourably with an anemometer reference. Secondly, an algorithm based on EEMD and amplitude modulation (AM) analysis to retrieve wind direction and speed from both rain-free and rain-contaminated X-band marine radar images is developed and is shown to be an improvement over an earlier 1D spectral analysis-based method.

For wave parameter measurements, an empirical modulation transfer function (MTF) is required for traditional spectral analysis-based techniques. Moreover, the widely used signal-to-noise ratio (SNR)-based method for significant wave height (H_S) estimation may not always work well for a ship-borne X-band radar, and it requires external sensors for calibration. In this thesis, two methods are first presented for H_S estimation from X-band marine radar data. One is an EEMD-based method, which enables satisfactory H_S measurements obtained from a ship-borne radar. The other is a modified shadowing-based method, which enables H_S measurements without the inclusion of external sensors. Furthermore, neither method requires the MTF. Finally, an algorithm based on the Radon

transform is proposed to estimate wave direction and periods from X-band marine radar images with satisfactory results.

Acknowledgements

Time flies. Four years of PhD study at Memorial University of Newfoundland is coming to an end. At the completion of my doctoral dissertation, I would like to express my sincere gratitude to those who gave me help and support in my PhD study.

First, I would like to express my deepest gratitude to my supervisors, Dr. Weimin Huang and Dr. Eric Gill. They continuously provided their professional guidance to me. Their attitude and enthusiasm for research inspired me all the time. When I had concerns, their doors were always open to me. They encouraged me to overcome difficulties in my research. They helped me in every aspect of my life. It is a great honour to be a member of their research group. My work was supported in part by the Natural Sciences and Engineering Research Council of Canada (NSERC) Discovery Grants to W. Huang (NSERC 402313-2012, RGPIN-2017-04508, and RGPAS-2017-507962) and E. W. Gill (NSERC RGPIN-2015-05289), the Memorial University Seed, Bridge and Multidisciplinary Grant (20151381) to W. Huang, and an Atlantic Innovation Fund Award (E. W. Gill, principal investigator). I would also like to thank Dr. E. Thornhill at Defence Research and Development Canada (DRDC) for the provision of radar, anemometer, and buoy data.

Next, I would like to thank all the members of our research group. I benefited a lot from our group meetings and discussions. I would also like to thank all my friends I met in St. John's. They made my life here colourful and brought me a lot of happiness.

Finally, I would like to thank my family for their love and continuous support to me. Thank you to my girlfriend, Yue Ma, who accompanied me all the time through my PhD study, making my life full of sunshine.

Contents

List of Figures

List of Tables

List of Symbols

The page numbers here indicate the place of first significant reference. Only important symbols are explicitly referenced below, and all the symbol definitions are obvious from the context.

f_o the optical flow, i.e., the local wind velocity vector (p. 12)

θ the azimuth direction (p. 14)

σ_{wDir_θ} the average radar backscatter intensity as a function of θ (p. 14)

σ_{wSpd} the average radar backscatter intensity of one radar image (p. 15)

w_{Spd} the wind speed (p. 19)

$r_{p_{\max}}$ the peak of smoothed maximum range distances (p. 19)

L_S the selected intensity level (p. 19)

$I_{m,n}$ the image intensity at range index m and azimuth index n (p. 21)

$T_{m,n}$ the texture of the radar image at range index m and azimuth index n (p. 21)

w_{Dir} the wind direction (p. 22)

$\sigma_{\exp}$ the expectancy of radar image intensity levels (p. 23)

H_S the significant wave height (p. 23)

F_{BGN_T} the total spectral energy of background noise (p. 24)

k the wavenumber (p. 25)

$I_n(m)$ the mth pixel intensity in the nth column of a polar radar image (p. 25)

$E_n(k)$ the wavenumber spectrum of the nth column of a polar radar image (p. 25)

S_n the integral of spectral values over the wavenumber range [0.01, 0.2] for the nth column of a polar radar image (p. 25)

S_T the spectral integration for one radar image (p. 26)

$\vec{k}$ the wavenumber vector (p. 29)

ω the angular frequency (p. 29)

$F_F^{(3)}(\vec{k},\omega)$ the 3D wave-related image spectrum (p. 29)

$T_M(\vec{k})$ the modulation transfer function (p. 29)

$F_W^{(3)}(\vec{k},\omega)$ the 3D wave spectrum (p. 29)

$F_W^{(2)}(\vec{k})$ the 2D wavenumber wave spectrum (p. 29)

$E^{(2)}(\omega,\theta)$ the 2D frequency-directional wave spectrum (p. 29)

$S(\omega)$ the 1D frequency wave spectrum (p. 30)

$F_I^{(3)}(\vec{k},\omega)$ the 3D image spectrum (p. 31)

$F_H^{(3)}(\vec{k},\omega)$ the 3D high harmonic spectrum (p. 31)

$F_{BGN}^{(3)}(\vec{k},\omega)$ the 3D background noise spectrum (p. 31)

SNR the signal-to-noise ratio of a radar image sequence (p. 31)

$\vec{U}$ the surface current vector (p. 34)

g the acceleration due to gravity (p. 34)

r_a the range (p. 50)

h_{ant} the antenna height (p. 50)

$\widetilde{\psi}(r_a)$ the range-dependent depression angle (p. 50)

$\psi(r_a, \theta)$ the local depression angle (p. 50)

$\varphi(r_a, \theta)$ the local ocean surface tilt angle (p. 50)

$I(m, n)$ the polar radar image at row m and column n (p. 52)

H_i the ith discrete directional first derivative operator (p. 52)

I_{E_i} the edge image along the ith direction (p. 52)

I_{T_i} the ith thresholded edge image (p. 52)

I_F the overall edge image (p. 52)

$F_H(\eta)$ the statistical distribution of edge pixel gray level values η (p. 53)

τ_S the shadow threshold (p. 53)

σ^A_{RMS} the average RMS surface slope (p. 53)

T_{m02} the average zero-crossing wave period (p. 53)

d_w the water depth (p. 54)

λ the wavelength of ocean waves (p. 54)

I_{TS} the 2D time-space image sequence (p. 56)

v_j the jth eigenvector of the matrix $I_{TS}I^T_{TS}$ (p. 56)

z_k the kth principal component of the 2D time-space image sequence I_{TS} (p. 56)

$std(z_k)$ the standard deviation of the kth principal component (p. 56)

f_p the peak wave frequency (p. 57)

T_p the peak wave period (p. 57)

z'_q the qth rotated principal component of the 2D time-space image sequence I_{TS} (p. 59)

$std(z'_q)$ the standard deviation of the qth rotated principal component (p. 59)

I a polar radar image with M rows and N columns (p. 69)

G_j the jth IMF component of the 1D-EEMD of I, with j ranging from 1 to J-1, J-1 being the number of IMF components (p. 70)

G_J the residual component of the 1D-EEMD of I (p. 70)

σ_θ the standard deviation of one IMF component or the combination of several IMF components as a function of θ (p. 70)

$H_{j,k}$ the kth IMF component of G_j after the application of EEMD to each row of G_j, with k ranging from 1 to K-1, K-1 being the number of IMF components (p. 71)

$H_{j,K}$ the residual component of G_j after the application of EEMD to each row of G_j (p. 71)

C_l the lth IMF component of the 2D-EEMD of I, with l ranging from 1 to the minimum of J-1 and K-1 (p. 71)

$C_{\min(J,K)}$ the residual component of the 2D-EEMD of I (p. 71)

$a_1(\sim,n)$ the AM part of $G_1(\sim,n)$ (p. 91)

R_n the average of the residual in each azimuth direction (p. 91)

$A_{1,n}$ the average of the AM part of the first IMF in each azimuth direction (p. 92)

m_a the average of the AM part of the first IMF in one radar image (p. 92)

m_r the average of the residual in one radar image (p. 93)

M_{com} the combination of m_a and m_r (p. 93)

I_{sub} the subarea of a polar radar image with M' rows and N' columns (p. 113)

$D_j(\sim, n')$ the jth IMF of $I_{sub}(\sim, n')$ (p. 114)

$R(\sim, n')$ the residual of $I_{sub}(\sim, n')$ (p. 114)

$A_j(\sim, n')$ the AM part of $D_j(\sim, n')$ (p. 114)

$F_j(\sim, n')$ the FM part of $D_j(\sim, n')$ (p. 114)

v_D dominant wave speed (p. 132)

λ_M mean wavelength (p. 133)

List of Abbreviations

SARSynthetic Aperture Radar (p. 1)

HFHigh Frequency (p. 1)

RCSRadar Cross Section (p. 2)

EEMDEnsemble Empirical Mode Decomposition (p. 3)

IMFIntrinsic Mode Function (p. 3)

AMAmplitude Modulation (p. 3)

FMFrequency Modulation (p. 3)

3DThree-Dimensional (p. 3)

DFTDiscrete Fourier Transform (p. 3)

MTFModulation Transfer Function (p. 3)

RTRadon Transform (p. 3)

H_S Significant Wave Height (p. 4)

SNRSignal-to-Noise Ratio (p. 4)

1DOne-Dimensional (p. 5)

2DTwo-Dimensional (p. 5)

LGMLocal Gradients Method (p. 9)

NNNeural Network (p. 9)

NRCSNormalized Radar Cross Section (p. 9)

CCFCross-Correlation Function (p. 9)

CSCross-Spectrum (p. 9)

OFMOptical Flow Motion (p. 12)

CFCurve Fitting (p. 14)

RMSRoot-Mean-Square (p. 15)

ZPPZero-Pixel Percentage (p. 17)

ILSIntensity Level Selection (p. 18)

FOVField of View (p. 19)

TAITexture-Analysis Incorporated (p. 21)

PDFProbability Distribution Function (p. 22)

BGNBackground Noise (p. 23)

SASpectral Analysis (p. 24)

FPSOFloating Production and Storage Offshore (p. 32)

ANNArtificial Neural Network (p. 33)

MLPMultilayer Perceptrons (p. 33)

LSLeast-Squares (p. 34)

ARPMAdaptive Recursive Positioning Method (p. 37)

CWTContinuous Wavelet Transform (p. 40)

ApFFTAll-Phase Fast Fourier Transform (p. 45)

GFCGullfaks C (p. 49)

CSRCartesian Start Range (p. 49)

GLCMGray Level Co-Occurrence Matrix (p. 49)

SVRSupport Vector Regression (p. 55)

MAEMean Absolute Error (p. 55)

MSEMean Square Error (p. 55)

EOFEmpirical Orthogonal Function (p. 55)

PCPrincipal Component (p. 55)

MEMMaximum Entropy Method (p. 55)

PSDPower Spectral Density (p. 55)

REOFRotated Empirical Orthogonal Function (p. 58)

EMDEmpirical Mode Decomposition (p. 66)

HHTHilbert-Huang Transform (p. 67)

DRDCDefence Research and Development Canada (p. 72)

HPPHigh-Pixel Percentage (p. 74)

HCDHigh-Clutter Direction (p. 95)

HCDPHigh-Clutter Direction Percentage (p. 95)

Chapter 1

Introduction

1.1 Background

Ocean wind and wave parameters are important for the study of oceanography, on- and off-shore activities, and the safety of ship navigation. Conventionally, anemometers have been widely used for wind measurements, and wave information has been derived from the time series of buoy-recorded sea surface elevation. However, wind measurements from anemometers may be affected by the structure and motion of the platform [1], and the deployment of buoys may be limited, for example, by the availability of mooring facilities and by meteorological conditions [2]. Also, of course, anemometers and buoys deliver only point measurements and cannot provide information on the spatial variability of the sea state. During the last several decades, ocean wind and wave measurements using remote-sensing instruments such as synthetic aperture radar (SAR) [3–5] and high frequency (HF) radar [6–8] have been rapidly developed. However, while SAR images contain spatial information, they do not provide the temporal evolution of the sea surface. Also, HF radar installations may require significant tracts of coastline, and the cost of deployment and maintenance can be high. Recently, due to the capability of scanning the sea surface with high temporal and spatial resolution, land-based or ship-borne X-band nautical radar has also drawn wide attention in wind and wave measurements. Since

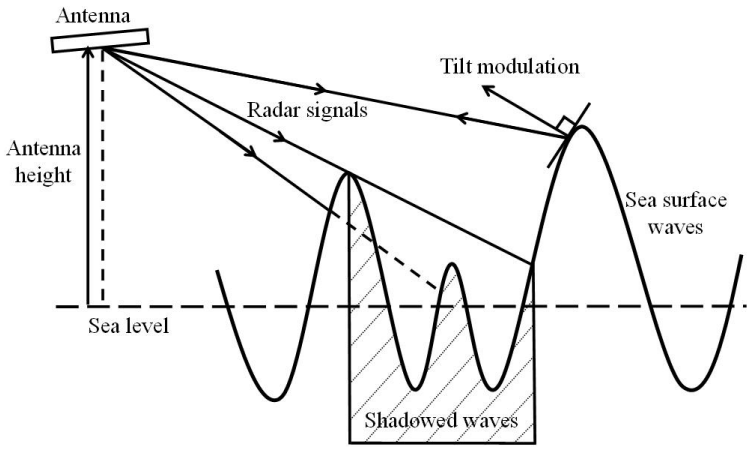

Fig. 1.1 Shadowing and tilt modulation.

X-band nautical radar is commonly installed on ships for navigation purposes, sea surface observation using such radars has become promising.

The radar signature of the sea surface, also known as sea clutter, is undesirable and generally suppressed for navigation purposes, but it is useful in monitoring sea state. At grazing incidence, X-band radar backscatter is mainly caused by Bragg resonance as a result of interactions between microwaves and the sea surface high frequency gravity-capillary waves induced by local winds and influenced by gravitational and surface tension restoring forces [9]. Longer waves become visible in radar images due to their modulations of the short waves in a non-linear process mainly affected by hydrodynamic modulation, tilt modulation, and shadowing [10]. Thus, the estimation of directional wave spectra and integrated sea state parameters is viable from an analysis of the time series of X-band nautical radar sea surface images [11]. Shadowing and tilt modulations are depicted in Fig.1.1. Wind information can be retrieved from radar images due to the dependence of the radar cross section (RCS) on wind speed [12] and the angle between radar look direction and wind direction [13]. Although X-band radar technology for measuring wind parameters [14–19], sea surface currents [20–23] and waves [24–28] is relatively mature, and corresponding products are commercially available, robust algorithms for wind and wave sensing using X-band radar are still evolving.

1.2 Motivation and Objectives

X-band marine radar can provide good wind measurements in the absence of rain. However, in the presence of rain, sea surface roughness changes due to the raindrops impinging the ocean [29, 30], and volume scattering and attenuation due to the raindrops in the atmosphere [31] will also affect the radar backscatter. These effects lead to less reliable wind measurements. Generally, radar images which are contaminated by rain are identified and removed from the data before the application of algorithms designed to extract wind information [15, 17]. Since rainfall is a common event on the ocean, it is necessary to develop techniques for wind parameter extraction from rain-contaminated radar images. A technique called ensemble empirical mode decomposition (EEMD) was mainly developed for time-frequency analysis of non-linear and non-stationary data [32–35], which is the case for X-band marine radar data. By using EEMD, such data can be adaptively decomposed into a finite number of disparate narrow-banded intrinsic mode functions (IMFs), which can be further separated into amplitude modulation (AM) and frequency modulation (FM) portions by a normalization scheme [36]. In this thesis, the first objective is to develop EEMD-based algorithms for the extraction of wind direction and speed from both rain-free and rain-contaminated X-band marine radar data.

Analysis of X-band marine radar image sequences based on the three-dimensional (3D) discrete Fourier transform (DFT) was first proposed in [9]. Since then, X-band marine radar has been widely used for the estimation of ocean wave parameters [37, 38]. A commercial wave monitoring system called WaMoS II has also been developed [2, 39]. Since wave parameters are retrieved based on radar-derived wave spectra, an empirical modulation transfer function (MTF) needs to be applied. However, since the MTF varies for different radar systems and different environments, a method independent of the MTF for wave parameter measurements is needed. The Radon transform (RT) can be used to detect linear features in a noisy digital image [40], and this makes it especially suitable for the detection of wave signatures in X-band marine radar images. The RT

has been used in SAR applications for detecting ship wakes [41] and geographical structures [42]. It has also been applied to X-band marine radar images to analyze internal wave signatures [43, 44]. In [45], surface wave parameters were extracted from X-band marine radar images using the RT, but only a single result was given and no complete algorithm was provided. The second objective of this thesis is to develop a RT-based algorithm for retrieving wave parameters, including wave direction, peak wave period, and mean wave period, directly from radar images, without the derivation of wave spectra or the application of a MTF.

Among ocean wave parameters, significant wave height (H_S) is an important one since it provides an indication of the severity of the sea state. Because the wave spectra are estimated from grey-level values of sea clutter signals rather than from sea surface elevations, directly estimating calibrated wave height values remains challenging. A widely accepted method for H_S estimation is based on a theory developed for SAR applications [46], in which the H_S is assumed to be linearly proportional to the square root of the signal-to-noise ratio (SNR) derived from the radar image sequence [24]. Application of this method has yielded satisfactory results from stationary radar systems. However, the SNR-based method does not always produce robust results for radars operated on a moving platform since the determination of the SNR is very sensitive to the local environment [49, 50]. Also, the SNR-based method requires calibration by an external reference sensor, such as a wave buoy. Therefore, it is necessary to develop techniques independent of the movement of the platform for H_S estimation, and a method independent of external sensors is also needed. These initiatives constitute the third objective of this thesis.

1.3 Scope of the Thesis

In this thesis, novel algorithms are developed for ocean wind and wave parameter extraction from ship-borne X-band marine radar data. The thesis is outlined as follows:

In Chapter 2, a literature review of the research on ocean wind and wave parameter extraction from X-band marine radar data is presented. For wind direction and speed extraction, several techniques are described, and corresponding pros and cons are summarized. For wave parameters determination, existing algorithms for wave spectra and related parameters are first reviewed. Then, a variety of methods for SWH estimation are specifically discussed.

In Chapter 3, two ensemble empirical mode decomposition (EEMD)-based methods for retrieving wind direction from rain-contaminated X-band marine radar images are presented. Each radar image is first decomposed into disparate intrinsic mode function (IMF) components using one-dimensional EEMD (1D-EEMD) or two-dimensional EEMD (2D-EEMD). Then, the standard deviation of one IMF component, or the combination of several IMF components, as a function of azimuth is least-squares fitted to a harmonic function to determine the wind direction.

In Chapter 4, an algorithm to retrieve wind direction and speed from both rain-free and rain-contaminated X-band marine radar images is developed. A data control strategy is proposed for distinguishing rain-free and rain-contaminated radar data. The radar data is decomposed by the EEMD into several IMFs and a residual. A normalization scheme is applied to the first IMF to obtain the amplitude modulation (AM) component. Based on curve-fitting a harmonic function, wind direction is determined from the residual for the rain-free and high-wind-speed rain-contaminated data, and from the AM portion of the first IMF for the low-wind-speed rain-contaminated data. Using a logarithmic relationship, wind speed is determined from a combination of the residual and the AM part of the first IMF for both rain-free and rain-contaminated data.

In Chapter 5, two methods are presented for H_S estimation from X-band marine radar data. One is an EEMD-based method, in which the data sequence in each radial direction of a radar sub-image is decomposed by the EEMD into several IMFs. The normalization scheme is then applied to the IMFs to obtain their AM components. By adopting a linear model, the H_S is estimated from the sum of the amplitudes of the second to the

fifth modes. The other is a modified shadowing-based method, in which modifications, including selecting a subarea along the upwind direction and smoothing the edge pixel intensity histogram, are made to the original shadowing-based algorithm to achieve more accurate wave height measurements. Both methods are applicable to ship-borne radar data, but the modified shadowing-based method does not require external reference sensors.

In Chapter 6, an algorithm based on the Radon transform (RT) is proposed for estimating wave parameters from X-band marine radar images. First, an initial guess of wave direction is determined from the first image of an image sequence. Then, sub-images located in the initial guess wave direction from an image sequence are used to determine wave parameters, including wave direction, peak wave period, and mean wave period.

In Chapter 7, conclusions for this research are summarized, and suggestions for future work are provided.

The achievements of this research have been published in the following journal papers:

1. W. Huang, X. Liu, and E. W. Gill, “Ocean wind and wave measurements using X-band marine radar: A comprehensive review," *Remote Sens.*, vol. 9, no. 12, pp. 1261, Dec. 2017.

   This paper provides a comprehensive review of the state of the art algorithms for ocean wind and wave information extraction from X-band marine radar data (Chapter 2).

2. X. Liu, W. Huang, and E. W. Gill, “Wind direction estimation from rain-contaminated marine radar data using the ensemble empirical mode decomposition method," *IEEE Trans. Geosci. Remote Sens.*, vol. 55, no. 3, pp. 1833-1841, Mar. 2017.

   This paper presents the 1D- and 2D-EEMD-based methods for wind direction extraction from rain-contaminated X-band marine radar data (Chapter 3).

3. W. Huang, X. Liu, and E. W. Gill, “An empirical mode decomposition method for sea surface wind measurements from X-band nautical radar data," *IEEE Trans. Geosci. Remote Sens.*, vol. 55, no. 11, pp. 6218-6227, Nov. 2017.

   This paper presents the EEMD-based method for wind direction and speed extraction from both rain-free and rain-contaminated X-band marine radar data (Chapter 4).

4. X. Liu, W. Huang, and E. W. Gill, “Wave height estimation from ship-borne X-band nautical radar images," *J. Sensors*, vol. 2016, Article ID 1078053, 7 pages, 2016. doi:10.1155/2016/1078053.

   This paper introduces modifications to the shadowing-based algorithm for more robust H_S estimation (Chapter 5).

5. X. Liu, W. Huang, and E. W. Gill, “Comparison of wave height measurement algorithms for ship-borne X-band nautical radar," *Can. J. Remote Sens.*, vol. 42, no. 4, pp. 343-353, Apr. 2016.

   This paper provides the comparison of H_S estimation between the SNR- and modified shadowing-based algorithms (Chapter 5).

6. X. Liu, W. Huang, and E. W. Gill, “Estimation of significant wave height from X-band marine radar images based on ensemble empirical mode decomposition," *IEEE Geosci. Remote Sens. Lett.*, vol. 14, no. 10, pp. 1740-1744, Oct. 2017.

   This paper presents the EEMD-based method for H_S extraction from X-band marine radar data (Chapter 5).

Chapter 2

Literature Review

This chapter contains a review of previous work related to sea surface wind and wave parameter measurements using X-band marine radar. The purpose of the review is to comprehensively summarize the techniques developed for such measurements and to explore remaining challenges. The chapter is divided into two sections: (1) wind measurements and (2) wave measurements.

2.1 Wind Measurements

Wind is a natural movement of air due to differences in the atmospheric pressure. Wind information can be extracted from X-band radar images since the radar backscatter is caused by sea surface roughness which is mainly induced by local winds. Due to the dependence of the radar cross section (RCS) on wind speed [12] and the angle between the radar look direction and the wind direction [13], X-band marine radar has been exploited to retrieve wind parameters [51]. Wind direction has generally been determined based on the fact that the backscatter of an HH-polarized X-band radar operating at grazing incidence presents only one peak in the upwind direction [52]. Wind speed has generally been determined by establishing a model relating wind speed to other parameters derived

from radar images. The wind estimation methods can be classified as wind-streaks-based, image-intensity-variation-over-azimuth-based, and spectral-analysis-based.

2.1.1 Wind-Streaks Based Techniques

Wind streaks are linear features first observed in synthetic aperture radar (SAR) images for ocean surface wind direction estimation [53]. They are mainly caused by local turbulence, foam, and surfactants on the ocean surface. Such wind streaks are also visible in the temporally-integrated X-band marine radar images and aligned with the mean wind direction. Thus, they can also be used for wind measurements using X-band marine radar.

2.1.1.1 Local Gradients Method and Neural Network

The local gradients method (LGM) was originally proposed for extracting wind-induced streaks from SAR images [54]. Dankert *et al.* [14, 55, 56] used LGM to determine wind direction as the orientation of wind-induced streaks from X-band marine radar images. Wind speed was estimated using a neural network (NN) that used the mean normalized RCS (NRCS), radar-derived wind direction, and radar look direction as the input parameters, and wind speed as the output.

For wind direction estimation, the first step is to integrate a radar image sequence over time. Ocean surface wave signatures that show high variability in the time domain can then be removed. As a result, only static and quasi-static signatures of low frequencies, such as wind-induced streaks, remain visible in the integrated image. In the next step, the integrated image is subjected to repeated smoothing and sub-sampling, in which the image resolution is thrice decreased by a factor of 2, resulting in a so-called Gaussian image pyramid. Subsequently, local gradients are obtained from all the sub-sampled images with three different resolutions using optimized Sobel operators [54], and the orientations of local wind streaks are determined to be those that are orthogonal to

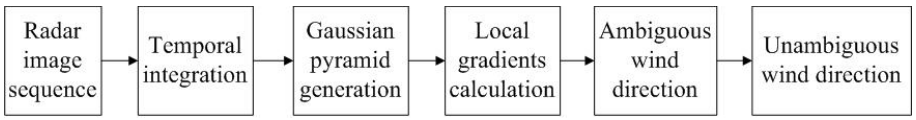

Fig. 2.1 LGM scheme for wind direction estimation.

the local gradients. Then, wind direction is derived as the mean or the mode of all the determined local wind streak orientations. While a 180° ambiguity exists in the derived wind direction, it can be removed using the following techniques. The first technique is based on the cross-correlation function (CCF) of two temporally-integrated radar image sub-sequences. The moving distance and direction of image patterns can be indicated by the location of the CCF peak, thus removing the 180° ambiguity. The second technique is based on the cross-spectrum (CS) of the CCF. The movements of image harmonic features can be derived from the phases of the CS values for the corresponding wavenumbers of the harmonic components. Since the resulting motion directions of the image harmonic features are always within ±90° of the downwind direction, the 180° ambiguity can be removed. Another technique, based on the extraction of wind gusts visible in the image sequence [57], is discussed in Section 2.1.1.2. The LGM scheme for wind direction estimation is shown in Fig.2.1.

For wind speed determination, each temporally-integrated radar image over the range of 600 m or 900 m to 2100 m is divided into range-azimuth bins of 300 m in range and 5° in azimuth. The least inputs required for the NN involve the mean NRCS of the bins within ±15° in both cross-wind directions, the radar-retrieved wind direction and the radar look direction. The mean NRCS in the cross-wind directions is used for two reasons. Firstly, the NRCS is more sensitive to wind speeds in the cross-wind directions. Secondly, the NRCS in the upwind and downwind directions may be affected by blockage and wind shadowing due to neighbouring platforms, respectively. Improvements can be achieved if other parameters related to the sea state and atmospheric conditions are also included as the inputs of the NN. The sea state parameters include the signal-to-noise ratio (SNR), which is proportional to the square of the significant wave height, and

the peak wave phase speed, which can be calculated from peak wave frequency. The atmospheric conditions measured by external sensors include the air-sea temperature difference and the relative humidity.

In [14, 55, 56], two sets of data were used to test the techniques. The first dataset with 3271 data samples was collected from February to June 2001 on the platform Ekofisk 2/4k located in the North Sea around 200 km off the west coast of Norway with wind speed up to 18 m/s. The comparison between *in-situ* and radar-derived wind directions showed a correlation coefficient of 0.99 and a standard deviation of 14.2°. For wind speed retrieval, input parameters involving only the mean NRCS, wind direction, and radar look direction resulted in a correlation coefficient of 0.96 and a standard deviation of 0.97 m/s. Including the air-sea temperature difference as an additional input improved the result, giving a correlation coefficient of 0.97 and a standard deviation of 0.85 m/s. The second dataset of 4786 data samples was collected from August 2003 to November 2004, on the research platform FINO-I in the German Bight of the southern North Sea with wind speed up to 16 m/s. The correlation coefficient and standard deviation are 0.99 and 12.8°, respectively. For wind speed estimation, if only the parameters derived from radar data (mean NRCS, wind direction, radar look direction, SNR, and peak wave phase speed) were used as the inputs for the NN, a result with a correlation coefficient of 0.97 and a standard deviation of 0.66 m/s was obtained. By including the atmospheric conditions (air-sea temperature difference and relative air humidity) as additional inputs, the correlation coefficient improved to 0.99 and the standard deviation became 0.42 m/s. Good results for wind measurements have been obtained using this method. However, it may be difficult to apply the LGM to ship-borne radar data because ship motion may lead to less reliable estimation of the streak orientations from the temporally-integrated radar images. A preprocessing technique, such as georeferencing, may be required for its application to ship-borne radar data. For the NN technique, various input parameters are needed and a training process must be conducted.

2.1.1.2 Optical Flow Motion Estimation

Dankert *et al.* [57] proposed an optical flow motion estimation-based technique (OFM) for retrieving wind fields from X-band marine radar images. This technique is based on the extraction of the movement of wind gusts that are visible in filtered and integrated images. Wind speed can be directly derived from the wind gusts without calibration.

Firstly, to filter out the ocean surface wave signatures, the linear dispersion relationship for surface gravity waves is applied to the 3D wavenumber-frequency spectrum of an image sequence. Next, a temporal moving average over 27 images is applied to a sequence of 32 images to remove high variability in the time domain, resulting in 5 averaged images $G(\vec{\gamma},t)$, with $\vec{\gamma} = (x,y)$ and t being space and time coordinates, respectively. For each averaged image, the same smoothing and sub-sampling process as described in Section 2.1.1.1 is implemented to obtained the so-called Gaussian image pyramid. Then, wind gusts become visible in the resulting images. Based on a common assumption on optical flow, the intensity change in the averaged image is caused only by the motion of wind patterns. Thus, the total time derivative associated with $G(\vec{\gamma},t)$ equals zero, and this results in [58]

$$(\nabla G)^T f_o + G_t = 0, \tag{2.1}$$

where ∇G and G_t are the spatial gradient and partial time derivative of the image intensity, respectively, T denotes the transpose of a matrix, and $f_o = [f_x, f_y]^T$ is the optical flow, with f_x and f_y being the components in the x and y directions, respectively. f_o denotes the local wind velocity vector in this case. Under the assumption that the optical flow is constant within a local area and by using a local weighted least-squares technique, (2.1)

can be solved as [58]

$$\underbrace{\begin{bmatrix} \langle G_x G_x \rangle & \langle G_x G_y \rangle \\ \langle G_y G_x \rangle & \langle G_y G_y \rangle \end{bmatrix}}_{A_G} \underbrace{\begin{bmatrix} f_x \\ f_y \end{bmatrix}}_{f_o} = - \underbrace{\begin{bmatrix} \langle G_x G_t \rangle \\ \langle G_y G_t \rangle \end{bmatrix}}_{b_G}, \tag{2.2}$$

where G_x and G_y are the first-order derivative of the image intensity in the x and y directions, respectively. Here, G_x, G_y, and G_t are calculated using optimized 3D Sobel operators [58]. In (2.2), $\langle a_w \rangle$ stands for a smoothing operation of an arbitrary image a_w, and is expressed as

$$\langle a_w \rangle = \int_{-\infty}^{\infty} w_e(\vec{\gamma} - \vec{\gamma}') a_w d\vec{\gamma}', \tag{2.3}$$

where $\vec{\gamma}' = (x', y')$ is the space vector used in the integral, and w_e is the weighting function for the local weighted least-squares technique, which determines the size of the local area and is generally realized by a Gaussian smoothing kernel. Then, the optical flow, i.e., the local wind velocity vector, may be determined as [58]

$$f_o = A_G^{-1} b_G. \tag{2.4}$$

Note that the local wind velocity vector cannot be determined if A_G is not invertible. Moreover, due to the application of 3D convolution (optimized 3D Sobel operators), the local wind velocity vector cannot be determined from the first and last images of the image sequence and the borders of images. Finally, all available estimated local wind velocity vectors are smoothed, and the mean wind velocity vector is determined as the mode of the smoothed local wind velocity vectors.

To test the technique, only 1332 data samples from the same dataset collected on the platform Ekofisk 2/4 k in the North Sea were used [57]. The correlation coefficient and standard deviation for wind direction measurements were 0.96 and 32.1°, respectively, as compared to reference data from *in-situ* sensors. For wind speed measurements, the

correlation coefficient and standard deviation were 0.64 and 2.68 m/s, respectively. It was observed that increasing the number of images involved in the moving average may improve the results. Although the technique does not require a calibration process, the accuracy of the results is relatively low compared to other methods. Also, as for the LGM, a preprocessing step, such as georeferencing, is required for ship-borne radar applications.

2.1.2 Intensity-Variation-Over-Azimuth Based Techniques

As mentioned earlier, the variation of radar backscatter intensity over azimuth can also be exploited to retrieve wind direction. Other than the NN, wind speed can also be retrieved using an explicit model.

2.1.2.1 Curve Fitting (CF)-Based Methods

A. Single-CF

In [15], Lund *et al.* proposed a single-CF-based method for retrieving both wind direction and speed. Wind directions are extracted using a harmonic function that is least-squares fitted to the radar backscatter intensity as a function of azimuth. Wind speeds are determined from the average radar backscatter intensity using an empirical third-order polynomial obtained through training.

For HH-polarized X-band radar images collected at grazing incidence, only one backscatter intensity peak exists in the upwind direction [52]. This is the key for wind direction estimation. First, radar backscatter intensities are averaged along each unobstructed azimuthal direction. Then, the average radar backscatter intensity σ_{wDir_θ} as a function of the azimuthal direction θ is least-squares fitted by a cosine square function

$$\sigma_{wDir_\theta} = p_0 + p_1 \cdot \cos^2(0.5(\theta - p_2)), \tag{2.5}$$

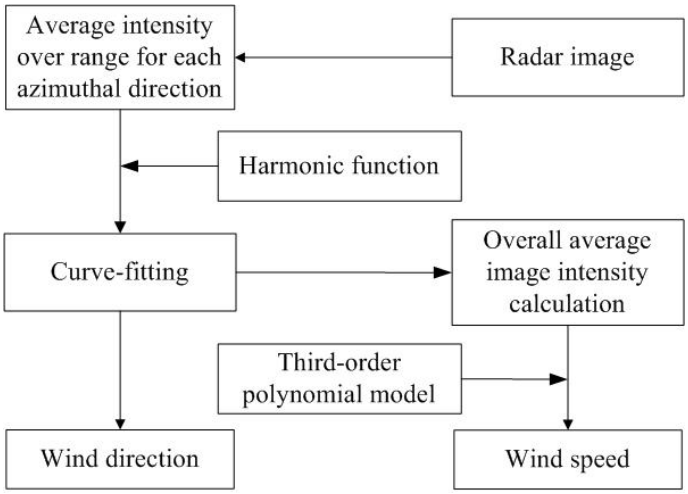

Fig. 2.2 Basic steps of the single-CF method for wind direction and speed retrieval.

where p_0, p_1, and p_2 are parameters determined through least-squares fitting. Wind direction is determined as the azimuthal direction corresponding to the peak of the fitted function. With least-squares fitting, wind directions can be retrieved even if the upwind direction appears in the obstructed portions of the image.

Wind speeds are retrieved by exploiting the dependence of radar backscatter intensity on wind speed. The overall average radar backscatter intensity σ_{wSpd} of one radar image is calculated as the integration of the fitted function in (2.5) over the full azimuth. This is expressed as

$$\sigma_{wSpd} = \frac{1}{2\pi}\int_0^{2\pi}(p_0 + p_1\cos^2(0.5(\theta - p_2)))d\theta. \tag{2.6}$$

The fitted function in (2.5) is used for calculating σ_{wSpd} because it automatically fills the gaps in obstructed image portions. Then, a third-order polynomial relationship between σ_{wSpd} and wind speed is assumed and trained using the wind speed data that are collected by external sensors such as anemometers. Based on the obtained third order polynomial, wind speed can be retrieved from σ_{wSpd} for each individual radar image. The basic steps of the single-CF method for wind direction and speed retrieval are illustrated in Fig.2.2.

The datasets used to test the method were collected from the R/V Roger Revelle travelling in the Philippine Sea near Taiwan island during two storms from August 6

to August 9 and from September 12 to September 17, 2010, respectively [15]. For wind speed retrieval, the empirical model function was trained using the data associated with the first storm and validated with those collected during the second storm. For the 6282 measurements obtained from the first storm with the reference wind speed varying from 2 to 17 m/s, the correlation coefficients and root-mean-square (RMS) differences between the anemometer-measured and radar-derived wind direction were 0.97 and 14.2°, respectively, and 0.90 and 0.88 m/s, respectively, for wind speed. For the 11321 measurements from the second storm with the reference wind speed up to 15 m/s, a correlation coefficient of 0.95 and a RMS difference of 17.4° for wind direction were obtained, and those for wind speed retrieval were 0.91 and 0.79 m/s, respectively. The results show that the CF-based method works well for ship-borne X-band marine radar data, even if some portions of the radar image are obstructed by ship structures. Furthermore, only one parameter derived from the radar data is needed to train the model function, significantly simplifying the wind speed estimation compared to the NN-based technique.

B. Dual-CF

Under low sea states, the overall image intensities are low, and this may lead to inaccurate wind estimation when using the CF-based method. Therefore, Liu *et al.* [17] modified the original CF-based method [15] with a dual-CF technique to improve wind direction and speed results under low sea state conditions.

In the dual-CF technique, an initial estimation of wind direction is first obtained by using the single-CF method. Then, to update the wind direction value, the radar data within $\pm 60^\circ$ of this estimated wind direction are employed for a second CF process. The range of $\pm 60^\circ$ is used because it is wide enough to include the actual wind direction and it is narrow enough to exclude low image intensities due to low sea states. For wind speed retrieval, negative values of the fitted function derived from the dual-CF technique are

discarded from the integration in (2.6) for the calculation of the average radar backscatter intensity σ_{wSpd}.

To test the technique, two sets of data [17] were collected by the Canadian Navy research ship CFAV Quest during a sea trial in the North Atlantic Ocean off the east coast of Canada while wind speed varied from 2 m/s to 16 m/s. Both the original CF-based method and the dual CF technique were applied to the two datasets. The first dataset of 49182 radar images was collected from a Decca radar from November 26 to November 29, 2008. After excluding 9924 rain-contaminated images and 1832 low-backscatter images from the dataset, the standard deviation of wind direction results derived by applying the dual-CF technique was 14.9°, which was 0.4° less than that of the single-CF method. The standard deviation of wind speed results derived from the dual-CF technique was 1.4 m/s, which was the same as the single-CF method. The second dataset containing 69088 radar images was collected from a Furuno radar from December 1 to December 4, 2008. 992 rain-contaminated images and 8337 low-backscatter images were excluded from this dataset. The standard deviations of the wind direction and speed results derived by the dual-CF technique were 16.6° and 1.9 m/s, respectively, with respect to the anemometer reference, showing an improvement of 0.4° and 0.1 m/s, respectively, compared to the single-CF method.

C. Two-model-CF

In both the single-CF method and dual-CF technique, radar data collected in the presence of rain were excluded from wind estimation. This is because rain affects the radar backscatter and leads to less reliable wind estimation. Huang and Gill [59] proposed an algorithm to improve wind speed extraction from rain-contaminated radar images. Radar data contaminated by rain are first identified and extracted based on a parameter called zero-pixel percentage (ZPP). Then, the same third-order polynomial used for rain-free data in [15] are trained separately for the rain-contaminated data.

The algorithm was tested using the Decca radar data as described in Section 2.1.2.1-B [59]. The comparison between *in-situ* and radar-derived wind speeds using the two-model algorithm showed a standard deviation of 1.7 m/s, which represents an improvement of 1.2 m/s compared to the results derived by using only one model for both rain-free and rain-contaminated radar data. However, in spite of the improvement of the wind speed estimation accuracy under rain conditions, the implementation cost of the algorithm is compromised by an additional procedure for distinguishing rain-free and rain-contaminated data and an extra training model.

2.1.2.2 Intensity Level Selection (ILS)-Based Methods

A. Original ILS

Vicen-Bueno *et al.* [16] proposed an ILS-based method for retrieving wind parameters from temporally-integrated and spatially-smoothed radar images. Wind direction is determined by searching for the maximum range for a selected intensity level along the azimuth, while wind speed is derived from the selected intensity level and its corresponding maximum range by training an empirical third-order polynomial geophysical model function.

In the first step, radar images are temporally integrated and spatially smoothed to remove high variabilities in the time and space domains, respectively. Then, a sequence of intensity levels is defined based on the image intensity range. For every azimuthal direction of each integrated and smoothed image, the maximum range with an intensity level equal to or greater than each defined intensity level is identified. Next, for each defined intensity level, the identified maximum ranges from all azimuthal directions are smoothed by a moving average over 5°, and the lowest defined intensity level with all its associated smoothed maximum ranges being greater than an inner distance boundary is designated as the selected intensity level. Finally, the wind direction is determined as the azimuthal direction corresponding to the peak of the smoothed maximum ranges

associated with the selected intensity level. After applying the above procedures to the first several integrated and smoothed images, rather than all the defined intensity levels, only the selected intensity level from the previous image and its upper and lower defined intensity levels are used for wind retrieval. This makes the algorithm more efficient.

Wind speed w_{Spd}, which is estimated from the selected intensity level and the peak of smoothed maximum ranges associated with the selected intensity level, can be expressed as [16]

$$w_{Spd} = \alpha_r \times r_{p_{\max}}, \tag{2.7}$$

with

$$\alpha_r = p_3 {L_S}^3 + p_2 {L_S}^2 + p_1 L_S + p_0, \tag{2.8}$$

where $r_{p_{\max}}$ is the peak of smoothed maximum ranges associated with the selected intensity level L_S, α_r is the conversion rate between $r_{p_{\max}}$ and w_{Spd}, and p_0, p_1, p_2, and p_3 are the parameters determined by least-squares fitting. For the training process, wind speed is measured by external sensors such as anemometers. After the training is completed, wind speed can be estimated from L_S and $r_{p_{\max}}$ for each individual integrated and smoothed radar image.

Datasets used to test this method were collected from the research platform FLIP at approximately 30 km northwest of Bodega Bay, California, USA, during four periods in June June 2010 while wind speed varied from 4 m/s to 22 m/s [16]. Data collected in the first period were used for training and those collected in the other three periods were used for testing. As compared to reference values from anemometer data, the standard deviations of wind direction and speed results were 11° and 0.6 m/s, respectively, for the training data, and 14.3° and 0.8 m/s, respectively, for the test data.

B. Modified ILS

In the original ILS method, the obstruction of the radar field of view (FOV) and the appearance of islands may lead to less accurate results. Thus, Liu *et al.* [17] modified the

original ILS method in [16] with blockage and island recognitions and an additional CF process, resulting in more robust wind direction and speed results when blockages or islands exist in the radar field of view.

First of all, blockages in the radar FOV due to obstruction by ship structures or other unknown factors are recognized. Blocked azimuthal directions are identified as those with ZPPs greater than 20%, and data in those directions are excluded from the ILS. Then, islands in the radar FOV are recognized as intensity bumps in the radar images. The intensity bump in each azimuthal direction is identified by applying the MATLAB built-in function, findpeaks. Data in the azimuthal directions in which islands are identified are also excluded from the ILS. Furthermore, an outer distance boundary is set for the ILS due to possible noise in the very far range. All smoothed maximum ranges associated with the selected intensity level should be smaller than the outer distance boundary. Finally, the harmonic function (2.5) is used to least-squares fit the smoothed maximum ranges to fill the gaps due to the exclusion of data. The azimuthal direction corresponding to the peak of the fitted function is determined as the wind direction and is further utilized for the wind speed determination which follows the original ILS procedure.

The same datasets as described in Section 2.1.2.1-B were used to test the method [17]. Both the original and modified ILS methods were applied. For the Decca radar data, the modified ILS method produced wind direction and speed measurements with standard deviations of 15.9° and 1.4 m/s, respectively, which were reduced by 4.9° and 0.1 m/s, respectively, compared to the original ILS method. The standard deviations of wind direction and speed results derived from the Furuno radar data by the modified ILS method were 16.3° and 1.3 m/s, respectively, with improvements of 4.9° and 0.2 m/s, respectively, over the original ILS method. Moreover, another dataset of 992 radar images, containing island interference, collected by the Furuno radar on October 29, 2008 were used. No rain-contaminated or low-backscatter images were found in this dataset. It was observed that the modified ILS method, producing standard deviations of

11.8° and 1.0 m/s for wind direction and speed estimation, respectively, outperformed the original ILS method by 7° and 0.3 m/s, respectively.

C. Texture-analysis

Huang *et al.* [60] proposed a texture-analysis incorporated (TAI) algorithm for extracting wind parameters from rain-contaminated radar images. The TAI method first requires the identification of the rain-contaminated pixels in each azimuthal direction of radar images based on texture analysis. Then, only the data from the azimuthal directions in which the rain contamination is negligible are used to extract wind parameters by applying the modified ILS method.

The texture of a radar image, $T_{m,n}$, is generated based on the calculation of intensity RMS difference as

$$T_{m,n} = \sqrt{\frac{1}{9}\sum_{i=-1}^{i=1}\sum_{j=-1}^{j=1}(I_{m,n} - I_{m+i,n+j})^2}, \tag{2.9}$$

where $I_{m,n}$ is the image intensity at range index m and azimuth index n. With the obtained $T_{m,n}$, n_θ is defined as the number of pixels with intensities larger than 40 in each azimuthal direction, which is then moving averaged over 32 points along the azimuthal direction. After that, a parameter I_{Tex} can be determined as

$$I_{Tex} = \begin{cases} n_{\theta\min} + 5, n_{\theta\max} - n_{\theta\min} \leq 35 \\ n_{\theta\min} + 0.25(n_{\theta\max} - n_{\theta\min}), else \end{cases}, \tag{2.10}$$

where $n_{\theta\min}$ and $n_{\theta\max}$ are the minimum and maximum of the averaged n_θ, respectively. Then, if the number of pixels with intensities larger than I_{Tex} is higher than or equal to 20 in one azimuthal direction in the image texture $T_{m,n}$, that direction is considered as the one with negligible rain contamination and is retained. By this means, wave signatures can be retained in the image texture while rain clutter can be removed.

The Decca radar data as described in Section 2.1.2.1-B were used for the validation of this method [60]. For rain-contaminated data, the standard deviations of wind direction

and speed results are 19.9° and 2.0 m/s, respectively, by using the TAI method, and 34.4° and 3.3 m/s, respectively, without incorporating TAI. For all data, the standard deviations for wind direction extraction with and without TAI are 16.8° and 21.2°, respectively, and for wind speed are 1.5 m/s and 1.9 m/s, respectively.

2.1.2.3 Probability Distribution Function

Chen *et al.* [61] proposed a probability distribution function (PDF)-based method to retrieve nearshore sea surface wind vectors. With an adjustment for the influence of land, wind direction is also retrieved based on the azimuthal dependence of radar image intensity levels. Wind speed is determined from a model based on the PDF of image intensity levels and significant wave height, H_S.

For wind direction retrieval, the average image intensity level σ_{wDir_θ} for each azimuthal direction θ is first calculated. Then, a sine function is used to least-squares fit the average image intensity level as a function of azimuthal direction. The result is expressed as

$$\sigma_{wDir_\theta} = p_0 + p_1 \cdot \sin(\theta + p_2), \tag{2.11}$$

where p_0, p_1, and p_2 are parameters determined by the least-squares fitting process. Then, the azimuthal direction corresponding to the peak of the fitted function, θ_{peak}, is obtained. However, since the wind direction was affected by two hills in the vicinity of the experimental site [61], θ_{peak} may not be the wind direction. Thus, an adjustment, $\Delta\theta$, obtained using the anemometer reference, to determine the wind direction w_{Dir}, as given by

$$w_{Dir} = \theta_{peak} + \Delta\theta, \tag{2.12}$$

is required.

For wind speed retrieval, the expectation $\sigma_{\exp}$ of the radar image intensity levels is calculated from the PDF of those levels. Then, a relationship between wind speed w_{Spd}

and σ_{exp} as well as H_S is sought through fitting

$$w_{Spd} = (p_2\sigma_{\text{exp}} + p_1)[1 + e^{(-\frac{p_0}{H_S})}], (p_0 > 0), \tag{2.13}$$

where p_0, p_1, and p_2 are parameters determined by the least-squares fitting process. In this model, the wind speed changes approximately linearly with σ_{exp} under low sea state conditions, while H_S mainly takes into account swell effects under high sea states. After the model is obtained, wind speed can be retrieved from σ_{exp} and H_S.

Datasets used to test the method were collected on Haitan Island, China, from October to December 2010 [61]. The data consisted of 535 radar image sequences and simultaneous anemometer and buoy measurements, and were divided into 10 groups based on corresponding wind speed values which ranged from 0 m/s to 20 m/s in increments of 2 m/s. One third of the data randomly selected from each interval were used for training the wind speed model, and the remainder were used for validating the model. An acceptable RMS difference of 26.2° for wind direction estimation was obtained while wind speeds ranged from 5 m/s to 20 m/s. For the data with wind speed varying from 0 m/s to 20 m/s, the RMS difference of wind speed retrieval results was 1.37 m/s. It was also found from the result that H_S should be included in (2.13) under moderate to high wind conditions.

2.1.3 Spectral-Analysis Based Techniques

2.1.3.1 Background Noise

Izquierdo and Soares [62] presented a method for retrieving wind speed from the background noise (BGN) of radar image sequences.

An image frequency-wavenumber spectrum is first obtained by applying the 3D discrete Fourier transform (DFT) to the radar image sequence. Then, spectral components corresponding to ocean waves and BGN are separated using the linear dispersion

relationship for gravity waves. The total spectral energy, F_{BGN_T}, of the BGN is used to estimate wind speed based on the trained linear model

$$F_{BGN_T} = p_0 + p_1 w_{Spd}, \tag{2.14}$$

where p_0 and p_1 are parameters determined by a regression fitting.

Datasets used to test the method were collected close to the Port of Sines in Portugal, from September 2000 to December 2001 with 925 simultaneous records of radar image sequences and wind speed and direction from the meteorological station [62]. A radar image was divided into 36 equiangular directional sectors, covering 360°. The calibration was implemented for each directional sector. The results showed that wind speeds derived from the sector along the upwind direction agreed best with the wind speed references, resulting in a correlation coefficient of 0.89 and a RMS difference of 2.86 m/s with the reference wind speed ranging from 1 to 10 m/s.

2.1.3.2 1D Spectral Analysis

Most of the aforementioned methods can provide reliable wind measurements only in the absence of rain. Recently, Wang and Huang [18] found that when the wind speed is high (over about 8 m/s), obtaining wind direction using the CF-based method in [15] is not significantly affected by rain. However, the accuracy may substantially decrease if the radar images are acquired during rain events under low wind speed. Thus, a method to estimate wind direction based on the 1D spectral analysis (SA) of radar backscatter in the wavenumber domain is proposed in [18]. Later, Huang and Wang [19] extended the 1D SA-based method for wind speed estimation from both rain-free and rain-contaminated radar data.

In the 1D SA algorithm, a DFT is first applied to the backscatter intensity sequence in each column of the polar radar image to obtain its wavenumber spectrum as

$$E_n(k) = E_n(\frac{2\pi k'}{M\Delta r}) = \sum_{m=1}^{M} I_n(m) e^{-j\frac{2\pi}{M}k'm}, \tag{2.15}$$

where M is the number of image pixels in each column, $I_n(m)$ is the mth pixel intensity in the nth column (azimuthal direction of $\frac{2\pi(n-1)}{N}$, N being the number of columns in a polar radar image), $|E_n(k)|$ is the spectral value of wavenumber k in the nth column, k' is the wavenumber bin and ranges from 0 to $M/2$, and Δr is the image range resolution.

For rain-free and high-wind-speed rain-contaminated cases, the spectral value at zero wavenumber as a function of column n, $|E_n(0)|$, is least-squares fitted to a harmonic function as

$$|E_n(0)| = p_0 + p_1 \cos^2(0.5(\frac{2\pi(n-1)}{N} - p_2)). \tag{2.16}$$

Here, p_0, p_1, and p_2 are parameters determined by the least-squares fitting. Wind direction is determined as the azimuth corresponding to the peak of the fitted function. In low-wind-speed, rain-contaminated cases, an integral of spectral values over the wavenumber range [0.01, 0.2] is calculated for each column as

$$S_n = \int_{0.01}^{0.2} |E_n(k)|\, dk. \tag{2.17}$$

Then, S_n is least-squares fitted to the harmonic function in (2.16) as

$$S_n = p_0 + p_1 \cos^2(0.5(\frac{2\pi(n-1)}{N} - p_2)). \tag{2.18}$$

Wind direction is determined as the azimuth corresponding to the peak of the fitted function.

In wind speed retrieval, for both rain-free and rain-contaminated radar images, the spectral integration is calculated for each image as

$$S_T = \frac{1}{MN} \sum_{n=1}^{N} \sum_{k'=0}^{M/2} |E_n(\frac{2\pi k'}{M\Delta r})|. \tag{2.19}$$

Then, a logarithmic relationship between S_T and wind speed w_{Spd} is sought through curve-fitting

$$S_T = p_0 + p_1 \cdot \ln(w_{Spd} + p_2), \tag{2.20}$$

where p_0, p_1 and p_2 are parameters determined from the curve-fitting process. After the parameters are determined based on (2.20), wind speed can be estimated from S_T for any radar data.

The Decca radar data as described in Section 2.1.2.1-B were used to test the method [18, 19]. Both the original CF and 1D SA methods were applied. The low-backscatter images were excluded for the wind direction retrieval but retained for the wind speed retrieval. For wind direction estimation, the standard deviations between radar and anemometer measurements for the original CF and 1D SA methods are 46.7° and 21.6°, respectively, under rain conditions, and 20.3° and 15.8°, respectively, for all data. For wind speed estimation, the RMS differences for the original CF and 1D SA methods are 7.5 m/s and 1.6 m/s, respectively, for rain cases, and 1.5 m/s and 1.6 m/s, respectively, for rain-free data. For all data, the correlation coefficients are 0.79 and 0.89, respectively, for the original CF and 1D SA methods. The results indicate that the 1D SA wind algorithm is applicable to both rain-free and rain-contaminated radar data. Moreover, the method significantly improves wind measurements under rain conditions. However, the wind direction result may not be accurate if the upwind direction is contaminated by rain, and the wind speed result is not always robust when the wind speed is high.

Table 2.1 Inter-Comparison of the Reviewed Wind Measurement Techniques

Methods	RMS Difference		Applicable Under			Calibration-Free		Images Required
	Wind Direction (°)	Wind Speed (m/s)	Ship Motion	Blockage	Rain	Wind Direction	Wind Speed	
Local Gradients Method & Neural Networks	12.8 - 14.2	0.42 - 0.85	×	√	×	√	×	Multiple
Optical Flow Motion	32.1	2.68	×	√	×	√	√	Multiple
Single Curve Fitting	14.2 - 17.4	0.79 - 0.88	√	√	×	√	×	Single
Dual Curve Fitting	14.9 - 16.6	1.4 - 1.9	√	√	×	√	×	Single
Two-Model Curve Fitting	-	1.7	√	√	√	-	×	Single
Original Intensity Level Selection	11 - 14.3	0.6 - 0.8	√	×	×	√	×	Multiple
Modified Intensity Level Selection	11.8 - 16.3	1 - 1.4	√	√	×	√	×	Multiple
Texture-Analysis	16.8	1.5	√	√	√	√	×	Multiple
Probability Distribution Function-Based	26.2	1.37	√	√	×	×	×	Single
Background Noise-Based	-	2.86	√	×	×	-	×	Multiple
1D Spectral Analysis	15.8	1.6	√	√	√	√	×	Single

2.1.4 Summary

The inter-comparison of the reviewed techniques for wind measurements is listed in Table2.1with the applicability, or otherwise, of a particular method being indicated by $\surd$ or $\times$, respectively. It can be observed from the table that ship motion has a significant effect on the LGM and OFM; the original ILS and BGN methods may not be applicable if portions of the radar images are blocked; the two-model-CF, texture-analysis-incorporated, and 1D spectral analysis algorithms work well under rain effects; and the OFM is calibration-free for wind speed retrieval.

2.2 Wave Measurements

Wave information can be extracted from X-band marine radar sea surface images due to the visibility of ocean waves in the radar images. Algorithms for such wave measurements are usually based on a wavenumber-frequency spectral analysis of the radar image time series using a 3D discrete Fourier transform (DFT) [9]. Recently, a variety of algorithms for wave measurements using X-band marine radar have appeared. These algorithms can be categorized as spectral-analysis-based and texture-analysis-based.

2.2.1 Spectral-Analysis Based Techniques

For wave algorithms based on spectral analysis, wave spectra are first obtained from series of radar images. Then, wave parameters are derived from the obtained wave spectra.

2.2.1.1 3D-DFT-Based Algorithms

A. Traditional algorithm

The traditional 3D-DFT-based algorithm is a relatively mature technique, which has also been implemented in the commercial wave monitoring system WaMoS II [2,39].

In this technique, rectangular sub-image sequences are first extracted from the time series of consecutive radar images. Then, in order to eliminate the static patterns due to the range dependence of the radar backscatter, image normalization is implemented on the sub-image sequence by subtracting the mean intensity of each pixel in the time series from its actual intensity. After that, the so-called image spectrum $F_I^{(3)}(\vec{k},\omega)$, where $\vec{k}$ is the wavenumber vector and ω is the angular frequency, is obtained by applying a 3D DFT to the normalized sub-image time sequence. To remove the non-stationary and non-homogeneous trends in the sub-image time series, the image spectrum is high-pass filtered with an empirical angular frequency threshold of $\omega_{th} = 0.03 \cdot 2\pi$ rad/s. The velocity of encounter current, which is the combined velocity of the ship and surface current, is determined from the high-pass filtered image spectrum using appropriate methods (see, e.g., [20–23]). The wave-related image spectrum $F_F^{(3)}(\vec{k},\omega)$ is separated from noise using a band-pass filter defined by the dispersion relationship, including the current-induced Doppler shift [11]. Due to the non-linearity caused by the radar imaging mechanisms, a further correction for converting the wave-related image spectrum to the actual wave spectrum $F_W^{(3)}(\vec{k},\omega)$ is performed by a modulation transfer function (MTF) $T_M(\vec{k})$ as [10]

$$F_W^{(3)}(\vec{k},\omega) = F_F^{(3)}(\vec{k},\omega) \cdot T_M(\vec{k}). \tag{2.21}$$

With the obtained 3D wave spectrum $F_W^{(3)}(\vec{k},\omega)$, the 2D wavenumber wave spectrum $F_W^{(2)}(\vec{k})$, 2D frequency-directional wave spectrum $E^{(2)}(\omega,\phi)$, and 1D frequency wave spectrum $S(\omega)$ can be derived as [11,39]

$$F_W^{(2)}(\vec{k}) = 2 \int\limits_{\omega>0} F_W^{(3)}(\vec{k},\omega) d\omega, \tag{2.22}$$

$$E^{(2)}(\omega,\phi) = F_W^{(2)}(\vec{k}(\omega,\phi)) \left|\vec{k}\right| \frac{d\left|\vec{k}\right|}{d\omega}, \tag{2.23}$$

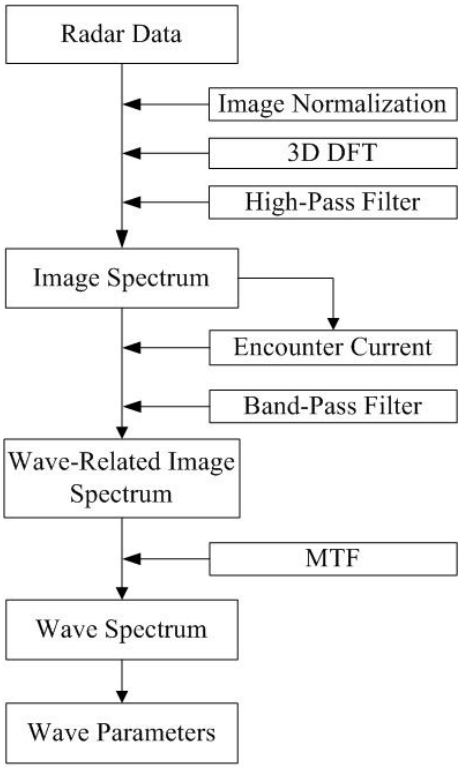

Fig. 2.3 Basic steps of the traditional 3D-DFT based algorithm.

$$S(\omega) = \int_{-\pi}^{\pi} E^{(2)}(\omega, \phi) d\theta. \tag{2.24}$$

Then, wave parameters such as wave direction and periods can be deduced from the wave spectra [37, 38]. The basic steps of the traditional 3D-DFT-based algorithm are shown in Fig.2.3.

However, since the radar image intensities are not related to sea surface elevations, but to the strength of radar backscatter signals, the wave spectra obtained as above represent relative values which are not properly scaled. Therefore, wave height cannot be directly determined from the radar-derived wave spectra. For estimating wave height, a widely accepted approach is based on a technique originally developed for synthetic aperture radars (SAR) applications [46], in which H_S is assumed to be proportional to the square root of the signal-to-noise ratio (SNR) [24]. The signal is assumed as the total energy of the estimated wave spectrum and the noise is computed as the energy due to the speckle caused by the sea surface roughness.

Assuming that the background noise (BGN) is a stochastic process and uncorrelated with wave field components in the image spectrum, the 3D BGN spectrum $F_{BGN}^{(3)}(\vec{k},\omega)$ can be obtained as

$$F_{BGN}^{(3)}(\vec{k},\omega) \simeq F_{I}^{(3)}(\vec{k},\omega) - F_{F}^{(3)}(\vec{k},\omega) - F_{H}^{(3)}(\vec{k},\omega), \tag{2.25}$$

where $F_{H}^{(3)}(\vec{k},\omega)$ is the high harmonic spectrum, which is induced by non-linear radar imaging mechanisms such as shadowing and is extracted in a similar way to the wave-related spectrum but using the high harmonic dispersion relation. Having obtained the wave and BGN spectra, the SNR used in the linear model for the wave height estimation can be calculated as

$$SNR = \frac{\int_{\Omega_{\vec{k}}^{\alpha}} F_{W}^{(2)}(\vec{k}) d^2k}{\int_{\Omega_{BGN}} F_{BGN}^{(3)}(\vec{k},\omega) d^2k d\omega}. \tag{2.26}$$

The integration domains Ω_{BGN} and $\Omega_{\vec{k}}^{\alpha}$ in (2.26) are respectively given by

$$\Omega_{BGN} \equiv [-k_{x_c}, k_{x_c}) \times [-k_{y_c}, k_{y_c}) \times [\omega_{th}, \omega_c) \tag{2.27}$$

$$\Omega_{\vec{k}}^{\alpha} \equiv \{\vec{k} \in \Omega_{\vec{k}} | F_{W}^{(2)}(\vec{k}) \geq \alpha \cdot max[F_{W}^{(2)}(\vec{k})]; 0 \leq \alpha \leq 1\}, \tag{2.28}$$

where k_{x_c}, k_{y_c}, and ω_c are the Nyquist wavenumber and frequency limits, respectively, within which the image spectrum is defined. The threshold α is used to eliminate the BGN contribution within the pass band in the wave component extraction. Finally, H_S can be derived using the linear model,

$$H_S = p_0 + p_1 \sqrt{SNR}, \tag{2.29}$$

where p_0 and p_1 are the calibration parameters which are determined by fitting the square root of the SNR and buoy-measured wave heights. These parameters may differ for

different systems. After the linear model is obtained, H_S can be derived from the SNR for each radar image sequence.

The SNR-based method has been tested with various datasets by many researchers [2, 24, 37–39, 47, 48]. The datasets collected from the Floating Production and Storage Offshore (FPSO) platform, Norne, in the northern North Sea from November 1997 to January 1998 [24, 39, 48] showed that the correlation coefficient between H_S measured by buoy and radar was 0.89, and the root-mean-square (RMS) difference was 0.38 m with the buoy-measured H_S ranging from 0.5 to 5.5 m. The correlation coefficient for the datasets collected from the FPSO Curlew in the central North Sea from May to June 1998 and from the Gulf of Biscay from February to April 1998 were 0.85 and 0.71, respectively [48]. The difference of buoy and radar positions mainly accounted for the low correlation of 0.71 due to a significant change of bathymetry. For the datasets acquired from the northern coast of Spain from 28 February to 23 April 2000 [37], the correlation coefficient between the 312 pairs of the square root of SNR derived from radar images and H_S measured by buoy was 0.83. Another two datasets were used to test the method using HH- and VV-polarized radars in [38]. The first dataset collected from Zhangzi Island, China, from February to April 2009 was used for calibration, and the second dataset used for validation was collected from Zhangzi Island during January, 2009 and from the South China Sea on 26 June 2009. The correlation coefficients for the calibration dataset were 0.74 and 0.86 for the HH- and VV-polarized radars, respectively, and the corresponding values for the validation dataset were 0.71 and 0.85, respectively. This indicated that the VV-polarized radar was more suitable for the H_S estimation. Although this SNR-based method for H_S estimation has been successfully applied to such stationary radar systems, it was found in [49, 50] that it may be challenging to achieve a comprehensive calibration for radar operations on moving vessels on the open sea.

Later, in [63], the dependency of wave parameter retrieval on range and azimuth was analyzed and removed. This enabled robust wave parameter measurements in the

case where the radar field of view (FOV) is partially obstructed. By retrieving the SNR, peak wave period, and peak wave direction from sub-image time series azimuthal-evenly distributed in the radar FOV, it was found that the SNR shows a higher peak in the upwave direction and a lower peak in the downwave direction, and both the peak wave periods and directions derived from different azimuths display a period of 180°. Thus, for the H_S estimation, the SNRs derived from the azimuthal-evenly distributed sub-images in the unobstructed radar FOV are least-squares fitted to a Fourier series. Then, the higher peak (upwave direction) or the lower peak (downwave direction) of the fitted curve is used to estimate H_S. The peak wave period and direction are estimated as the average of those derived from the azimuthal-evenly-distributed sub-images covering 180° in the unobstructed radar FOV.

B. Multilayer perceptrons

A limitation of the standard SNR-based method for H_S estimation is that local wind speed should be higher than a threshold to produce sufficient sea surface roughness and radar backscatter. Under low wind speeds or swell-dominated sea state conditions, the BGN energy may be low, leading to large SNR and, therefore, overestimated H_S. To mitigate this, Vicen-Bueno *et al.* [64] proposed a non-linear model using artificial neural networks (ANN) with multilayer perceptrons (MLP). In addition to the square root of the SNR, peak wavelength and mean wave period are also used as input parameters. One hidden layer with 15 hidden neurons is selected for the MLP.

The technique was tested using two datasets [64]. One dataset with 49096 measurements and manifesting bimodal sea states (wind sea and swell) was collected at Ekofisk in the Norwegian sector of the North Sea from October 2008 to May 2009. Another dataset containing 67684 measurements, with a swell-dominated sea state, was collected at FINO 1 in the German basin of the North Sea from April 2005 to August 2008. Both the standard SNR- and MPL-based methods were applied to the two datasets. For the testing data of 19096 measurements at Ekofisk, as compared to the reference H_S of 0.5

to 8 m measured by buoy, the correlation coefficient and the standard deviation of H_S derived by the MLP-based method were 0.97 and 0.22 m, respectively, which were 0.02 and 0.05 m, respectively, higher than those of the standard SNR-based method. For the testing data involving 20144 measurements at FINO 1 with the buoy-measured H_S up to 10 m, the MLP-based method produced a correlation coefficient of 0.96 and a RMS difference of 0.27 m, with improvements of 0.07 and 0.17 m, respectively, over the MLP-based method. A more significant improvement was observed for the dataset collected at FINO 1 since this location was dominated by swell.

C. Iterative least-squares

Huang *et al.* [65] presented an iterative least-squares (LS)-based method for wave measurements, which is based on the iterative LS methods for ocean surface current determination from X-band marine radar images [20, 66]. This method, which does not require a band-pass filter as in the traditional 3D-DFT-based algorithm, simplifies the wave measurement.

After applying the 3D DFT to the radar image series and high-pass filtering the image spectrum, the ocean surface current has to be determined. An initial guess of the surface current is first derived using a basic LS method as in [9]. Then, a lower threshold than that in [9] is used to obtain spectral points that may correspond to the fundamental and harmonic modes of the linear wave dispersion relationship. The current-induced Doppler-shifted dispersion relationship at the pth harmonic mode is expressed as

$$\omega_p(\vec{k}) = (p+1)\sqrt{\frac{g\left|\vec{k}\right|}{p+1}} + \vec{k}\cdot\vec{U}, \tag{2.30}$$

where g is the acceleration due to gravity, and $\vec{U}$ is the surface current vector. In each iteration, $\omega_p(\vec{k})$ is calculated using the surface current vector derived from the previous iteration or the initial guess. Due to the aliasing effect, $\omega_p(\vec{k})$ located in the qth frequency

interval is folded to $\omega_{p,q}(\vec{k})$ through mapping according to the properties of periodicity and point symmetry about the origin. The obtained spectral points that satisfy

$$\min_{p,q}(\left|\omega_i - \omega_{p,q}(\vec{k})\right|) < \Delta\omega, \tag{2.31}$$

where ω_i is the angular frequency in the ith angular frequency panel of the 3D image spectrum and $\Delta\omega$ is the angular frequency resolution, are used to estimate a new surface current vector by the LS fitting as in [20]. The iteration is repeated until the termination criterion defined in [66] is met. When the final surface current is determined, since the spectral points used in the iterations have been automatically classified as the fundamental and different harmonic modes of the dispersion relationship, the band-pass filter in the traditional 3D-DFT-based algorithm is not required. Here, the spectral points associated with the fundamental mode (p=0) and the first harmonic mode (p=1) are extracted for the wave measurement. Then, after applying an MTF, wave spectra and related wave parameters can be derived.

The iterative LS-based wave measurement method was tested using both vertically- and horizontally-polarized X-band radar data [65]. Both the traditional 3D-DFT-based algorithm and the iterative LS-based method were applied to the data. The vertically-polarized land-based radar data were acquired at Skerries Bight near St. John's Harbour on the east coast of Canada on December 15 and 20, 2010. The results showed that compared to the buoy reference, the RMS differences of the peak wave periods and peak wave directions derived using both techniques were less than 1 s and 10°, respectively. The horizontally-polarized ship-borne radar data were acquired about 220 km Southeast of Halifax from 14:16 on November 28 to 12:06 on November 29, 2008, with peak wave period ranging from 10 s to 12 s and peak wave direction being around 110°. The RMS differences for the peak wave periods derived from the traditional algorithm and the iterative LS-based method were 0.87 s and 0.98 s, respectively. For the peak wave directions, the corresponding values were 6.4° and 7.3°, respectively. The results

derived from the iterative LS-based method were similar to those from the traditional 3D-DFT-based algorithm, again indicating the capability of the method.

D. New MTFs

In the traditional 3D-DFT-based algorithm, due to radar imaging mechanisms such as tilt modulation and shadowing, a linear MTF with a constant exponent is usually required for wave spectrum correction [10]. Such an MTF is developed using an HH-polarized radar under deep water conditions, where the wave field can be safely assumed as stationary and homogeneous without severe interactions of wind sea and swell, and the variation of the exponent β_0 in

$$T_M(\left|\vec{k}\right|) = \left|\vec{k}\right|^{\beta_0} \tag{2.32}$$

due to range and azimuth can be neglected. However, under shallow water conditions such as may occur in near-shore regions, the linear MTF with a constant exponent may not work well due to the heterogeneity of the wave field. Therefore, Chen *et al.* [67] proposed a new quadratic polynomial MTF for near-shore regions using a VV-polarized radar. The MTF is fitted by a quadratic polynomial as

$$\log(\left|T_M(\left|\vec{k}\right|)\right|) = p_2\log^2(\left|\vec{k}\right|) + p_1\log(\left|\vec{k}\right|) + p_0, \tag{2.33}$$

where p_0, p_1, and p_2 are coefficients determined by least-squares fitting. Later, Qiu *et al.* [68] proposed another MTF with the same linear model as in [10], but considering the dependence of the exponent on range and azimuth. The range-and-azimuth-dependent variable exponent of the MTF, β_v, is given by

$$\beta_v = p_2 {r_a}^{p_1} \sin\theta_v + p_0, \tag{2.34}$$

where r_a is the range, and θ_v the angle between the radar look direction and peak wave direction.

The methods incorporating the new MTFs were tested using datasets collected on Haitan Island, China, from December 22, 2012 to January 6, 2013 and from January 12 to 18, 2013. Peak and mean wave periods were derived using both of the new MTFs and the traditional constant-exponent linear MTF. The comparison between the quadratic polynomial MTF and the linear MTF with an exponent of -0.55 involved 520 measurements [67]. Compared to the buoy measurements, the RMS difference of peak wave periods derived using the quadratic polynomial MTF was 0.88 s, which was similar to that of 0.74 s derived with a constant-exponent linear MTF. The RMS difference of mean wave periods derived using the quadratic polynomial MTF was 0.53 s, which was 0.50 s better than that using the constant-exponent linear MTF. For the comparison between the variable-exponent linear MTF and the linear MTF with an exponent of -1.2, only the data with H_S higher than 2 m were used [68]. During the test, the buoy-measured peak and mean wave periods varied from 7 s to 11 s and from 6.5 s to 9 s, respectively. The RMS differences of the peak and mean wave periods for the variable-exponent linear MTF were 0.95 s and 0.48 s, respectively, which were improved by 2.24 s and 2.21 s, respectively, over the constant-exponent linear MTF. The results indicated that the new MTFs may be more suitable for near-shore regions where the ocean wave field is heterogeneous.

E. Adaptive recursive positioning

In the traditional 3D-DFT-based algorithm for wave measurements, since radar backscatter is dependent on the azimuthal direction, sub-image sequences located in different azimuthal directions may lead to different wave measurement results. This problem has been mitigated by averaging wave spectra derived from several sub-image time series evenly distributed in azimuth in the radar FOV [69]. Recently, Al-Habashneh *et al.* [70] proposed an adaptive recursive positioning method (ARPM) to further improve wave measurements, especially under bimodal sea states (wind wave and swell).

In the first step, an initial directional wave spectrum is derived using three sub-image time series evenly distributed in azimuth in the radar FOV as in the traditional algorithm. Then, azimuthal directions of spectral peaks can be determined from the directional wave spectrum. In the next iteration, sub-image time series located in those azimuthal directions determined from the previous iteration are used to derive a new directional wave spectrum. Final wave spectra and related wave parameters are determined after three iterations.

The ARPM in [70]was tested using datasets collected from ship-borne Decca and Furuno X-band marine radars near Halifax, Nova Scotia, off East Coast of Canada, on November 27, November 29, December 1, and December 3, 2008. The performance was validated by calculating correlation coefficients between radar-derived and buoy-measured wave spectra on a discrete frequency grid. Compared to the traditional 3D-DFT-based algorithm, the ARPM produced an improvement of 9.8% in the averaged correlation coefficient. The accuracies for wave period and peak wave direction estimations were also enhanced by 15% to 30% and 6°, respectively. Although, due to the iterations, additional computational time is needed for the ARPM, real-time applications can still be realized. A limitation of the ARPM is that its best performance requires a full radar FOV. If the radar FOV is partially obstructed, it may not improve the wave measurement over the traditional 3D-DFT-based algorithm.

F. Geometrics-based SNR estimation

The standard SNR-based H_S estimation requires the surface current velocity to be determined in order to separate the wave components from the noise in the image spectrum [24]. However, possible inaccuracies in the determination of surface current may lead to erroneous SNR, thus affecting the H_S estimation. Wang *et al.* [71] proposed an algorithm to derive the SNR based on the geometrics of the linear wave dispersion relationship, which does not require the surface current determination.

A 3D image spectrum is first obtained by the application of a 3D DFT to a sub-image time series. With the assumption of deep water condition, two arbitrary points located on the linear dispersion curve in an $\omega - k$ plane, $(\vec{k_1}, \omega_1) = (k_{1x}, k_{1y}, \omega_1)$ and $(\vec{k_2}, \omega_2) = (k_{2x}, k_{2y}, \omega_2)$, satisfy

$$\begin{cases} \omega_1 = \sqrt{g\left|\vec{k_1}\right|} + k_{1x}u_x + k_{1y}u_y \\ \omega_2 = \sqrt{g\left|\vec{k_2}\right|} + k_{2x}u_x + k_{2y}u_y \end{cases}, \tag{2.35}$$

where $\vec{U} = (u_x, u_y)$ is the surface current vector. Based on the geometric relationship, a parameter α_k can be defined as

$$\alpha_k = \frac{k_{1x}}{k_{2x}} = \frac{k_{1y}}{k_{2y}} = \frac{\left|\vec{k_1}\right|}{\left|\vec{k_2}\right|}, \tag{2.36}$$

and (2.35) and (2.36) lead to

$$\omega_2 = \frac{1}{\alpha_k}(\omega_1 - (1 - \sqrt{\alpha}_k)\sqrt{g\left|\vec{k_1}\right|}). \tag{2.37}$$

Then, for any given point $(\vec{k_1}, \omega_1)$, a set of curves can be obtained as

$$\omega = \frac{\left|\vec{k}\right|}{\left|\vec{k_1}\right|}(\omega_1 - (1 - \sqrt{\frac{\left|\vec{k_1}\right|}{\left|\vec{k}\right|}})\sqrt{g\left|\vec{k_1}\right|}). \tag{2.38}$$

An example of these curves can be found in [72]. Of all the curves in each $\omega - k$ plane, those satisfying

$$\sum_{i=1}^{M_c} G_c(m_{ci}, n_{cj}) \geq 0.5 \max\{\sum_{i=1}^{M_c} G_c(m_{ci}, n_{c(j-1)}), \sum_{i=1}^{M_c} G_c(m_{ci}, n_{c(j+1)})\} \tag{2.39}$$

are first extracted. $G_c(m_c, n_c)$ is the m_cth spectral value on the n_cth curve, which is obtained using the nearest-neighbour interpolation. Then, the extracted curves satisfying

$$n_{cj} \leq \left| \frac{1}{N_c} \sum_{i=1}^{N_c} n_{ci} - 4 \right|, \tag{2.40}$$

where N_c is the total number of the curves extracted using (2.39), are determined to be associated with the dispersion relationship. Other curves are associated with noise. Therefore, the signal and noise can be separated for each $\omega - k$ plane, and the SNR can be derived for the H_S estimation.

The geometrics-based SNR estimation algorithm was tested with datasets collected at Zhoushan City, Zhejiang Province, China, from January 6 to 12, 2014, with H_S varying from 0.5 m to 2 m [71]. Both the geometrics-based algorithm and standard SNR-based method were applied to the datasets. As compared to the buoy reference, the correlation coefficient and the RMS difference of the retrieved H_S using the geometrics-based algorithm were 0.89 and 0.19 m, respectively, which were improved by 0.06 and 0.03 m, respectively, over the standard SNR-based method.

2.2.1.2 2D Continuous Wavelet Transform-Based Algorithms

A. Original algorithm

For wave extraction using the 3D-DFT-based algorithms mentioned above, the homogeneity within the observed area is assumed. Such an assumption is safe under deep water conditions without severe interactions of wind sea and swell. However, in coastal areas with shallow water, heterogeneities may exist because of the varying topography. Therefore, Chuang *et al.* [73] and Wu *et al.* [74] applied a 2D continuous wavelet transform (CWT) to X-band marine radar images to obtain ocean wave spectra.

The 2D CWT of an image $s(\vec{\gamma})$, where $\vec{\gamma} = (x, y)$ represents the coordinates in the image, may be expressed as [75]

$$W(\vec{b}, \varphi, a) = C_{\Psi}^{-1/2} a^{-1} \int_{R^2} \Psi^*(a^{-1} r_{-\varphi}(\vec{\gamma} - \vec{b})) s(\vec{\gamma}) d^2\vec{\gamma}, \tag{2.41}$$

where C_{Ψ} is a constant denoting that the mother wavelet function Ψ satisfies the admissibility condition, $\vec{b} = (b_x, b_y)$ the translation parameter, a the dilation parameter, and $r_{-\varphi}$ the rotation matrix, which is defined as

$$r_{-\varphi} = \begin{pmatrix} \cos\varphi & \sin\varphi \\ -\sin\varphi & \cos\varphi \end{pmatrix}. \tag{2.42}$$

In [74], the Morlet wavelet is selected as the mother wavelet function because of its directionality. By simplifying the Morlet wavelet with the peak wavenumber in the non-dimensional Fourier space at $\vec{k_0} = (k_{0_x}, k_{0_y}) = (6, 0)$ and the anisotropy matrix of $diag[1, 1]$, its Fourier transform is given by

$$\hat{\Psi}(\vec{k}_{non}) = e^{-0.5\left|\vec{k}_{non} - \vec{k_0}\right|^2}, \tag{2.43}$$

where $\vec{k}_{non}$ is the wavenumber in the non-dimensional Fourier space. For the application to the digital X-band marine radar image, the 2D CWT in (2.41) may be expressed in discrete form as

$$W(b_{x_u}, b_{y_v}, \varphi_m, a_n) = C_{\Psi}^{-0.5} a_n^{-1} \sum_{p=1}^{N_x} \sum_{q=1}^{N_y} \Psi^*[a_n^{-1} r_{-\varphi_m}(x_p - b_{x_u}, y_q - b_{y_v})] \cdot s(x_p, y_q) \Delta x \Delta y, \tag{2.44}$$

where b_{x_u}, b_{y_v}, φ_m, and a_n are the discrete forms of b_x, b_y, φ, and a, respectively, N_x and N_y are the total pixel numbers in x and y directions, respectively, and Δx and Δy are the image resolutions in x and y directions, respectively. To reduce the computation time, the

CWT can be calculated in the Fourier space, resulting in

$$W(b_{x_u}, b_{y_v}, \varphi_m, a_n) = \\ C_\Psi^{-0.5} a_n \sum_{p=1}^{N_x} \sum_{q=1}^{N_y} e^{i(b_{x_u} k'_{x_p} + b_{y_v} k'_{y_q})} \cdot \hat{\Psi}^*[a_n r_{-\varphi_m}(k'_{x_p}, k'_{y_q})] \hat{s}(k'_{x_p}, k'_{y_q}) \cdot \Delta k'_x \Delta k'_y, \tag{2.45}$$

where $\hat{s}$ is the Fourier transform of s, $\vec{k'} = (k'_x, k'_y)$ is the wavenumber in the dimensional Fourier space, and $\Delta k'_x$ and $\Delta k'_y$ are the wavenumber resolutions in the dimensional Fourier domain. If the sampling resolution is Δx and the total sampling number is N_S in the space domain, and the total length of the Morlet wavelet function in the non-dimensional space is $2D_M$, after dilation with a_n and rotation with $r_{-\varphi_m}$, the peak wavenumber in the dimensional Fourier space can be calculated as

$$\vec{k'} = \frac{\overrightarrow{k_0}}{(a_n r_{-\varphi_m})} \cdot \frac{2D_M}{N_S \Delta x}. \tag{2.46}$$

With (2.46), $W(b_{x_u}, b_{y_v}, \varphi_m, a_n)$ can be transformed to $W(b_{x_u}, b_{y_v}, \vec{k'})$. Therefore, the local wavenumber spectrum at position (b_{x_u}, b_{y_v}) is $W(\vec{k'})$.

X-band radar images used to verify the 2D-CWT based algorithm were collected in the southern part of Taiwan [74]. The directional wave spectra derived by the 2D-CWT based algorithm showed local ocean wave features at different locations of radar images. Furthermore, compared to the Fourier transform, the normalized 1D wavenumber spectrum derived using the 2D-CWT based algorithm agreed better with that measured by an *in-situ* buoy.

B. Self-adaptive 2D-CWT

In the original 2D-CWT based algorithm, the effect of ocean wave conditions on the selection of wavelet parameters is not considered. It is shown in [76] that the dilation parameter may affect wave extraction, and a look-up table is constructed for selecting the dilation parameter values according to different wave conditions. However, the wave

data collected by external sensors are used to make such a table. Later, An *et al.* [27] proposed a self-adaptive 2D-CWT-based algorithm for wave extraction by selecting the dilation parameter adaptively.

In Section 2.2.1.2-A, since $\vec{k_0} = (k_{0_x}, k_{0_y}) = (6,0)$, with $\varphi_m = 0^\circ$, it can be obtained from (2.46) that

$$k'_x = \frac{2D_M k_{0_x}}{a_n N_S \Delta x}. \tag{2.47}$$

Assuming that the minimum value of k'_x is given by

$$k'_{x_{\min}} = \beta \Delta k'_x, \tag{2.48}$$

the maximum value of a_n is regulated by a calibration parameter β through

$$a_{\max} = \frac{2D_M k_{0_x}}{N_S \Delta x \beta \Delta k'_x}. \tag{2.49}$$

A look-up table for determining β with different mean wave periods T_{01} is provided in [76]. The values of β in the table are based on an image resolution Δx of 10.5 m and a sub-image length N_x of 128. For a different image resolution Δx_n and a different sub-image length N_{x_n}, β_n may be modified as

$$\beta_n = \beta \frac{N_{x_n} \Delta x_n}{N_x \Delta x}. \tag{2.50}$$

In the algorithm for selecting appropriate β, a sub-image is first selected and normalized. Then, an image spectrum is obtained by applying the 2D CWT with an initial value of β (e.g., 1.4 for $\Delta x = 10.5$ and $N_x = 128$). Next, the 1D frequency wave spectrum $E(f)$ and the mean wave period T_{01} are derived. If any peak above a threshold exists at the left side of the major peak of $E(f)$, it is regarded as a false peak. If a false peak exists, the value of β is increased by $\Delta\beta$ and the 2D CWT is applied to the normalized sub-image again. If no false peak exists, the calculated T_{01} is compared with that in the look-up

table for the corresponding β. If the difference between the two periods is larger than a threshold ξ (if $T_{01} < 10$ s, $\xi = 0.5$; otherwise, $\xi = 1$), the value of β is increased by $\Delta\beta$ and the 2D CWT is applied to the normalized sub-image again. If the difference is not larger than ξ, β is selected as the appropriate value for the wave extraction using the 2D-CWT-based algorithm.

Both the traditional 3D-DFT-based and self-adaptive 2D-CWT-based algorithms were applied to the datasets that are described in Section 2.2.1.1-C [27]. The results from both the land-based and ship-borne radar data showed that the wave spectra and wave parameters derived using both algorithms agreed well with buoy records. Furthermore, for the ship-borne radar data, taking the buoy data as ground truth, the RMS differences of H_S, mean wave period, and wave direction derived from the traditional 3D-DFT-based and self-adaptive 2D-CWT-based algorithms were 0.53 m and 0.61 m, 1.91 s and 1.51 s, and 22.96° and 24.18°, respectively. During this experiment, the buoy-measured H_S, mean wave period, and wave direction were about 2 m to 3.5 m, 7 s to 10 s, and 100° to 120°, respectively. Although the results indicated the applicability of the self-adaptive 2D-CWT-based algorithm, some limitations of the algorithm still exist. Firstly, the computational cost of the algorithm is expensive. Secondly, the effect of surface current is not considered. Thirdly, the directional ambiguity cannot be eliminated by the 2D CWT analysis of a single radar image.

2.2.1.3 Array Beamforming Algorithm

Ma *et al.* [77] proposed an array beamforming algorithm to extract the directional wave spectrum and related wave parameters from X-band radar image time series. Beamforming is a technique that extracts the signal arriving from a desired direction through constructive interference and suppresses other signals through destructive interference [78]. In this algorithm, image pixels are considered as elements in an antenna array, and image pixel intensities are considered as signals received by the elements. The advantages

of this algorithm are that no coordinate transformation and MTF are required, and the effects of shadowing modulation and moving vessels in the image can be suppressed.

A signal received at the reference element of an antenna array and at time t with angular frequency ω, arriving direction ϕ, and amplitude $u_{\omega,\phi}$ can be expressed as

$$s_{\omega,\phi}(t) = u_{\omega,\phi} e^{j\omega t}. \tag{2.51}$$

For the ith antenna in the antenna array, the received signal may be

$$s_{\omega,\phi}(t - \tau_{\omega,\phi,i}) = u_{\omega,\phi} e^{j\omega(t-\tau_{\omega,\phi,i})} = s_{\omega,\phi}(t) e^{-j\omega\tau_{\omega,\phi,i}}, \tag{2.52}$$

where $\tau_{\omega,\phi,i}$ is the time delay of the received signal between the ith antenna and the reference antenna. Assuming that $X_\omega(t)$ is an $A \times 1$ array, representing the signals with different directions received by an antenna array of A antennas, the beamforming result for direction ϕ may be expressed as

$$y_{\omega,\phi}(t) = a^H_{\omega,\phi} X_\omega(t) \approx A s_{\omega,\phi}(t), \tag{2.53}$$

where H is the conjugate transpose operator, and $a_{\omega,\phi}$ is the steering vector, which is given by

$$a_{\omega,\phi} = \left[e^{-j\omega\tau_{\omega,\phi,1}}, e^{-j\omega\tau_{\omega,\phi,2}}, \ldots, e^{-j\omega\tau_{\omega,\phi,A}}\right]^T, \tag{2.54}$$

Then, the expectation of the signal power may be estimated as

$$P_{\omega,\phi} = E\left[\left|y_{\omega,\phi}(t)\right|^2\right] \approx A^2 u^2_{\omega,\phi}. \tag{2.55}$$

For X-band radar sea surface imaging, $s_{\omega,\phi}(t)$ may represent the sea surface waves, and $X_\omega(t)$ may represent the complex image pixel intensities. A circular antenna array is selected for this algorithm, and by considering the radar image pixel as the antenna, an

approximate circular array is constructed by the pixels located within a circle. $X_\omega(t)$ can be obtained by applying an all-phase fast Fourier transform (ApFFT), which significantly improves the phase spectrum accuracy [79] to image intensity time series at each pixel. $\tau_{\omega,\phi,i}$ can be obtained by

$$\tau_{\omega,\phi,i} = \frac{\vec{k}(\omega,\phi)\cdot\vec{d_i}}{\omega}, \tag{2.56}$$

where $\vec{d_i}$ is the space vector from the reference pixel Q_0 to the ith pixel Q_i with $\vec{Q_0Q_i} = \vec{d_i}$, and $\vec{k}(\omega,\phi)$ is the wavenumber vector derived using the dispersion relationship with current effects. Current may be retrieved by seeking the maximum total power, which is

$$P_T = \sum_{\omega}\sum_{\phi} E^{(2)}(\omega,\phi)\Delta\omega\Delta\phi, \tag{2.57}$$

where $E^{(2)}(\omega,\phi)$ is the directional wave spectrum calculated as

$$E^{(2)}(\omega,\phi) = \frac{u^2_{\omega,\phi}}{2\Delta\omega\Delta\phi}, \tag{2.58}$$

and $\Delta\omega$ and $\Delta\phi$ are the angular frequency and direction resolutions, respectively. It is found that, as a function of current speed and direction, P_T reaches a maximum on the actual current speed and direction. Therefore, for the current estimation, the current speed-direction grids are first divided into sub-blocks. P_T on the center of each sub-block is calculated, and the maximum P_T is identified. Then, for the sub-block with the maximum P_T, the division and calculation are repeated until the final maximum P_T is obtained, and the current velocity associated with the final maximum P_T is taken to be the actual current velocity. Then, wave parameters such as wave directions and periods can be derived from the wave spectrum. H_S is estimated based on the SNR using (2.29), where the signal energy can be calculated from $E^{(2)}(\omega,\phi)$, and the noise energy is estimated as the subtraction of the signal energy from the total energy, which is derived from the mean of the power spectrum at each pixel. Fig.2.4illustrates the basic steps of the array beamforming algorithm.

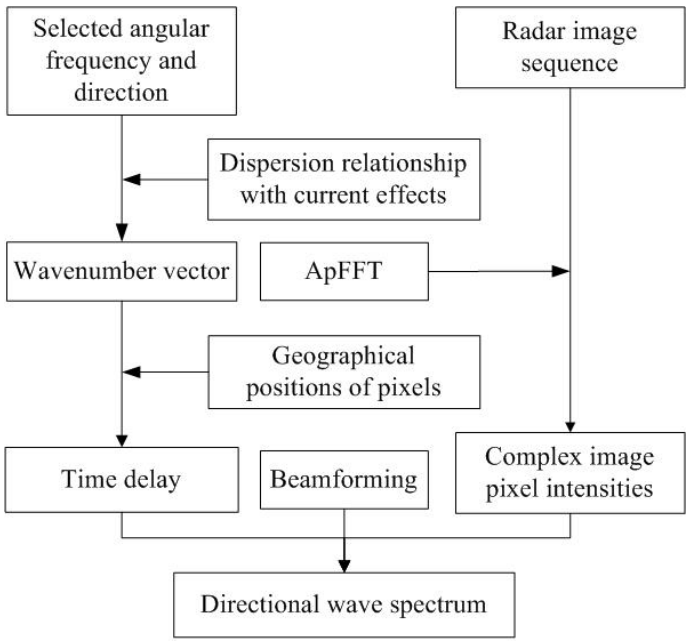

Fig. 2.4 Basic steps of the array beamforming algorithm.

An experiment was conducted in Zhoushan, China, on January 8, 9, 10, and 12, 2014 [77]. During the experiment, buoy-measured H_S, mean wave period, and peak wave direction ranged from 0.5 m to 2 m, 4 s to 7 s, and 50° to 250°, respectively. For 45 buoy-radar comparison pairs, the correlation coefficient and RMS difference of the mean wave period, peak wave direction, and H_S are 0.95 and 0.28 s, 0.9 and 15.14°, and 0.95 and 0.12 m, respectively. Moreover, the wave spectrum derived by the array beamforming algorithm is similar to that derived by the traditional DFT-based method with an MTF. The novel array beamforming algorithm utilizes the beamforming technique based on individual image pixels, suppressing the effects of shadowing modulation and moving vessels in the images. The coordinate transformation and MTF can also be avoided. In the future, the validation of the algorithm for ship-borne radar applications with higher encounter current speed and for heterogeneous wave fields may be required.

2.2.2 Texture-Analysis Based Techniques

Another class of algorithms for wave measurements is based on the texture analysis of radar sea surface images. Wave parameters, such as H_S, are derived directly from the image texture without the estimation of wave spectra.

2.2.2.1 Illumination Probability

A model that relates H_S to the crest-to-trough length ratio extracted from the radar image and a threshold probability of illumination (P_0) was first proposed in [80] for estimating H_S. Crests and troughs in the radar image represent illuminated areas reflected from visible wave portions and shadowed areas with no reflections, respectively. In [81], Buckley and Aler validated this model by assuming a constant P_0 based on the theory of geometric optics [82]. The essence of the theory is that, for a constant P_0, the crest-to-trough ratio decreases as the wave height increases. Later, Buckley and Aler [83] enhanced the H_S determination utilizing a varying P_0. Based on the assumption that P_0 decreases as wave height increases, a linear relationship between P_0 and the mean image intensity in the up-wave direction was found. Then, a P_0 that varies with mean image intensity values was used in the model for the H_S estimation. According to the test using datasets collected in the southern Labrador Sea from January 30 to March 17, 1997 [81, 83] and a varying P_0, the correlation coefficient and the mean difference between the radar-derived and wavemeter-measured H_S were improved from 0.54 to 0.67, and from 28% to 20%, respectively, over that with a constant P_0. In this method, illuminated and shadowed areas in the radar image are exploited to estimate H_S. However, an external sensor is required for the calibration. Later, an algorithm, which does not require calibration and is also based on shadowing analysis incorporating sea surface slope and mean wave period, was proposed [27].

2.2.2.2 Statistical Analysis

Gangeskar [84] estimated the wave height through analyzing the texture of radar images. The connection between H_S and various parameters derived from the statistical analysis of images was investigated. Datasets used to test the algorithm were collected from the Gullfaks C (GFC) oil production platform in the North Sea, with H_S ranging from 0.5 m to 9 m [84]. 17 statistical parameters were used to estimate H_S. The average absolute correlation coefficient between the radar-derived and reference H_S were 0.65 and 0.67, respectively, for the Cartesian start ranges (CSR) of 1500 m and 900 m. The best result was obtained using the parameter of the number of extrema per area in the smoothed image, with the standard deviations of 0.99 m for the CSR of 1500 m and 0.98 m for 900 m.

Later, Gangeskar [85] developed an adaptive method incorporating a scheme for detecting problematic situations such as low wave height and precipitation. In this adaptive method, different parameters were selected to estimate wave height according to the data quality identification results. Under good conditions, the parameter of extrema number is used, while under precipitation or low wave height, the parameter of gray level co-occurrence matrix (GLCM) correlation [85] is used. The result provided by the same datasets as in [84] showed that by using the adaptive method, the standard deviations were reduced to 0.68 m and 0.77 m for the CSR of 1500 m and 900 m, respectively. Although precipitation may affect radar images by inducing noise, the adaptive method still permits H_S estimation.

2.2.2.3 Tilt-Based Algorithm

In most of the aforementioned cases, the algorithmatic outputs require calibration by additional reference sensors such as wave buoys. Dankert and Rosenthal [55, 86] proposed an algorithm to determine ocean surface elevations based on tilt modulation

without calibration. In their method, both hydrodynamic and shadowing modulations are considered to be insignificant to the radar imaging mechanism.

First, each image in a radar image sequence is corrected with a 2D antenna pattern, which is obtained from the temporal average of all the radar images. Next, a third-order polynomial $f(r_a, \theta)$, where r_a is the range, is least-squares fitted to the mean RCS for each azimuthal direction θ. With the given antenna height h_{ant}, the depression angle as a function of range can be calculated as

$$\widetilde{\psi}(r_a) = \arctan(\frac{h_{ant}}{r_a}). \tag{2.59}$$

The local ocean surface tilt $\varphi(r_a, \theta)$, which is assumed to be equal to the change of the local depression angle, can be obtained as

$$\varphi(r_a, \theta) = \psi(r_a, \theta) - \widetilde{\psi}(r_a), \tag{2.60}$$

where $\psi(r_a, \theta)$ is the local depression angle, which can be determined as

$$\psi(r_a, \theta) = \widetilde{\psi}(f^{-1}(\sigma_{r_a}, \theta)), \tag{2.61}$$

where σ_{r_a} is the local RCS at range r_a, and f^{-1} is the inverse function of f. The local tilt angles are derived for all the images of an image sequence, resulting in a tilt image sequence. Finally, the ocean surface elevation is derived by convolving tilt images with a 2D integration filter kernel. Here, the convolution in the spatial domain is realized by the multiplication of the 3D DFT of the tilt image sequence and the integration transfer function in the Fourier domain. Then, the dispersion relationship with current effects and a 3D Gabor filter are used to extract the 3D wave spectrum. The ocean surface elevation is obtained by applying an inverse 3D DFT to the 3D wave spectrum.

The algorithm was tested using datasets collected in the central North Sea from February to September 2001 [86, 55]. During the test, H_S measured by *in-situ* sensors

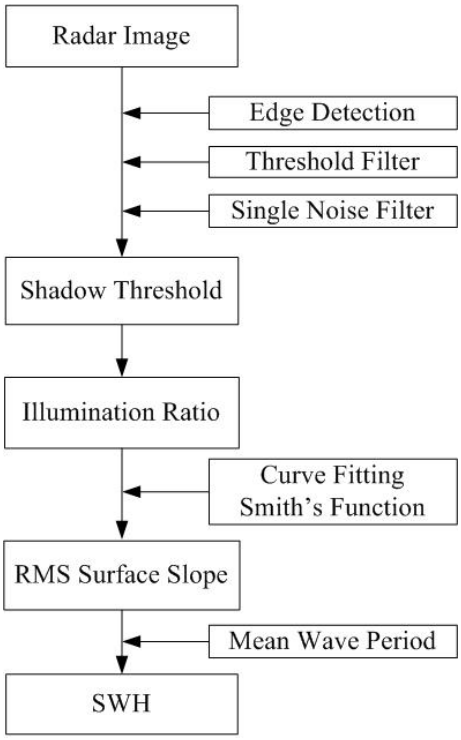

Fig. 2.5 Basic steps of the shadowing-based algorithm.

varied from 0.5 m to 6 m. For the 1535 comparison pairs of the radar-derived and *in-situ* sensor-measured H_S, a correlation coefficient of 0.94 and a standard deviation of 0.35 m were obtained. However, since shadowing modulation cannot be neglected for X-band radars operating at grazing incidence, the algorithm may not be suitable for the standard X-band marine radar mounted closer to sea level.

2.2.2.4 Shadowing-Based Algorithms

A. Original algorithm

Gangeskar [25] proposed an algorithm for the H_S estimation based on shadowing analysis. This algorithm also does not require calibrations using external sensors. Furthermore, it is suitable for X-band marine radars operating at grazing incidence. Basic steps of the shadowing-based algorithm are shown in Fig.2.5

For each radar image, an edge detection technique is first used to identify the edges that separate the shadowed areas and illuminated areas. Here, this is performed by

convolving a raw polar radar image $I(m,n)$ with a simple pixel difference operator $H_i(m,n)$ where H_i is the ith discrete directional first derivative operator, and i ranges from 1 to 8. m and n are row and column, respectively. The edge image obtained by convolving along the ith direction is $I_{E_i}(m,n)$ and is given by [87]

$$I_{E_i}(m,n) = I(m,n) \circledast H_i(m,n). \tag{2.62}$$

Since the result of (2.62) represents the intensity level difference of a pixel from its neighboring pixels, and the intensity level of an edge pixel that separates shadow and no shadow usually differs from its adjacent pixels more than other pixels, the eight edge images are thresholded using a threshold value equal to the upper B-percentile ($B = 10$ in [25]) of the pixel intensity levels in each image (i.e., $I_{E_i}(m,n)$). Pixels with intensity levels higher and lower than (or equal to) the threshold are assigned the value of 1 and 0, respectively. This results in eight thresholded edge images $I_{T_i}(m,n)$. An overall edge image $I_F(m,n)$ is obtained next by summing the eight thresholded edge images $I_{T_i}(m,n)$ and then filtering as

$$I_T(m,n) = \sum_{i=1}^{8} I_{T_i}(m,n) \tag{2.63}$$

$$I_F(m,n) = \begin{cases} 1, & I_T(m,n) \in [1, \tau_F] \\ 0, & \text{otherwise.} \end{cases} \tag{2.64}$$

The purpose of the filtering is to remove the single pixel noise having edges in more than τ_F directions. For example, if a pixel has edges in all directions, it will be considered as noise rather than an edge, and will be set as 0 in the edge image. The raw radar image pixels corresponding to the pixels of intensity value of 1 in $I_F(m,n)$ are used to create a statistical distribution $F_H(\eta)$ of edge pixel gray level values η. From the distribution, the shadow threshold τ_S can be determined as the intensity level corresponding to the

highest occurrence in the pixels selected for statistical distribution analysis. That is,

$$\tau_S = \text{mode}(F_H(\eta)). \tag{2.65}$$

It should be noted that $F_H(\eta)$ is created individually for each radar image, and τ_S is also determined based on $F_H(\eta)$ for each radar image. Using the estimated shadow threshold τ_S, the shadow image can be derived. Pixels with intensity levels lower than or higher than or equal to τ_S are regarded as shadowed or illuminated, respectively. The shadow image is then divided into segments along the range and the azimuth. Each segment covers 30 m in range and 10° in azimuth. For each segment, the illumination ratio $L(\gamma)$, which is defined as the ratio of the number of pixels corresponding to the illuminated areas to the total number of pixels, is calculated as a function of grazing angle γ. With the obtained illumination ratios, the RMS surface slope σ_{RMS} of a random rough surface described by a one-dimensional Gaussian surface height probability density function (PDF) can be derived by curve fitting Smith's function for each azimuth direction [88]. The Neilder-Mead simplex method in one dimension is implemented for the curve fitting [89]. After σ_{RMS} are obtained for all azimuth directions, an average RMS surface slope σ^A_{RMS} can be calculated. Finally, from the average RMS surface slope σ^A_{RMS} and the average zero-crossing wave period T_{m02}, H_S can be determined as

$$H_S = \frac{\sigma^A_{RMS} g T^2_{m02}}{\sqrt{2}\pi}. \tag{2.66}$$

T_{m02} can be derived from the radar images themselves using existing wave algorithms [37, 38].

The algorithm was tested using datasets collected at Veslefrikk platform in the North Sea in January 2008 [25]. The correlation coefficient between the radar-derived and reference H_S was 0.87. The shadowing-based algorithm is totally based on theory and does not require calibration with additional sensors. However, in [25], the test was

conducted using the average zero-crossing wave period T_{m02} measured by a reference sensor. Therefore, the algorithm needs to be further validated using the radar-derived average zero-crossing wave period T_{m02} in order to be fully independent of external sensors. In addition, the height of the radar used in the test [25] was 43.2 m, which was higher than the regular marine radar height of 20-30 m. Since the radar height affects the grazing angles and shadowing, the algorithm also needs to be validated using a regular marine radar.

B. Water-depth considerations

Since (2.66) is valid only under deep water conditions, Wei *et al.* [90] modified the shadowing-based algorithm in [25] by considering water depth for its application to a coastal area as

$$H_S = \begin{cases} \frac{\sigma^A_{RMS} g T^2_{m02}}{\sqrt{2}\pi}, \frac{d_w}{\lambda} \geq x_2 \\ \frac{\sigma^A_{RMS} g T^2_{m02}}{\sqrt{2}\pi}\left(\sqrt{0.0437 + 1.2899\frac{d_w}{T^2_{m02}}} + 0.2096\right), x_1 \leq \frac{d_w}{\lambda} \leq x_2 \\ \sqrt{2}\sigma^A_{RMS}\sqrt{g d_w}, \frac{d_w}{\lambda} \leq x_1 \end{cases}, \tag{2.67}$$

where d_w is the water depth, and λ is the wavelength of ocean waves. $x_1 = 0.098$ and $x_2 = 0.289$ are determined by minimizing the RMS error between the function $\tanh(kd)$ and the piecewise linear function approximated to it. The water-depth-incorporated shadowing-based algorithm was tested using the datasets acquired at the coastal area of Haitan Island in Fujian Province from October to November 2010 and from November 2014 to January 2015 [90], with H_S ranging from 0.5 m to 5 m. The correlation coefficient and the RMS difference between the H_S measured by the water-depth-incorporated algorithm and buoy are 0.68 and 0.51 m, respectively, while those for the original algorithm are 0.53 and 0.58 m, respectively.

2.2.2.5 Support Vector Regression Algorithm

Salcedo-Sanz *et al.* [91] estimated H_S using a support vector regression (SVR) algorithm and shadowing information from simulated and field X-band marine radar images. In this algorithm, the SVR is trained from the simulated data and applied to field data. Calibrations using external sensors can thus be avoided. A classical model, ε-SVR [92], is considered in this algorithm. Shadow probability and the tangent of the local incident angle are included in the SVR training scheme using the simulated data. Shadowing probability is obtained as the ratio of the number of shadowed pixels to the number of total pixels. The tangent of the local incident angle is determined from the radar range, wave elevation, and antenna height above the sea surface.

After the training phase using the simulated data, the SVR is applied to field data collected at the German research platform of FINO 1 in the German basin of the North Sea in 2006 and 2013 [91]. As compared to the ground truth, the mean absolute error (MAE) and mean square error (MSE) of H_S obtained with the SVR algorithm were 0.66 m and 0.82 m, respectively, for data acquired in 2006 with H_S varying from 2 m to 9 m. For data acquired in 2013 with H_S varying from 2 m to 6 m, the MAE and MSE were 0.50 m and 0.38 m, respectively.

2.2.2.6 Empirical Orthogonal Function-Based Algorithms

A. Principal component

Chen *et al.* [26] proposed an empirical orthogonal function (EOF)-based algorithm for wave measurements using X-band marine radar. Wave parameters, including H_S, peak wave period, wavelength, and wave direction were determined from the principal components (PCs) of the radar image sequence derived from the EOF.

First, a 2D time-space image sequence can be represented by

$$I_{TS} = \begin{bmatrix} i_{11} & i_{12} & \cdots & i_{1D} \\ i_{21} & i_{22} & \cdots & i_{2D} \\ \vdots & \vdots & \ddots & \vdots \\ i_{C1} & i_{C2} & \cdots & i_{CD} \end{bmatrix}, \tag{2.68}$$

where C is the sample number in space, and D the sample number in time. After the application of EOF [93,94], I_{TS} can be decomposed as

$$I_{TS} = VZ. \tag{2.69}$$

Each column of V is one eigenvector of the matrix $I_{TS}I_{TS}^T$. The jth eigenvector can be expressed as

$$v_j = (v_{1j,}v_{2j,}\cdots,v_{Cj})^T. \tag{2.70}$$

Each row of Z is one PC of the 2D time-space image sequence I_{TS}, representing the variation of waves in the time domain. The kth PC can be expressed as

$$z_k = (z_{k1,}z_{k2,}\cdots,z_{kD}). \tag{2.71}$$

For H_S estimation, a linear relationship between H_S and the standard deviation of one PC, $std(z_k)$, is established as

$$H_S = p_0 + p_1 \cdot std(z_k), \tag{2.72}$$

where p_0 and p_1 are parameters which can be determined from the least-squares fitting. With the obtained linear relationship, H_S can be estimated from the standard deviation of one PC for any radar image sequence. Then, the first PC is used for the estimation of peak wave period. The maximum entropy method (MEM) [95] is used to derive the

power spectral density (PSD) of the first PC. The peak wave frequency f_p is determined as the frequency corresponding to the maximum PSD, and the peak wave period T_p is trivially determined as

$$T_p = \frac{1}{f_p}. \tag{2.73}$$

The process of estimating the peak wavelength is similar to that of estimating the peak wave period. The difference is that the 2D time-space image sequence to be decomposed by the EOF consists of C samples in time and D samples in space, as opposed to (2.68). After the decomposition, PCs can be obtained in the space domain, representing the spatial variation of waves. Then, the peak wavelength can be obtained from the PSD of the first PC derived by the MEM [95]. In the 2D space domain, two peak wavelengths along two orthogonal directions need to be derived, and the peak wavelength and wave direction can be obtained based on the geometric relationship. The ambiguity of 180° of the wave direction is removed by applying the 3D DFT to the image sequence. The wave direction is selected as the one close to the peak of the image spectrum.

The EOF-PC-based algorithm was tested using the same datasets collected from two experiments as described in Section 2.2.1.1-D [26]. During the experiments, buoy-measured H_S and peak wave period ranged from 0.5 m to 3.5 m and from 5 s to 11 s, respectively. The first experiment contained 364 measurements, and the second one contained 156 measurements. For the H_S estimation, the second experiment was used for training, and the first one was used for validation. For the validation data, the comparison of the radar-derived and buoy-measured H_S resulted in a correlation coefficient of 0.93 and a RMS difference of 0.21 m. For all data, the comparison of the radar-derived and buoy-measured peak wave period resulted in a correlation coefficient of 0.69 and a RMS difference of 0.84 s. By applying the EOF, the algorithm enables wave parameter estimation from heterogeneous ocean wave fields such as occur in near-shore regions. Also, the linear wave dispersion relationship and MTF are not required. However, a calibration process with an external sensor is still necessary for wave height estimation.

B. Rotated EOF

Since the first few PCs derived by the EOF may not represent the main modes of the wave field and wave parameters estimated from EOF analysis may be affected by the observed area and selected pixel positions, Yu *et al.* [96] and Zhang *et al.* [97] utilized a rotated EOF (REOF) to estimate H_S.

Assume that λ_j is the jth eigenvalue of the matrix $I_{TS}I_{TS}^T$ after the EOF, a diagonal matrix Λ is composed as

$$\Lambda = \begin{bmatrix} \lambda_1 & & & \\ & \lambda_2 & & \\ & & \ddots & \\ & & & \lambda_P \end{bmatrix}, P < C. \tag{2.74}$$

The sum of the fractional variances of the first P EOF modes is calculated as

$$G_P = \sum_{p=1}^{P} \frac{\lambda_p}{\sum_{j=1}^{C} \lambda_j}. \tag{2.75}$$

With P being selected as the lowest value that makes G_P greater than 85%, an initial factor loading matrix is obtained as

$$V'_{ini} = \begin{bmatrix} v_1 & v_2 & \cdots & v_P \end{bmatrix} \Lambda. \tag{2.76}$$

The initial factor loading matrix is then normalized by dividing each element at the c row by h_c^2, which is calculated as

$$h_c^2 = \sum_{p=1}^{P} (v_{cp}\lambda_p)^2. \tag{2.77}$$

The factor loading matrix V' is obtained by multiplying the normalized initial factor loading matrix with the orthogonal matrix

$$Q = \begin{bmatrix} q_{11} & q_{12} & \cdots & q_{1P} \\ q_{21} & q_{22} & \cdots & q_{2P} \\ \vdots & \vdots & \ddots & \vdots \\ q_{P1} & q_{P2} & \cdots & q_{PP} \end{bmatrix}. \tag{2.78}$$

If P is even, q_{pp} is $\cos\varphi$, q_{P1}, $q_{P-1,2}$,...,$q_{P/2,P/2+1}$ are $\sin\varphi$, q_{1P}, $q_{2,P-1}$,...,$q_{P/2+1,P/2}$ are $-\sin\varphi$, and other elements are 0. If P is odd, q_{pp} is $\cos\varphi$ except $q_{(P+1)/2,(P+1)/2}$ in which case it is 1, q_{P1}, $q_{P-1,2}$,...,$q_{(P-1)/2,(P-1)/2+1}$ are $\sin\varphi$, q_{1P}, $q_{2,P-1}$,...,$q_{(P-1)/2+1,(P-1)/2}$ are $-\sin\varphi$, and other elements are 0. φ is selected as the value that maximizes

$$M = \sum_{p=1}^{P} [\frac{1}{C} \sum_{c=1}^{C} \left(\frac{(v'_{cp})^2}{h_c^2} \right)^2 - \left(\frac{1}{C} \sum_{c=1}^{C} \frac{(v'_{cp})^2}{h_c^2} \right)^2], \tag{2.79}$$

where v'_{cp} is the element of V' at the cth row and the pth column. Then, the common factor matrix Z' is obtained from

$$I_{TS} = V'Z'. \tag{2.80}$$

Each row of Z' is one rotated PC of the 2D time-space image sequence I_{TS}. The qth rotated PC can be expressed as

$$z'_q = (z'_{q1,} z'_{q2,} \cdots, z'_{qD}). \tag{2.81}$$

Finally, H_S can be estimated from the standard deviation of one rotated PC, $std(z'_q)$, by training a linear model

$$H_S = p_0 + p_1 \cdot std(z'_q), \tag{2.82}$$

or a polynomial model

$$H_S = p_0 + p_1 \cdot (std(z_q'))^{1/2} + p_2 \cdot std(z_q') + p_3 \cdot (std(z_q'))^{3/2}, \tag{2.83}$$

where p_0, p_1, p_2, and p_3 are parameters determined through regression fitting.

The REOF-based algorithm was validated using the datasets collected in Bohai Bay, China from July 25 to 26, 2014, with H_S ranging from 0.5 m to 1.8 m [96, 97]. The correlation coefficient and RMS difference between the buoy-measured and radar-derived H_S from the REOF-based algorithm are 0.88 and 0.17 m, respectively, for the linear model, and 0.92 and 0.14 m, respectively, for the polynomial model. The EOF-PC-based algorithm was also applied to the same datasets. The corresponding correlation coefficient and RMS difference are 0.86 and 0.19 m, respectively. The results from the employed datasets indicated that the REOF-based algorithm improved the H_S estimation over the EOF-PC-based algorithm. However, a calibration process using an external sensor is still required.

C. Joint PDF

Later, by extending the EOF-PC-based algorithm, Chen *et al.* [98] developed an algorithm to retrieve wave heights from X-band marine radar image sequences based on the joint PDF of dimensionless wave periods and wave heights, without using external sensors for calibrations.

Based on (2.68) - (2.71), a dominant wave field may be reconstructed as

$$I_1 = v_1 z_1. \tag{2.84}$$

I_1 can be expressed in polar coordinates as $I_1(m,n)$. Since H_S is proportional to the standard deviation of PCs, $I_1(m,n)$ is rescaled as

$$I_1'(m,n) = \frac{I_1(m,n)}{\max[I_1(m,n)]} \cdot std(z_1). \tag{2.85}$$

Then, with the peak wave direction ϕ_p determined by using the traditional 3D-DFT-based method, the radial profile $I_1(m,\phi_p)$ is used to derive dimensionless wave periods and wave heights. Zero-crossing wavelengths are obtained by detecting crests and troughs from $I_1(m,\phi_p)$ as

$$l_{0_i} = r_{a_i} - r_{a_{i+1}}, \tag{2.86}$$

where r_{a_i} and $r_{a_{i+1}}$ are ranges corresponding to two neighbouring crests or troughs. Similarly, zero-crossing wave heights can be obtained as

$$h_{0_j} = a_c[I_1'(r_{a_j},\phi_p) - I_1'(r_{a_{j+1}},\phi_p)], \tag{2.87}$$

where r_{a_j} and $r_{a_{j+1}}$ are ranges corresponding to two neighbouring crests and troughs, and a_c is the coefficient to be determined in the following procedures. Zero-crossing wave periods t_{0_i} can be derived from l_{0_i} using the dispersion relationship. Subsequently, dimensionless wave periods are obtained as

$$\tau_{0_i} = \frac{t_{0_i}}{\overline{t_0}}, \tag{2.88}$$

where $\overline{t_0}$ is the average zero-crossing wave period. Dimensionless wave heights are obtained as

$$\alpha_{0_j} = \frac{h_{0_j}}{\overline{h_0}}, \tag{2.89}$$

where $\overline{h_0}$ is the average zero-crossing wave height. The joint PDF of dimensionless wave periods and wave heights for random ocean waves, $f(\alpha_h,\tau_t|\upsilon_0)$, is defined in [99, 100]. The spectral width parameter υ_0 is determined by fitting the histogram of dimensionless

wave periods in (2.88) to the theoretical PDF of dimensionless wave periods which is derived by integrating $f(\alpha_h, \tau_t|\upsilon_0)$ over α_h from 0 to 5 with a step of 0.001. With the derived υ_0, the theoretical PDF of dimensionless wave heights can be obtained by integrating $f(\alpha_h, \tau_t|\upsilon_0)$ over τ_t from 0 to 3 with a step of 0.001. Then, a parameter p_s is defined to quantify the shape of the PDF of a variable v as

$$p_s = \frac{E(v-\mu_v)^6}{\sigma_v^5}, \tag{2.90}$$

where μ_v is the mean of v, σ_v the standard deviation of v, and $E(\cdot)$ the expectation operator. The parameter p_s is calculated for the histogram of relative wave heights in (2.87) and the theoretical PDF of dimensionless wave heights as p_{s_r} and p_{s_t}, respectively. Finally, the coefficient a_c can be calculated as

$$a_c = \frac{p_{s_t}}{p_{s_r}}. \tag{2.91}$$

Accordingly, H_S can be determined as

$$H_S = a_c \cdot h_{0m}, \tag{2.92}$$

where h_{0m} is the wave height having the maximum probability. The basic overall steps of the joint-PDF-based algorithm are shown in Fig.2.6.

The joint PDF-based algorithm was tested using datasets collected on Haitan Island, China from October 2014 to January 2015, with H_S varying from 0.2 m to 3.5 m [98]. The datasets contained 671 measurements for HH-polarized radar and 548 measurements for VV-polarized radar. The correlation coefficient and the RMS difference for H_S derived from the HH-polarized radar and the buoy are 0.78 and 0.51 m, respectively, and those for the VV-polarized radar are 0.77 and 0.51 m, respectively. Wave height can be retrieved from the algorithm directly without using external sensors for calibration.

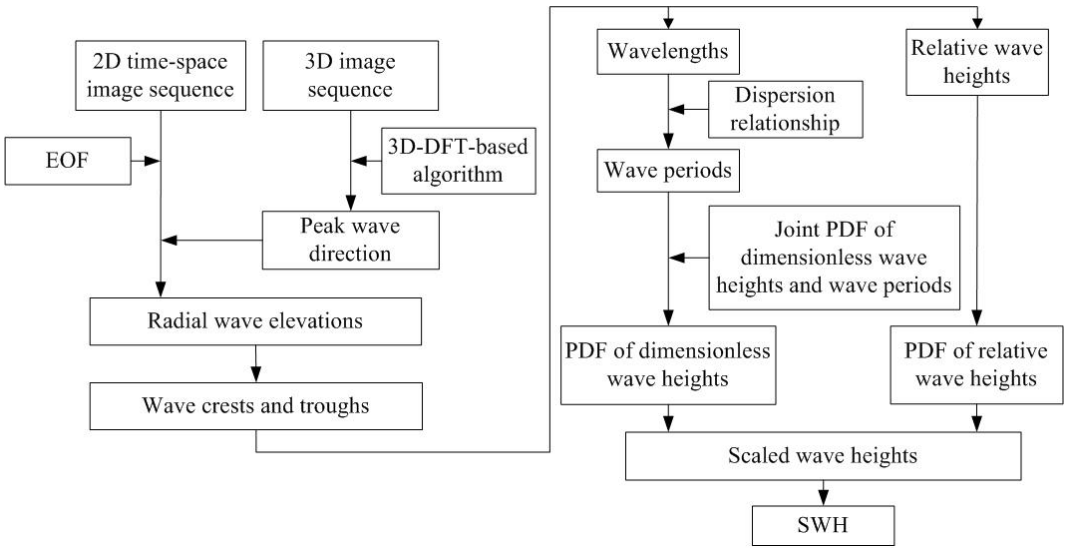

Fig. 2.6 Basic steps of the joint-PDF-based algorithm.

However, compared to the SNR- and shadowing-based algorithms, the accuracy of the joint PDF-based algorithm needs to be improved.

2.2.3 Summary

The inter-comparison of the reviewed techniques for wave measurements is listed in Table2.2. It may be observed from the table that wave height measurement is available for almost all the algorithms. However, most of them need calibrations using external sensors.

2.3 Chapter Summary

In this chapter, algorithms for ocean surface wind and wave measurements using X-band marine radar were reviewed.

For wind measurements, wind direction is generally determined from the upwind peak in images collected from HH-polarized X-band radars operating at grazing incidence; wind speed is generally determined from parameters related to the NRCS derived from the radar image. Recently, much effort has been focused on techniques for wind parameter

extraction from rain-contaminated radar data, and this may still be one of the future trends for wind measurements. Another remaining challenge for wind measurements is that a calibration phase using external sensors is generally required for wind speed estimation. In the future, calibration-free algorithms for wind speed estimation need to be developed. This may be realized by exploiting both the spatial and temporal variations of image patterns. Techniques such as the optical flow-based motion estimation in [57] may be further developed to measure the movements of wind gusts visible in images.

For wave measurements, various algorithms based on the spectral or texture analysis of radar images have been used. Traditionally, wave height estimation requires calibrations using external sensors. Recently, techniques have been rapidly evolving for calibration-free wave height estimation. These include tilt- [86] and shadowing-based algorithms [25], and an algorithm exploiting the joint PDF of dimensionless wave periods and wave heights [98]. Calibration-free wave height estimation is likely to be one of the continuing trends for wave measurements. Coherent X-band radar may be considered for such purposes since it provides the radial velocity of ocean surface waves that can be used to derive H_S [101]. In addition, a simple model for marine radar backscatter signals from the ocean surface has been developed [102], which may be further investigated for calibration-free wave height estimation. One of the remaining issues for wave measurement is that no effective algorithms have been developed for mitigating rain effects. With regard to this, S-band radar is a promising tool since, due to its longer wavelength, it can yield wave measurements under rain conditions [103]. Recently, models for SAR backscatter from the ocean surface under rainfall have been developed [104, 105]. X-band marine radar sea surface imaging mechanisms in rain events are also worth exploring.

Table 2.2 Inter-Comparison of the Reviewed Wave Measurement Techniques

Methods	Wave Spectrum Measurement	Wave Height Measurement	RMS Difference of H_S Measurement (m)	Calibration -Free	Images Required
Traditional 3D DFT	√	√	0.38	×	Multiple
Multilayer Perceptrons	√	√	0.22 - 0.27	×	Multiple
Iterative Least-Squares	√	×	-	×	Multiple
Quadratic Polynomial MTF	√	×	-	×	Multiple
Variable-Exponent Linear MTF	√	×	-	×	Multiple
Adaptive Recursive Positioning	√	×	-	×	Multiple
Geometrics-Based SNR Estimation	√	√	0.19	×	Multiple
2D Continuous Wavelet Transform	√	√	0.61	×	Single
Array Beamforming	√	√	0.12	×	Multiple
Illumination Probability	×	√	-	×	Single
Statistical Analysis	×	√	0.68 - 0.77	×	Single
Tilt-Based	×	√	0.35	√	Multiple
Original Shadowing-Based	×	√	-	√	Single
Water-Depth considerations	×	√	0.51	√	Single
Support Vector Regression	×	√	0.38 - 0.82	√	Single
Empirical Orthogonal Function-Principal Component	×	√	0.21	×	Multiple
Rotated Empirical Orthogonal Function	×	√	0.14 - 0.17	×	Multiple
Empirical Orthogonal Function-Joint PDF	×	√	0.51	√	Multiple

Chapter 3

Wind Direction Estimation From Low-Wind-Speed Rain-Contaminated Data

In 1998, Huang *et al.* [32, 33] proposed an empirical mode decomposition (EMD) method for adaptive time-frequency analysis of non-linear and non-stationary data. In that method, data could be decomposed into a finite number of narrow-banded intrinsic mode function (IMF) components. Since its appearance, the method has been widely used in various applications. In 2009, Wu *et al.* [34] proposed an ensemble EMD (EEMD), resolving the mode mixing problem of the original EMD, and resulting in a more practical method. In the same year, Wu *et al.* [35] proposed a multi-dimensional EEMD allowing the algorithm to be applicable in higher dimensions. In 2014, Wang *et al.* [106] analyzed the computational complexity of the EMD/EEMD and substantially reduced its execution time, leading to a computationally efficient method. In this chapter, two algorithms based on the EEMD technique are proposed to determine wind direction from low-wind-speed, rain-contaminated X-band marine radar data. The EEMD technique is introduced in Section 3.1. The 1D-EEMD-based and 2D-EEMD-based algorithms are described in Section 3.2 and Section 3.3, respectively. Experimental results obtained from ship-borne

radar and anemometer data are illustrated in Section 3.4. A summary for this chapter appears in Section 3.5.

3.1 EEMD

The EMD is the fundamental part of the Hilbert-Huang transform (HHT) for non-stationary and non-linear data analysis [32, 33]. It aims to adaptively decompose complicated data into a finite number of separate narrow-banded intrinsic mode function (IMF) components that admit well-behaved Hilbert transforms. An IMF is defined by two criteria: the numbers of zero crossings and extrema are equal or differ by one; the mean of the envelopes defined by local maxima and local minima is zero at any point. EMD is implemented by a sifting process [32,33] as described below.

For an arbitrary data set $X(t)$, the local extrema are first identified. Next, the local maxima and local minima are connected by cubic spline lines as the upper and lower envelopes, respectively. Then, the mean, m_{11}, of the upper and lower envelopes is subtracted from the original data, $X(t)$, to yield

$$h_{11} = X(t) - m_{11}, \tag{3.1}$$

such that if h_{11} meets the aforementioned criteria for an IMF, it is designated as the first IMF. Otherwise, h_{11} is regarded as new data, and the procedure is repeated until the result is an IMF. This process is described as

$$\begin{aligned} h_{12} &= h_{11} - m_{12} \\ &\vdots \\ h_{1i} &= h_{1(i-1)} - m_{1i} \end{aligned}, \tag{3.2}$$

where h_{1i} is the sifting result after i repetitions, and m_{1i} is the mean of the upper and lower envelopes of $h_{1(i-1)}$. When h_{1i} meets the criteria for an IMF, the procedure terminates,

and h_{1i} is designated as the first IMF, c_1, i.e.,

$$c_1 = h_{1i}. \tag{3.3}$$

Overall, c_1 consists of the highest-frequency components of the signal. After decomposing it from the original data $X(t)$, the first residual r_1 which can be expressed as

$$r_1 = X(t) - c_1 \tag{3.4}$$

is obtained. Generally, r_1 contains other components of the signal. Therefore, it is treated as new data, and the same sifting process as above is employed again to obtain the next IMF. The process, as indicated by

$$\begin{aligned} r_2 &= r_1 - c_2 \\ &\vdots \\ r_p &= r_{p-1} - c_p, \end{aligned} \tag{3.5}$$

where c_p is the pth IMF, and r_p is the pth residual, is repeated until no IMF can be extracted.

The original data can be reconstructed based on the IMFs and the pth residual as

$$X(t) = \sum_{q=1}^{p} c_q + r_p. \tag{3.6}$$

However, in some cases, intermittent oscillation of the signal may cause the problem of mode mixing, defined as various scales existing in a single IMF or a similar scale existing in different IMFs. In order to solve the mode mixing problem of EMD, EEMD was developed [34]. The basic steps, as found in [34], may be outlined as follows: i) add a finite-amplitude white noise signal to the original data; ii) apply EMD to the noise-added data; iii) repeat the previous two steps with different noise signals a sufficient

number of times (e.g., 100); iv) the set of the ensemble means of the corresponding IMF components of the decompositions is achieved as the final result. Here, both 1D-EEMD and 2D-EEMD are applied to marine radar images for wind direction determination.

3.2 1D-EEMD Based Algorithm

Suppose that one polar radar image with M rows and N columns is expressed as

$$I = \begin{pmatrix} i_{1,1} & i_{1,2} & \dots & i_{1,N} \\ i_{2,1} & i_{2,2} & \dots & i_{2,N} \\ \dots & \dots & \dots & \dots \\ i_{M,1} & i_{M,2} & \dots & i_{M,N} \end{pmatrix}, \tag{3.7}$$

where $i_{m,n}$ is the image intensity at the mth row and the nth column. For the 1D-EEMD-based algorithm, EEMD [34] is applied only to each column of I as indicated by

$$I(\sim, n) = \begin{pmatrix} i_{1,n} \\ i_{2,n} \\ \dots \\ i_{M,n} \end{pmatrix}. \tag{3.8}$$

This results in

$$I(\sim, n) = \sum_{j=1}^{J} G_j(\sim, n) = \sum_{j=1}^{J} \begin{pmatrix} g_{1,n,j} \\ g_{2,n,j} \\ \dots \\ g_{M,n,j} \end{pmatrix}, \tag{3.9}$$

where $g_{m,n,j}$ is the element of $G_j(\sim, n)$, $G_j(\sim, n)$ is the jth output IMF, with j ranging from 1 to J-1, J-1 being the number of IMFs, and $G_J(\sim, n)$ is the output residual. After all the columns are decomposed, the results can be rearranged into J matrices, in which

the jth matrix is

$$G_j = \begin{pmatrix} g_{1,1,j} & g_{1,2,j} & \cdots & g_{1,N,j} \\ g_{2,1,j} & g_{2,2,j} & \cdots & g_{2,N,j} \\ \cdots & \cdots & \cdots & \\ g_{M,1,j} & g_{M,2,j} & \cdots & g_{M,N,j} \end{pmatrix}. \tag{3.10}$$

The resultant J matrices consist of J-1 IMF components and one residual component of the 1D-EEMD of the radar image.

After the implementation of 1D-EEMD, the standard deviation σ_θ of one IMF component, or the combination of several IMF components, as a function of azimuth is least-squares curve fitted to a harmonic function as

$$\sigma_\theta = p_0 + p_1 \cos^2(0.5(\theta - p_2)). \tag{3.11}$$

Here, θ is the azimuth direction, and p_0, p_1, and p_2 are parameters determined by the curve fitting. Wind direction is determined as the azimuth direction corresponding to the peak of the fitted function.

3.3 2D-EEMD Based Algorithm

2D-EEMD [35] is an extension of the 1D-EEMD discussed above. After obtaining (3.10), EEMD [34] is again applied to each row of each matrix G_j as symbolized by

$$G_j(m,\sim) = \begin{pmatrix} g_{m,1,j} & g_{m,2,j} & \cdots & g_{m,N,j} \end{pmatrix}. \tag{3.12}$$

Its decomposition is

$$\begin{aligned} G_j(m,\sim) &= \sum_{k=1}^{K} H_{j,k}(m,\sim) \\ &= \sum_{k=1}^{K} \begin{pmatrix} h_{m,1,j,k} & h_{m,2,j,k} & \cdots & h_{m,N,j,k} \end{pmatrix} \end{aligned}, \tag{3.13}$$

where $h_{m,n,j,k}$ is an element of $H_{j,k}(m,\sim)$, $H_{j,k}(m,\sim)$ is the kth output IMF, with k ranging from 1 to K-1, K-1 being the number of IMFs, and $H_{j,K}(m,\sim)$ is the output residual. After all the rows in all matrices are decomposed, the results are rearranged as

$$H_{j,k} = \begin{pmatrix} h_{1,1,j,k} & h_{1,2,j,k} & \ldots & h_{1,N,j,k} \\ h_{2,1,j,k} & h_{2,2,j,k} & \ldots & h_{2,N,j,k} \\ \ldots & \ldots & \ldots & \ldots \\ h_{M,1,j,k} & h_{M,2,j,k} & \ldots & h_{M,N,j,k} \end{pmatrix}. \tag{3.14}$$

Finally, the radar image can be decomposed as

$$I = \sum_{j=1}^{J} \sum_{k=1}^{K} H_{j,k}. \tag{3.15}$$

Then, IMF components are obtained based on a comparable minimal scale combination principle [35], in which the components with comparable minimal scales are combined to give a single IMF component. This is expressed as

$$C_l = \sum_{j=l}^{J} H_{j,l} + \sum_{k=l+1}^{K} H_{l,k}, \tag{3.16}$$

where C_l is the lth IMF component of the 2D-EEMD of the radar image, with l ranging from 1 to the minimum of J-1 and K-1, and $C_{\min(J,K)}$ is the residual component of the 2D-EEMD of the radar image. This combination principle can result in IMFs revealing meaningful 2D features. Its visual schematic is illustrated in Table3.1, in which the subcomponents ($H_{j,k}$) in the neighboring cells with same shade are combined to obtain a single IMF.

Table 3.1 Visual Schematic of the Combination Principle.

$H_{1,l}$	$H_{1,2}$	...	...	$H_{1,K}$
$H_{2,l}$	$H_{2,2}$	...	...	$H_{2,K}$
...	...	...	...	...
$H_{J,l}$	$H_{J,2}$	...	...	$H_{J,K}$

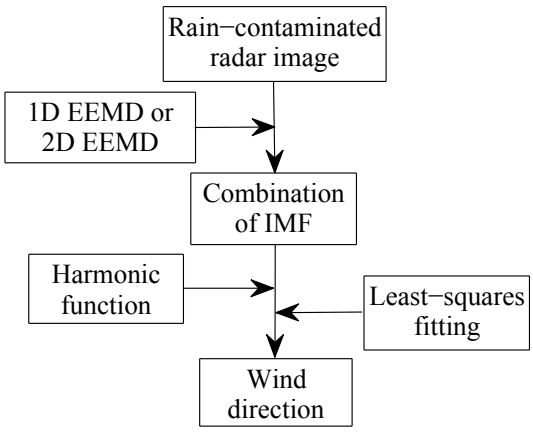

Fig. 3.1 Diagram for the proposed EEMD-based methods.

Next, in order to determine the wind direction, (3.11) is also used to least-squares fit the standard deviation σ_θ of one IMF component, or the combination of several IMF components, as a function of azimuth. An overall diagram for the proposed EEMD-based methods is shown in Fig.3.1.

3.4 Experimental Results

3.4.1 Data Overview

Data provided by Defence Research and Development Canada (DRDC) is employed to test the proposed methods. The radar and anemometer data were collected in a sea trial in late November of 2008, approximately 300 km south-southeast of Halifax, Nova Scotia, Canada. A standard Decca nautical radar operated at 9.41 GHz with horizontal polarization. The radar coverage was 360° in azimuth and from 240 m to 2160 m in range. The beam width of the radar was 2° and the range resolution was 7.5 m. The antenna was installed at a height of 21.9 m above sea level and rotated at a speed of about 28 rpm. The radar backscatter intensity was scaled to a level from 0 to 255, with 0 corresponding to the minimum backscatter and 255 to the maximum. Anemometers were mounted on the port and starboard sides of the ship. The average of the two anemometer

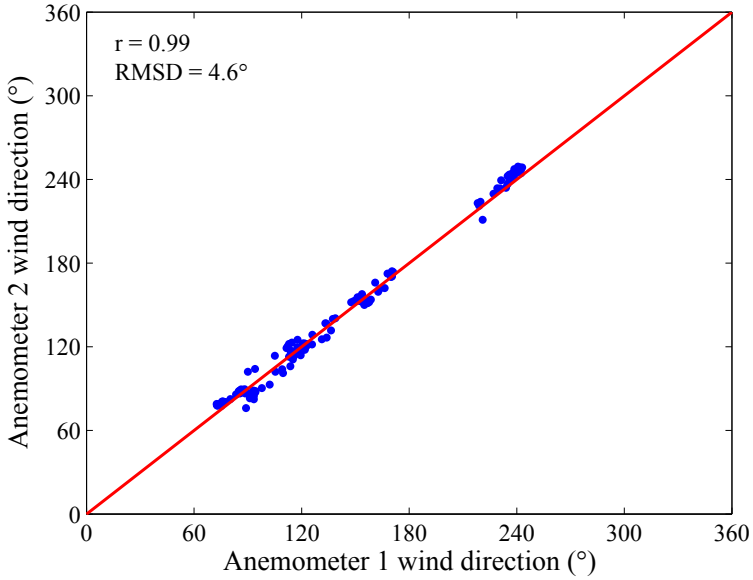

Fig. 3.2 Comparison of the measurements from two anemometers installed on the port and starboard sides of the ship.

measurements was used as the reference. It is reported in [1] that errors in anemometer measurements may be up to 10%. The reliability of the anemometer measurements in the work presented here can be evaluated by comparing the measurements from the two anemometers. These are shown in Fig.3.2. It is readily observed that the two anemometers produce similar wind direction measurements and the average may be legitimately used as the ground truth. Additionally, for the sake of completeness, the ship's path is shown in Fig.3.3.

3.4.2 Data Preprocessing

3.4.2.1 Noise Line Removal

One example of a rain-contaminated polar radar image collected at 01:48 on Nov. 27 (2008) is shown in Fig.3.4(a). It may be observed from the raw radar image in Fig.3.4(a) that radial noise lines due to interference of other marine radars are present as high-level intensity pixels aligned in the range direction. Some of these lines are highlighted by red circles. Since the noise lines may negatively affect wind direction retrieval, a method

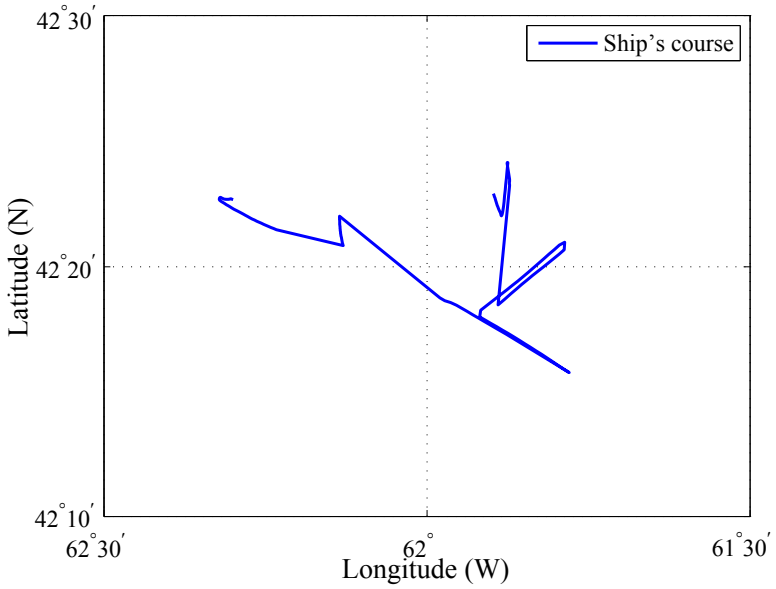

Fig. 3.3 Ship's path.

similar to that in [44] is used to remove them. First, a 3 × 3 kernel, in which the first and third columns are set as -1 and the second column is set as 2, is convolved with the raw polar radar image. Then, the noise lines are identified as the sets of at least 5 continuous pixels in the range direction with intensity levels greater than 255. Finally, each such pixel is replaced by the mean of its azimuthal-adjacent pixels. The result after this process, found in Fig.3.4(b), indicates that the noise lines have been successfully removed.

3.4.2.2 Image Classification

Only the data acquired in rain events under low wind speed is employed for the test. The image classification method described in [13] is used here for distinguishing the low-wind-speed, rain-contaminated data from the other data. The method is based on the statistical distribution of pixel intensities in each radar image. The parameters of zero-pixel percentage (ZPP) and high-pixel percentage (HPP) are used. ZPP is defined as the ratio of the number of pixels with intensity levels lower than 5 to the total number

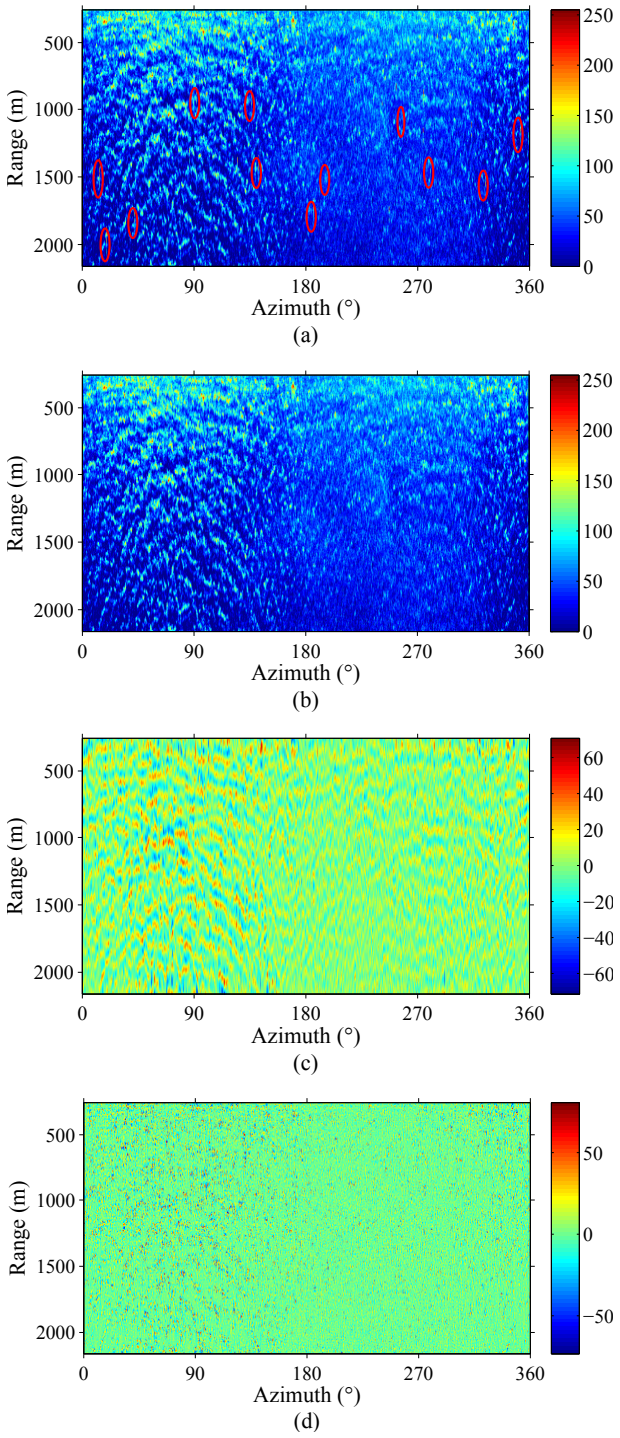

Fig. 3.4 (a) Low-wind speed, rain-contaminated raw polar radar image; (b) radar image in Fig.3.4(a) after noise line removal; (c) the third IMF component of the 1D-EEMD of the radar image in Fig.3.4(b); (d) the first IMF component of the 2D-EEMD of the radar image in Fig.3.4(b). The color scale represents gray level.

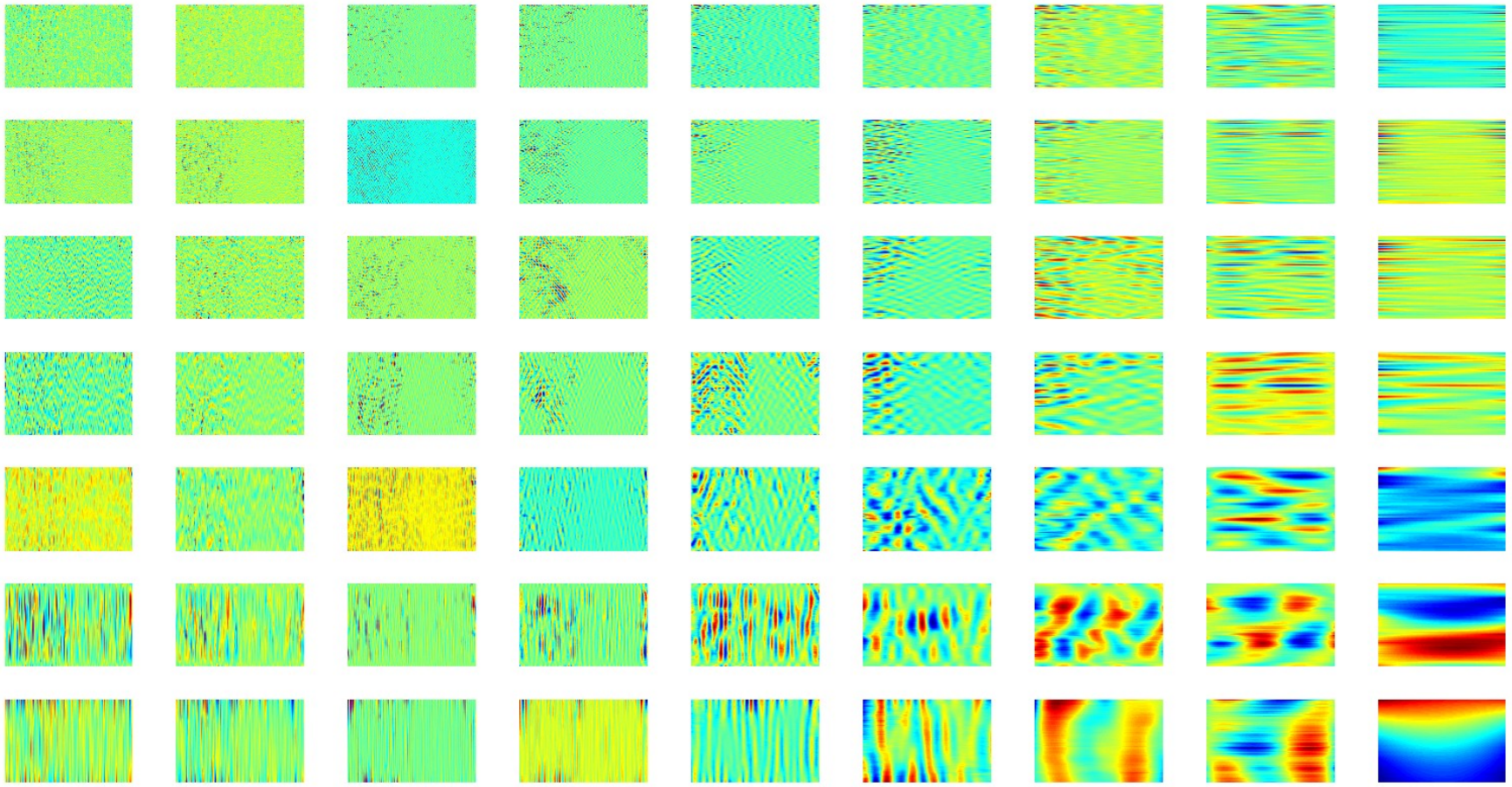

Fig. 3.5 Subcomponents of the 2D-EEMD of the radar image in Fig.3.4(b). The horizontal axis represents azimuth and the vertical axis represents range. The subcomponents in the same row have similar spatial scales in the vertical direction, and the subcomponents in the same column have similar spatial scales in the horizontal direction.

of pixels. HPP is defined as the ratio of the number of pixels with intensity levels higher than 100 to the total number of pixels. Low-wind-speed, rain-contaminated images are identified as those with ZPP lower than 10% and HPP lower than 15%.

3.4.3 Wind Direction Retrieval Results

The third IMF component (j=3) of the 1D-EEMD of the radar image in Fig.3.4(b) is depicted in Fig.3.4(c). The subcomponents of the 2D-EEMD of the radar image in Fig.3.4(b) appear in Fig.3.5. It may be observed from Fig.3.5that the subcomponents in the same row have similar spatial scales in the vertical direction and that the subcomponents in the same column have similar spatial scales in the horizontal direction. The first IMF component (l=1) of the 2D-EEMD of the radar image in Fig.3.4(b) is shown in Fig.3.4(d).

It may be discerned that the backscatter intensity in the radar image in Fig.3.4(b) is enhanced by rain and that the wave signature is partially obscured. Since rain affects the wave signature appearing in the radar images, the rain effect may be considered as a kind of modulation transfer function (MTF). On the contrary, it may be noted from both the IMF components in Fig.3.4(c) and Fig.3.4(d) that the image intensity enhancement due to rain is significantly removed and that the wind-induced, small-scale wave signature is well-preserved. Since the average of the intensity value of any IMF component is almost zero, which is one attribute of an IMF, the standard deviation, instead of the average of the intensity value for each azimuth, is used in the curve fitting process. The results for the 1D-EEMD-based method along with the third IMF component and the 2D-EEMD-based method using the first IMF component are depicted in Fig.3.6(a) and Fig.3.6(b), respectively, and the wind directions are determined as 75.5 $^\circ$ and 78.6°, respectively, which are very close to the anemometer measurement of 76.5°. As an inter-comparison, the curve fitting result obtained using the 1D-SA-based method in [18] is shown in Fig.3.6(c), and the wind direction is retrieved as 69.1 $^\circ$. The 1D-SA-based

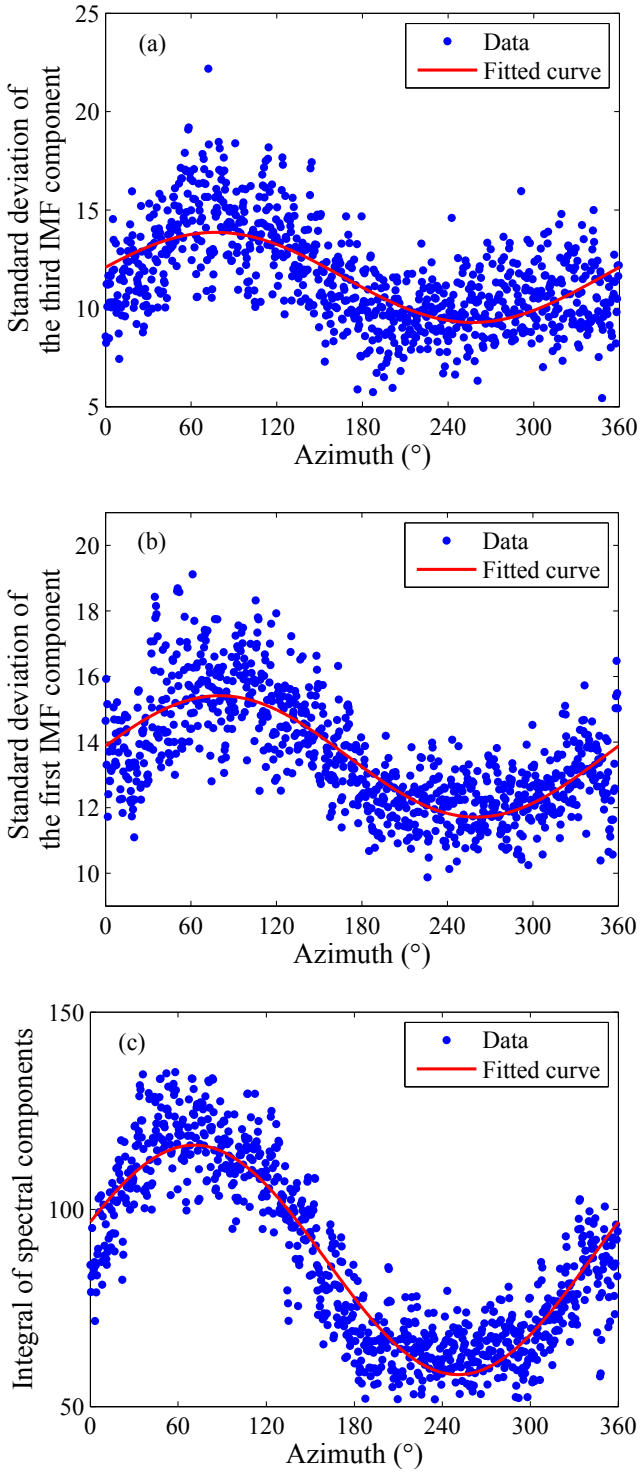

Fig. 3.6 Curve fitting results for (a) the 1D-EEMD based method by using the third IMF component; (b) the 2D-EEMD based method by using the first IMF component; (c) the 1D-SA based method.

Table 3.2 Overall Wind Direction Retrieval Results

Algorithm	IMF Components	r	RMSD
1D-SA based method	-	0.952	20.1°
1D-EEMD based method	1	0.986	13.7°
	2	0.980	16.8°
	3	0.984	12.7°
	1+2	0.982	15.7°
	1+2+3	0.986	14.1°
	1+2+3+4+5+6	0.982	14.9°
2D-EEMD based method	1	0.984	11.4°
	2	0.981	16.2°
	3	0.983	15.6°
	1+2	0.983	14.0°
	1+2+3	0.983	14.5°
	1+2+3+4+5+6	0.983	15.1°

method is used for the comparison because it was particularly proposed for wind direction extraction from rain-contaminated X-band radar images.

It should be noted that each radar image is decomposed into 6 IMF components and a residual for both 1D- and 2D-EEMD. Technically, the radar image can be decomposed into more than 6 IMF components, but it is not necessary because the magnitudes of additional IMF components are negligible compared to the first 6. Since the residual represents the overall trend of the radar image, it contains considerable rain contamination. Thus, excluding the residual can significantly mitigate the rain effects. Since the wind-induced, small-scale wave signature is preserved in IMF components with high oscillations (the first three IMF components), at least one of them should be included for the wind direction determination. The overall wind direction results derived from the EEMD-based algorithms by using different (combinations of) IMF components, as well as from the 1D-SA-based algorithm [18], are listed in Table3.2. It can be seen from Table3.2that while the EEMD-based algorithms generally deliver satisfactory wind direction retrieval results, the third IMF component generates the best result for the 1D-EEMD-based algorithm, and the first IMF component produces the best result for

the 2D-EEMD-based algorithm. Note that the combinations shown in Table3.2are only examples. Other combinations can also give good results if at least one of the first three IMF components is included and the residual is excluded.

The limitation of the EEMD-based methods is that they have high computational cost. As reported in [106], the EEMD of a data sequence has a computational complexity of $O(PQ)$, where P is the number of data points in the sequence and Q is the number of IMFs. In this work, EEMD should be implemented N times for the 1D-EEMD-based method since there are N columns in one radar image. Thus, the 1D-EEMD-based method has a computational complexity of $O(NMJ)$, where M is the number of pixels in each column and J is the number of IMFs after the application of EEMD to each column. For the 2D-EEMD-based method, an additional EEMD is applied to each row of each component (matrix G_j) resulting from 1D-EEMD. Thus, the 2D-EEMD-based method has a computational complexity of $O(NMJK)$, where K is the number of IMFs after the application of EEMD to each row. For the experimental platform used here, the computation time to produce one wind direction result from one image is around 10 s for 1D-EEMD and 100 s for 2D-EEMD. In this work, the antenna rotation period is 2.14 s (i.e. a speed of 28 rpm) and each radar image sequence of 32 images is collected approximately every two minutes. Within such a period, only one wind direction result can be obtained using the 2D-EEMD-based method. Thus, only one image from each image sequence is analyzed to estimate wind direction, i.e., one wind direction result will be obtained approximately every 2 minutes and 5 consecutive such results provide a single 10-minute average. A 10-minute moving window with an 80% overlap is used to determine the next average, and so on (that is, each 10-minute interval consists of the last 8 minutes from the previous window along with 2 minutes of new data, again providing a single new average of 5 results). Thus, after the first average is provided in the initial 10 minutes, average wind directions are updated every 2 minutes (i.e., near real-time in terms of practical ocean sensing). In order to compare the performance of three methods based on the same data, this process is maintained for the 1D-EEMD-based

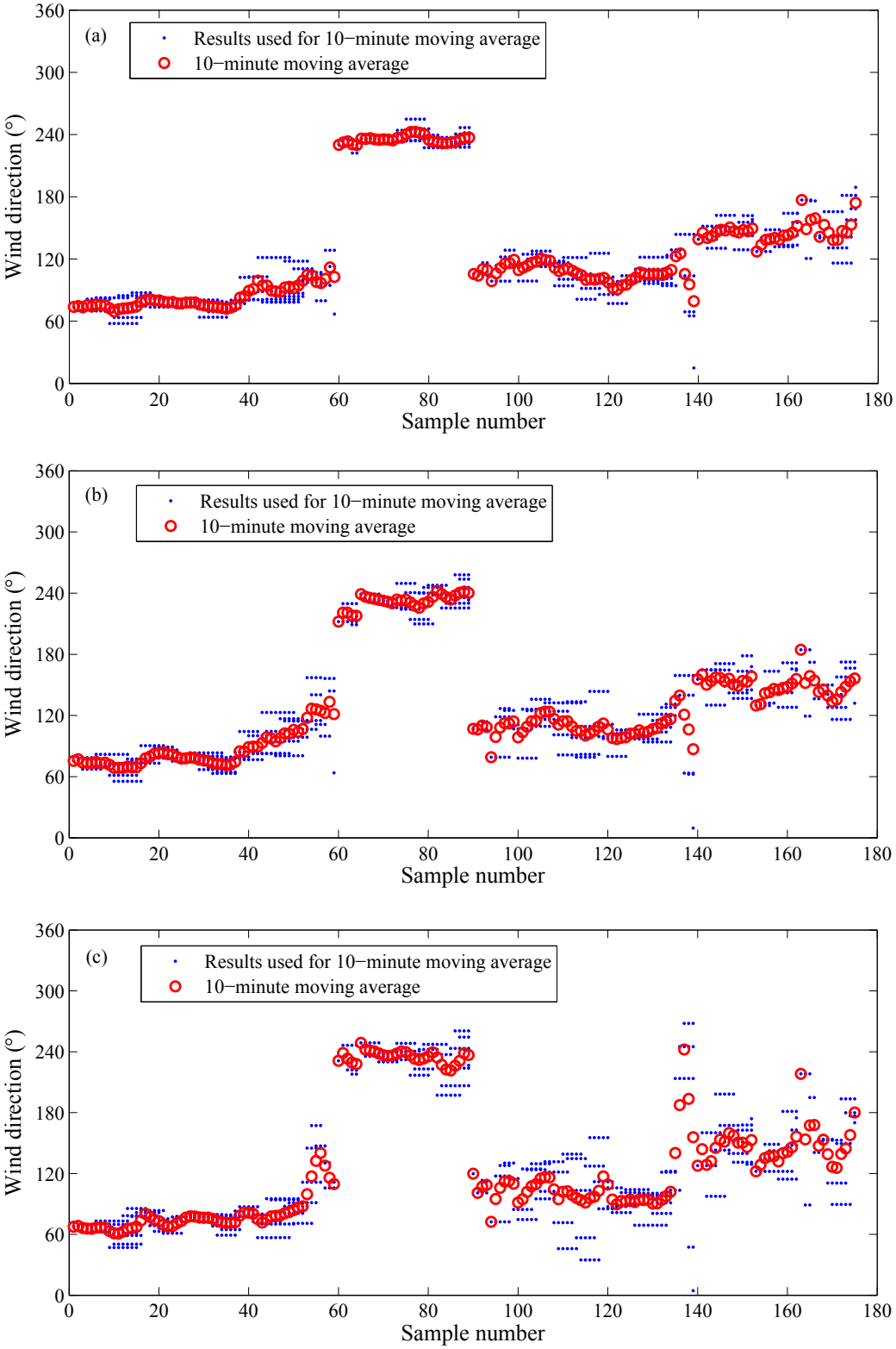

Fig. 3.7 Trend of wind direction retrieval results during each 10-minute interval used for the moving average for (a) 1D-EEMD based method; (b) 2D-EEMD based method; (c) 1D-SA based method.

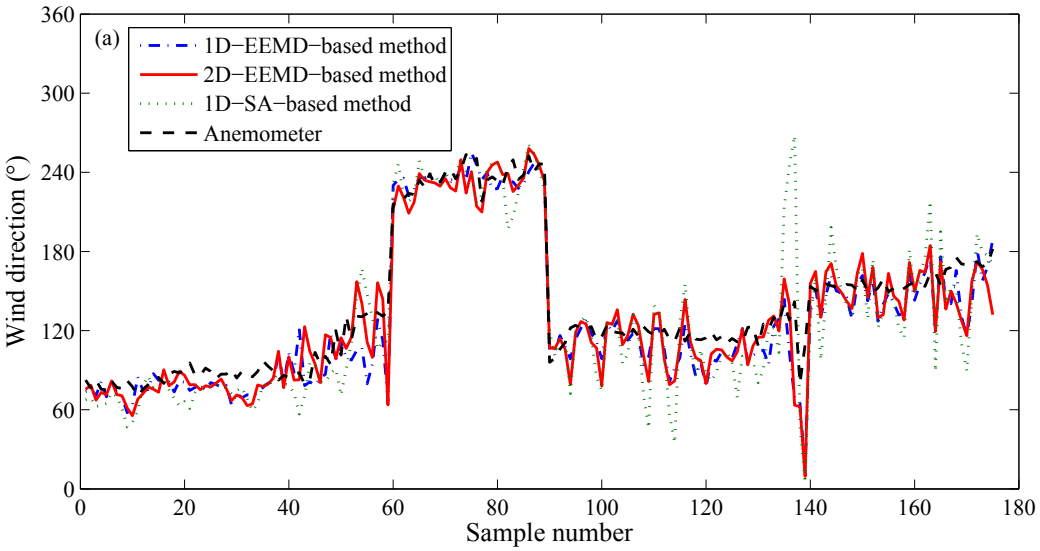
(a)
1D−EEMD−based method
2D−EEMD−based method
1D−SA−based method
Anemometer
Wind direction (°)
Sample number
0
60
120
180
240
300
360
0
20
40
60
80
100
120
140
160
180

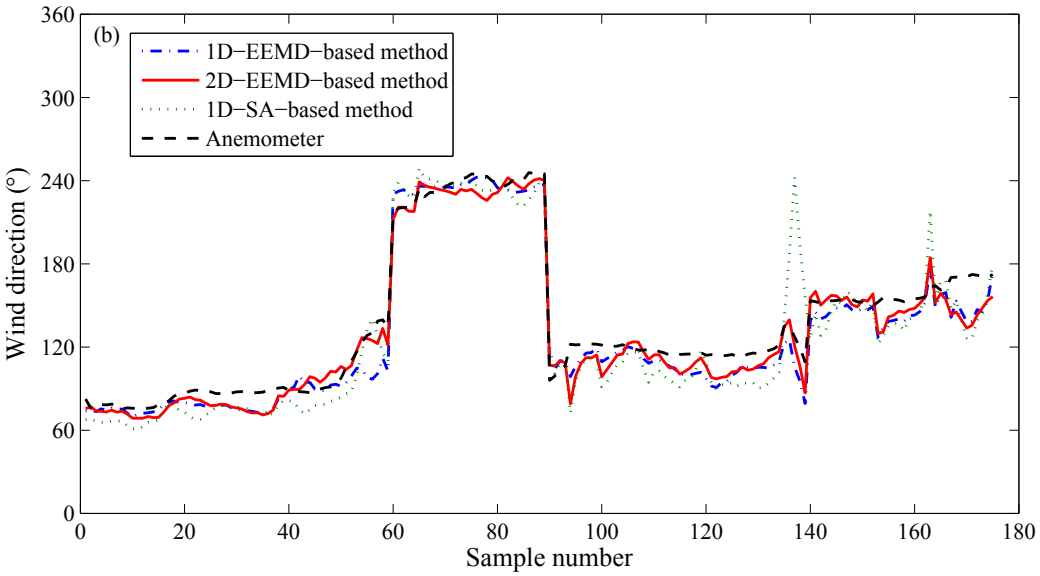
(b)
1D−EEMD−based method
2D−EEMD−based method
1D−SA−based method
Anemometer
Wind direction (°)
Sample number
0
60
120
180
240
300
360
0
20
40
60
80
100
120
140
160
180

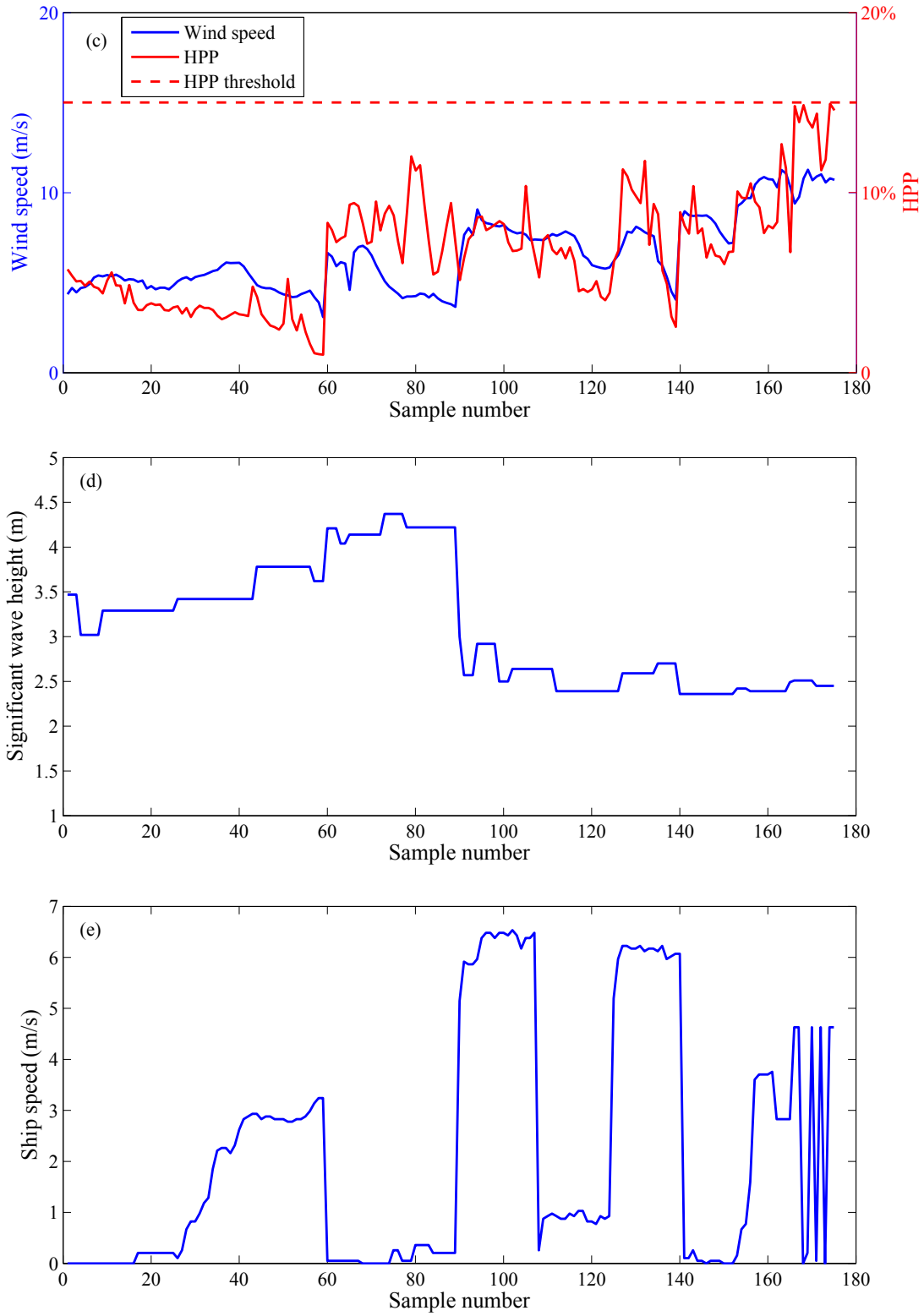

Fig. 3.8 (a) Comparison of time sequences of wind direction retrieval without a 10-minute moving average; (b) comparison of time sequences of wind direction retrieval with a 10-minute moving average; (c) wind speeds and HPPs; (d) significant wave heights; (e) ship speeds. The sampling rate is approximately 2 min.

and 1D-SA-based methods. The trend of wind direction retrieval results during each 10-minute interval used for the moving average is shown in Fig.3.7. Fig.3.8(a) shows the wind directions retrieved using the 1D-EEMD-based method with the third IMF component, the 2D-EEMD-based method with the first IMF component, and the 1D-SA-based method, with all being compared to the anemometer reference. Fig.3.8(b) displays the corresponding wind directions obtained by applying a 10-minute moving average to both anemometer and radar results. It can be seen from Fig.3.8(b) that the results derived from all three methods agree generally well with the reference. However, for some periods, the wind directions derived from the 1D-SA-based method show large deviations from the reference. These deviations are due to the fact that the image portion in the upwind direction is also contaminated by rain. In this case, however, the EEMD-based methods can still provide satisfactory results. Fig.3.8(c) depicts the wind speed and HPP values during the data acquisition period. It may be observed from that figure that the HPP threshold of 15% used for separating low-wind-speed and high-wind-speed cases corresponds to a wind speed of around 10 m/s. In addition, the significant wave heights and ship speeds during this period are shown in Fig.3.8(d) and Fig.3.8(e), respectively. The significant wave heights were measured by buoys approximately 10 km from the ship. The corresponding scatter plots of the retrieved wind directions using the three methods with the reference data in Fig.3.8(a) and Fig.3.8(b) are shown in Fig.3.9and Fig.3.10, respectively. From Fig.3.10, it can also be seen that while all three methods produce satisfactory results, the 1D-EEMD-based method and 2D-EEMD-based method outperform the 1D-SA-based method for rain-contaminated radar data collected under low wind speeds, with improvements of about 0.032 in the correlation coefficient, and about 7.4° and 8.7°, respectively, in the root-mean-square (RMS) difference.

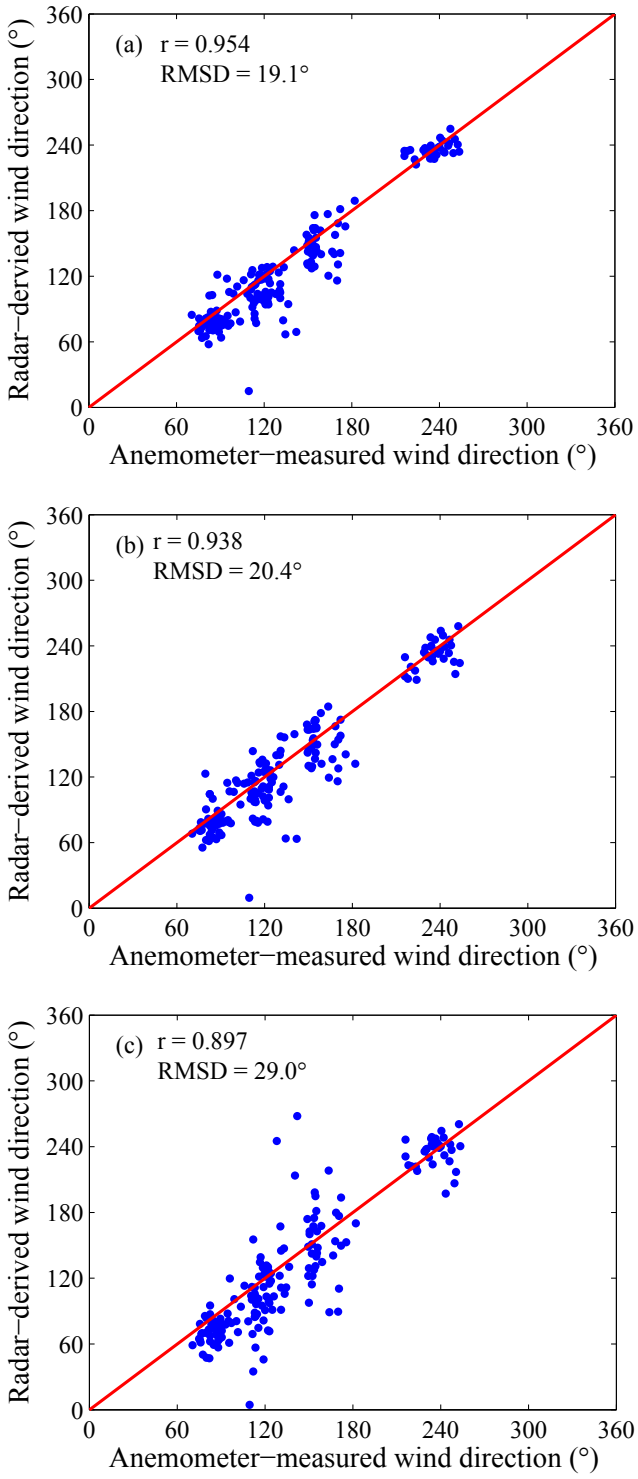

Fig. 3.9 Scatter plots of Fig.3.8(a): (a) the 1D-EEMD based method with the third IMF component; (b) the 2D-EEMD based method with the first IMF component; (c) the 1D-SA based method.

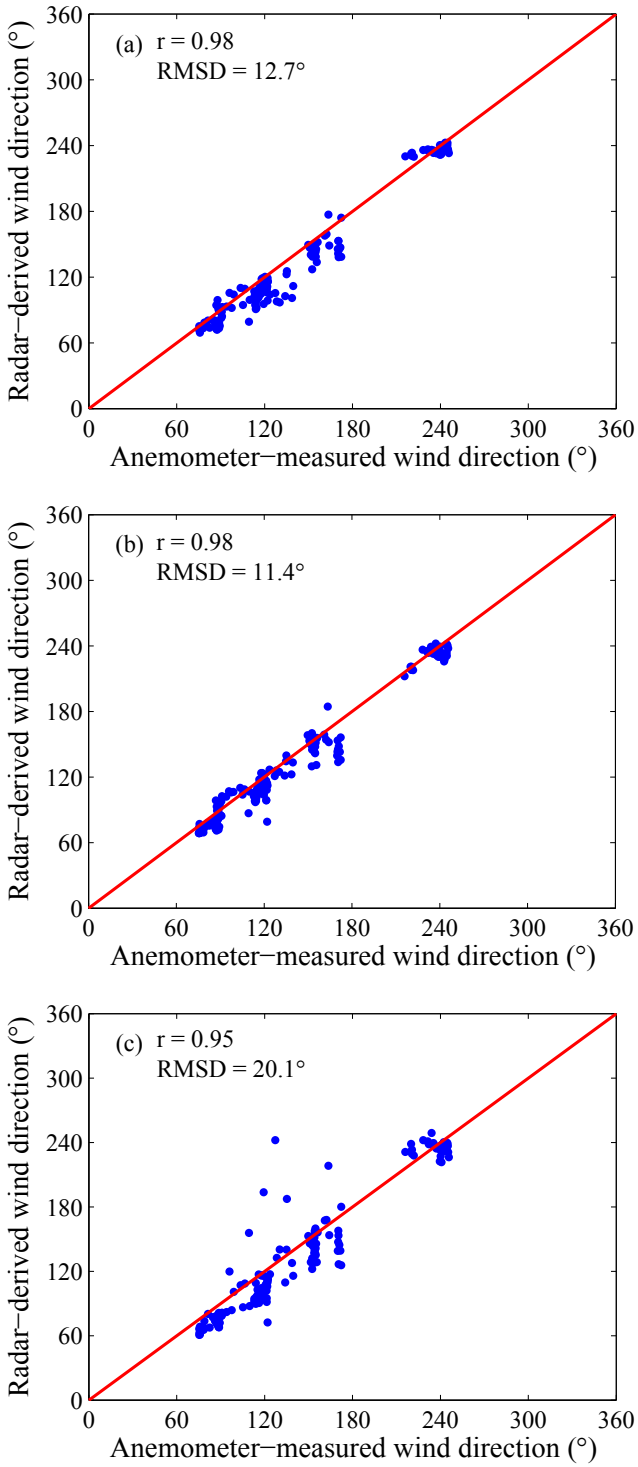

Fig. 3.10 Scatter plots of Fig.3.8(b): (a) the 1D-EEMD-based method with the third IMF component; (b) the 2D-EEMD-based method with the first IMF component; (c) the 1D-SA-based method.

3.5 Chapter Summary

In this chapter, two new schemes based on EEMD were proposed to retrieve wind direction from X-band nautical radar sea surface images contaminated by rain during periods of low wind speed. The standard deviation of an IMF component or the combination of several IMF components derived from 1D-EEMD or 2D-EEMD was used in the curve fitting process to determine wind direction. The basic criterion is that the combination should include at least one of the first three IMF components and exclude the residual. It was found that compared to the 1D spectral-analysis (SA) based method in [18], wind direction retrieval in rain events under low wind speed was significantly improved by the proposed EEMD-based methods. Based on the data used in this work, the third IMF component generates the best result for the 1D-EEMD based algorithm, but the first IMF component produces the best result for the 2D-EEMD based algorithm. While these wind direction results are encouraging, the computational costs for the EEMD-based algorithms are expensive. The experiments were conducted in Matlab R2013a installed on a personal computer (PC) running Windows 7 with a 3.0 GHz Intel Core i5-2320 central processing unit (CPU), an 8 GB memory, and a 64-bit operating system (OS). For the experimental platform in this work, the time consumed for the implementation of the traditional curve fitting method or 1D-SA based method is less than 1 s for one radar image. However, the execution times of the 1D-EEMD based and 2D-EEMD based algorithms are around 10 s and 100 s, respectively, for one radar image.

Chapter 4

Wind Direction and Speed Estimation From Rain-Free and Rain-Contaminated Data

The difference between this chapter and Chapter 3 is that only the wind direction is retrieved from low-wind-speed, rain-contaminated radar data using 1D-EEMD and 2D-EEMD techniques in the latter, while the EEMD, a normalization scheme, and a data control strategy are exploited in this chapter to estimate both wind direction and speed from both rain-free and rain-contaminated radar data. The EEMD and the normalization scheme are introduced in Section 4.1. The proposed algorithms for wind direction and speed estimation are described in Section 4.2 and Section 4.3, respectively. Section 4.4 illustrates the experimental results obtained from ship-borne radar and anemometer data. A summary for this chapter appears in Section 4.5.

4.1 EEMD and Normalization

According to the results in Section 3.2, the application of EEMD to the nth column of one polar radar image results in

$$I(\sim,n)=\sum_{j=1}^{J}G_j(\sim,n)=\sum_{j=1}^{J}\begin{pmatrix} g_{1,n,j} \\ g_{2,n,j} \\ \dots \\ g_{R,n,j} \end{pmatrix}, \tag{4.1}$$

where $G_j(\sim,n)$ is the jth output IMF, with j ranging from 1 to J-1, J-1 being the number of IMFs, and $G_J(\sim,n)$ the output residual. The EEMD result for $I(\sim,1)$ in one radar image is shown in Fig.4.1. It can be seen from Fig.4.1that, due to the nature of the EEMD, the intrinsic oscillatory scale increases from the first to the last IMF and the residual shows the overall trend of the original data. In terms of the radar image, the first IMF represents the wind-induced small-scale wave signature and the residual is related to the overall image intensities that depend on the wind strength. Moreover, in the presence of rain, the overall image intensities are enhanced whereas the wind-induced small-scale wave signature is weakened. Therefore, in order to apply the technique in both rain and rain-free cases, only the first IMF and the residual are used for wind measurements.

Implicitly, the mean of an IMF is almost zero, and therefore both positive and negative values exist in such functions. Thus, a normalization scheme [36] should be applied to the first IMF, $G_1(\sim,n)$, to obtain its amplitude modulation (AM) part. First, all the local maxima of the absolute values of $G_1(\sim,n)$ (i.e., $|G_1(\sim,n)|$) are identified. Then, all these maxima are connected with a cubic spline curve, resulting in the envelope of $G_1(\sim,n)$ and designated as $e_1(\sim,n)$. The first normalization result $f_1(\sim,n)$ is given as

$$f_1=\frac{G_1(\sim,n)}{e_1(\sim,n)}. \tag{4.2}$$

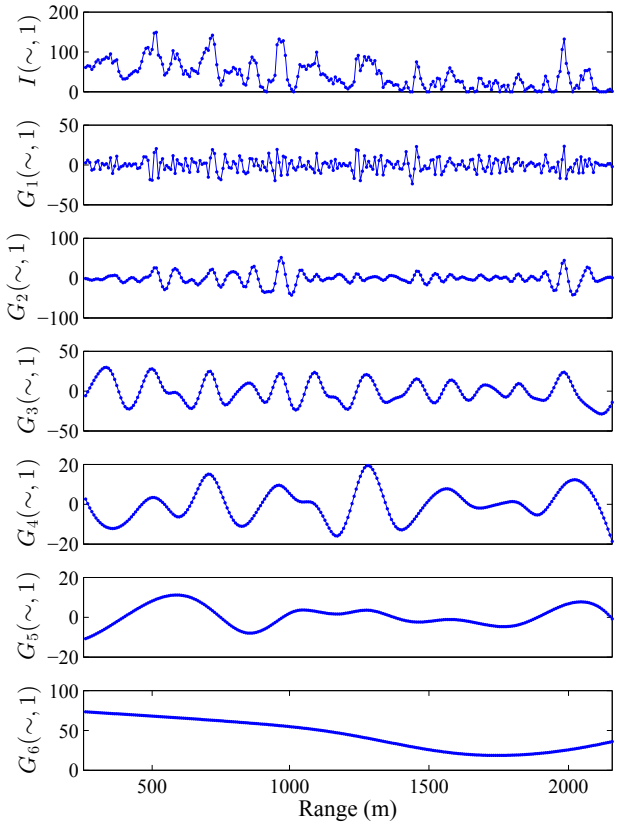

Fig. 4.1 EEMD result for $I(\sim,1)$ in one radar image obtained at 23:43 on Nov. 26, 2008. The vertical axis represents gray level.

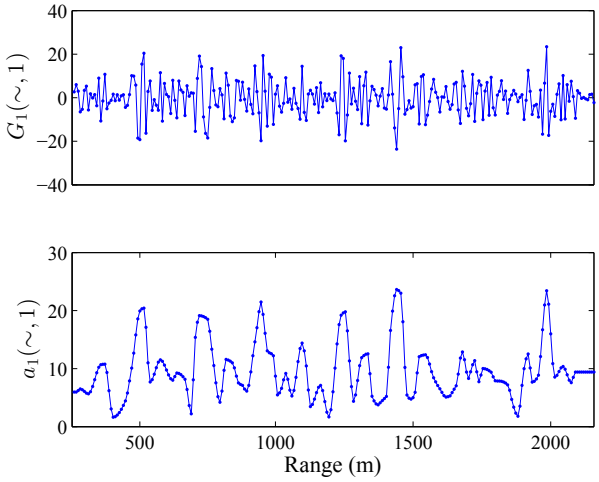

Fig. 4.2 $G_1(\sim,1)$ in Fig.4.1and its AM part $a_1(\sim,1)$. The vertical axis represents gray level.

If all the absolute values of $f_1(\sim,n)$ are equal to or less than 1, $e_1(\sim,n)$ is the AM part and $f_1(\sim,n)$ is the frequency modulation (FM) part of $G_1(\sim,n)$, and the normalization process ends. Otherwise, this normalization process is repeated as

$$\begin{aligned} f_2(\sim,n) &= \tfrac{f_1(\sim,n)}{e_2(\sim,n)} \\ &\vdots \\ f_i(\sim,n) &= \tfrac{f_{i-1}(\sim,n)}{e_i(\sim,n)}, \end{aligned} \tag{4.3}$$

where $e_i(\sim,n)$ is the envelope of $f_{i-1}(\sim,n)$. The process stops when all the absolute values of $f_i(\sim,n)$ are equal to or less than 1. Then, $f_i(\sim,n)$ is the FM part of $G_1(\sim,n)$, and the AM part of $G_1(\sim,n)$ is calculated as

$$a_1(\sim,n) = \frac{G_1(\sim,n)}{f_i(\sim,n)} = e_1(\sim,n)e_2(\sim,n)\cdots e_i(\sim,n). \tag{4.4}$$

$G_1(\sim,1)$ of Fig.4.1and its AM part $a_1(\sim,1)$ are shown in Fig.4.2.

4.2 Wind Direction Retrieval

In the absence of rain, the normalized RCS (NRCS) of an HH-polarized X-band radar operating at grazing incidence exhibits a peak in the upwind direction [15]. If the radar backscatter is contaminated by rain, the NRCS will be affected. However, it is found in [18] that when the wind speed is high, the dependence of the NRCS on wind direction is not significantly affected by rain because the wind effect dominates. Therefore, in rain-free and high-wind-speed rain cases, the residual, which is related to the overall image intensities that depend on the NRCS, may be used to estimate wind direction. The average of the residual, R_n, in each azimuth direction is calculated as

$$R_n = \frac{1}{M}\sum_{m=1}^{M} G_J(m,n), \tag{4.5}$$

where M is the total number of image pixels in each azimuth direction. Then, R_n, rather than the average radar backscatter intensity [15], is least-squares curve fitted to a harmonic function as

$$R_n = p_0 + p_1 \cos^2\left(0.5\left(\frac{2\pi(n-1)}{N} - p_2\right)\right), \tag{4.6}$$

where N is the total number of azimuth directions in one radar image, and p_0, p_1, and p_2 are parameters determined by the curve fitting. Wind direction is determined as the azimuth direction corresponding to the peak of the fitted function.

In low-wind-speed rain cases, the first IMF is used to estimate wind direction since it preserves the wind-induced small-scale wave signature that shows an immediate reaction to wind effects. The average, $A_{1,n}$, of the AM part of the first IMF in each azimuth direction is calculated as

$$A_{1,n} = \frac{1}{M}\sum_{m=1}^{M} a_1(m,n). \tag{4.7}$$

Then, similar as in (4.6), $A_{1,n}$ is least-squares curve fitted to the harmonic function as

$$A_{1,n} = p_0 + p_1 \cos^2\left(0.5\left(\frac{2\pi(n-1)}{N} - p_2\right)\right), \tag{4.8}$$

from which the wind direction can be determined.

4.3 Wind Speed Retrieval

The AM part of the first IMF and the residual are both involved in the training model for both rain and rain-free cases. To compare these two quantities, the average, m_a, of the AM part of the first IMF in one radar image is calculated as

$$m_a = \frac{1}{N}\sum_{n=1}^{N} A_{1,n}. \tag{4.9}$$

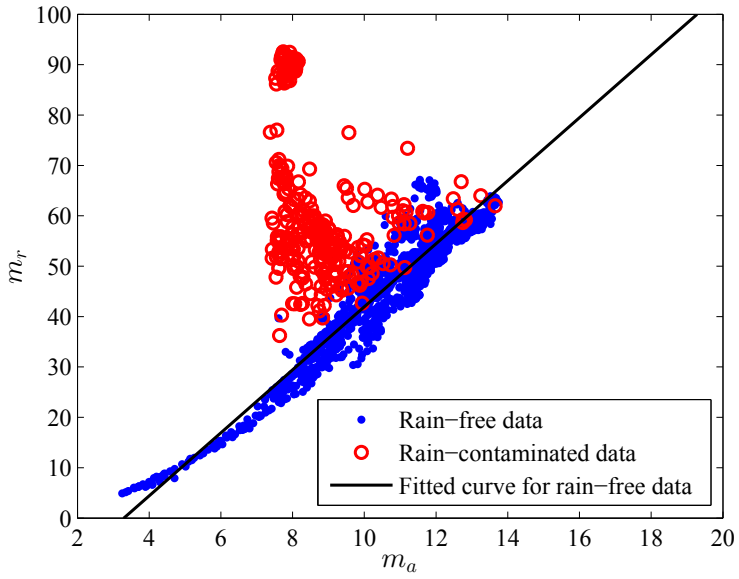

Fig. 4.3 Relationship between m_a and m_r for both rain-free and rain-contaminated data. Fitted curve for rain-free data: m_r=6.255*m_a-20.58

Similarly, the average, m_r, of the residual in one radar image is calculated as

$$m_r = \frac{1}{N}\sum_{n=1}^{N} R_n. \tag{4.10}$$

The relationship between m_a and m_r for both rain and rain-free cases is shown in Fig.4.3. It can be seen that the relationship is almost linear for rain-free cases. However, in rain cases, m_r increases whereas m_a decreases. Since the slope of the fitted curve for the relationship in rain-free cases is close to 6, the weight for m_a is set as 6 in the combination M_{com}, which is expressed as

$$M_{com} = 6m_a + m_r. \tag{4.11}$$

Adding a weight to m_a in the combination is due to the fact that the increases of m_r are generally larger than the decreases of m_a in rain cases. The weight of 6 results in almost equivalent effects of these two quantities on the combination, in which the increase of m_r can almost be compensated for by the decrease of m_a after being scaled by the weight. Then, a logarithmic relationship between M_{com} and wind speed w is sought through

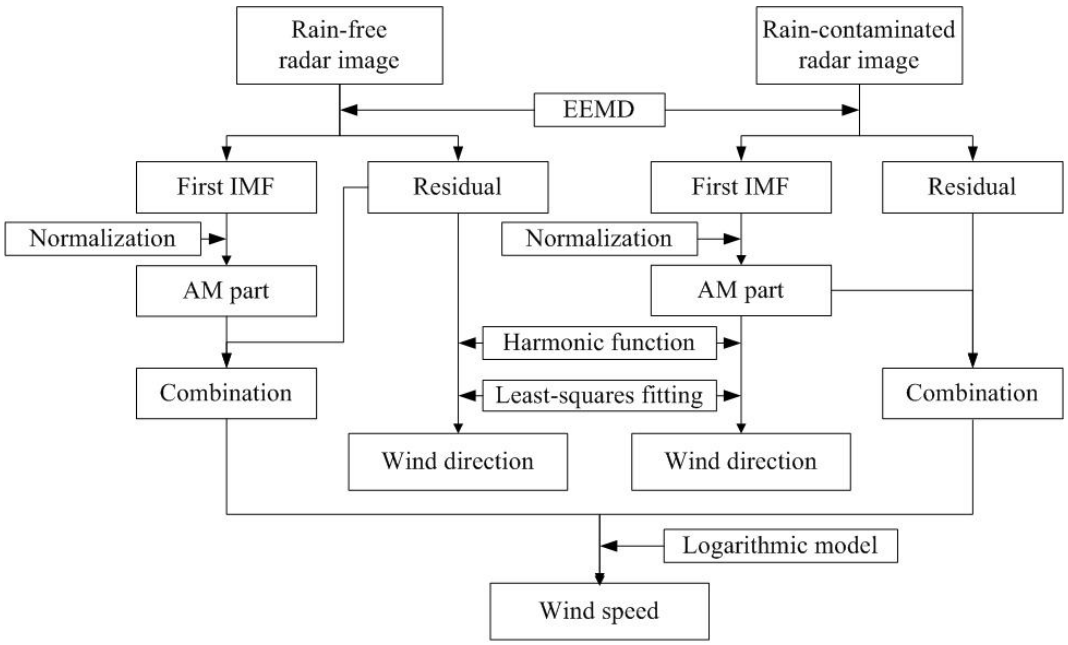

Fig. 4.4 Basic steps of the EEMD-normalization-based algorithm.

curve-fitting. The relationship using anemometer wind speed data is written as

$$M_{com} = p_0 + p_1 \cdot \ln(w_{Spd} + p_2), \tag{4.12}$$

where p_0, p_1 and p_2 are parameters determined from the curve-fitting process. After the parameters are determined, based on (4.12), wind speed can be estimated from M_{com} for any radar data. Fig.4.4illustrates the basic steps of the EEMD-normalization-based algorithm for wind parameter estimation.

4.4 Experimental Results

4.4.1 Data Overview

The proposed method is tested using radar and anemometer data described in Section 3.4.1. The data were collected approximately 300 km south-southeast of Halifax, Nova Scotia, Canada during a sea trial from Nov. 26 to Dec. 4 of 2008. During the sea trial, the wind speed ranged from 2 m/s to 16 m/s, and the significant wave height varied

Table 4.1 Radar Information

	Decca	Furuno
Polarization	Horizontal	Horizontal
Operating frequency	9.41 GHz	9.41 GHz
Range resolution	7.5 m	7.5 m
Range coverage	240 m - 2160 m	240 m - 2160 m
Beam width	2°	1.9°
Azimuth coverage	360°	Around 300°
Antenna rotation speed	28 rpm	40 rpm
Antenna height	21.9 m	16.5 m
Backscatter intensity level	0 - 255	0 - 255

correspondingly between 1.5 m and 5 m. This permitted the methods to be evaluated under typical wind conditions. The parameters for the two radars (Decca and Furuno) utilized in the experiment are listed in Table4.1. As in Section 3.4.1, the two anemometer measurements that were collected on the port and starboard sides, respectively, were averaged as the reference.

4.4.2 Data Control Strategy

A strategy is proposed to distinguish rain-free and rain-contaminated data. For one radar image, if all the pixel intensities in one azimuth direction are higher than 1, the direction is defined as a high-clutter direction (HCD). Then, if the high-clutter direction percentage (HCDP, defined as the number of HCDs divided by the total number of directions in one image) is higher than 5%, the image is recognized as a rain-contaminated image. Moreover, high-pixel percentage (HPP) [18] is used to distinguish low-wind-speed cases and high-wind-speed cases. HPP is defined as the number of pixels with intensities higher than 100 divided by the total number of pixels in one radar image. If the HPP of one image is larger than 30%, it is recognized as a high-wind-speed image. Otherwise, it is recognized as a low-wind-speed image.

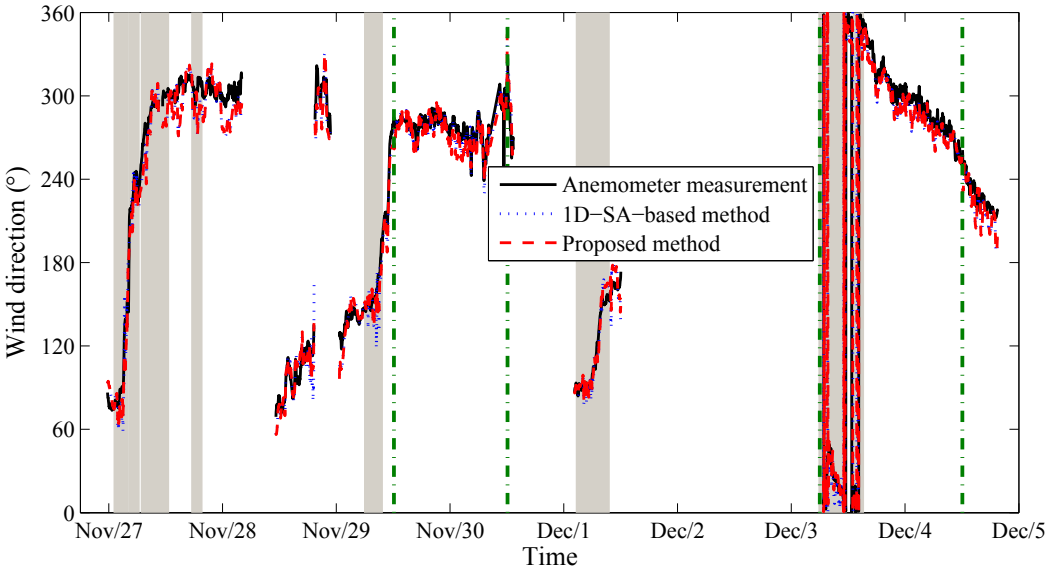

Fig. 4.5 Comparison of the sequences of wind direction results. The results from rain-contaminated data are indicated by the gray shadow.

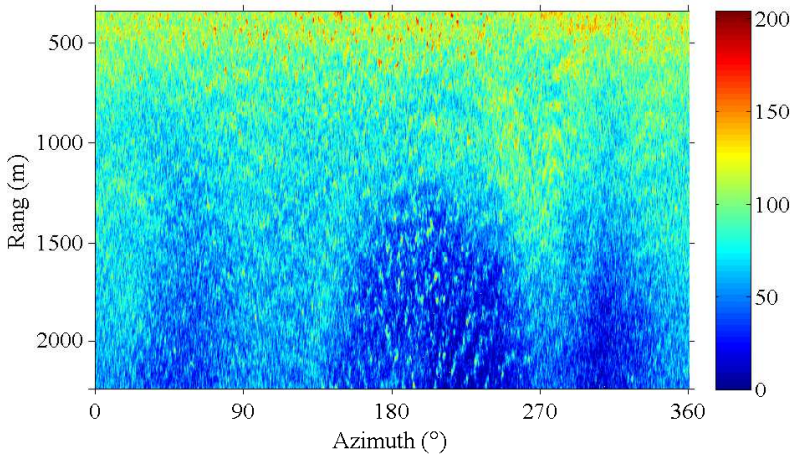

Fig. 4.6 Rain-contaminated radar image collected at 8:32, Nov. 29. Anemometer-measured wind direction is 160.5°.

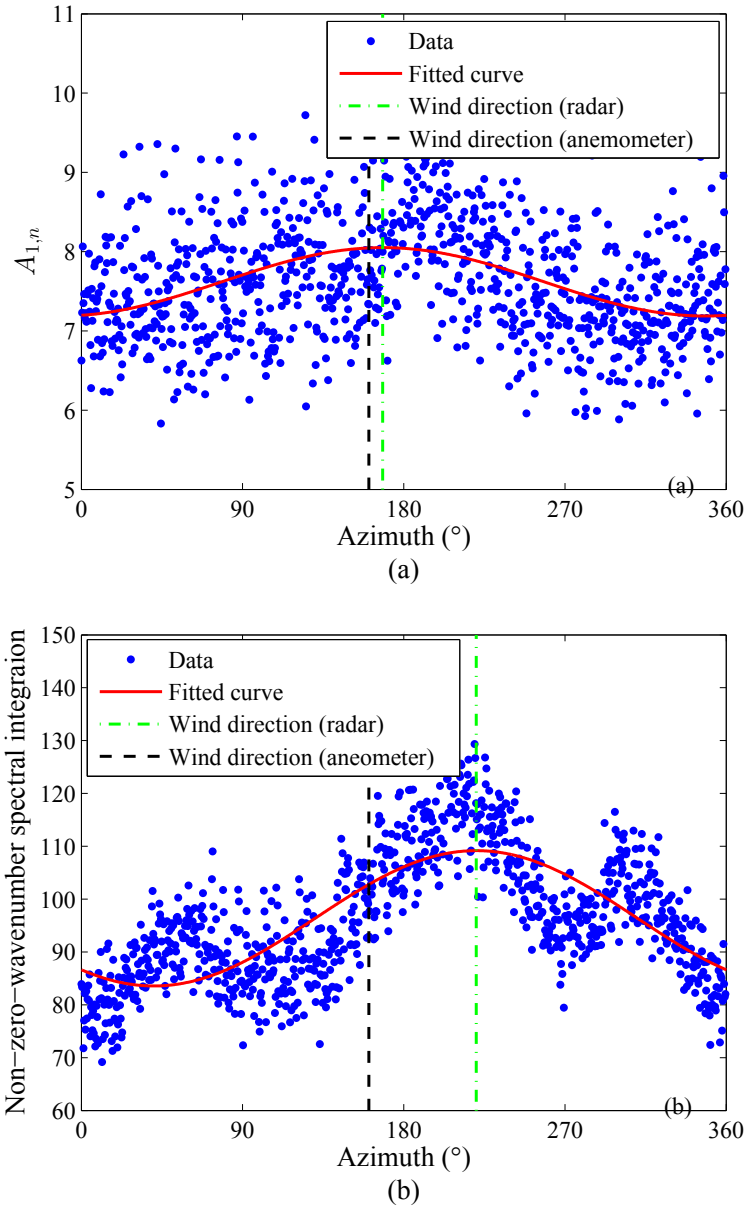

Fig. 4.7 Curve fitting results of Fig.4.6: (a) proposed method; (b) 1D-SA based method.

4.4.3 Wind Direction Results

The wind direction results obtained using the 1D spectral-analysis (SA)-based method [18] and the proposed method are compared with the anemometer measurements in Fig.4.5. Both the anemometer and radar results are moving-averaged over 10 minutes. It can be observed that both methods generally produce good results. However, the results derived from the 1D-SA-based method show large deviations from the reference for some periods with rain. These deviations are due to the fact that the image portion in the upwind direction is also contaminated by rain. In the 1D-SA-based method, the harmonic function is curve fitted to the spectral integration over the wavenumber range of [0.01, 0.2] since this yields satisfactory results [18]. However, the value of this integration is larger in the directions where the radar backscatter is less contaminated by rain. Thus, if the upwind direction is also contaminated by rain, the method will not produce accurate results. However, in the proposed method, only the first IMF is used because it corresponds to the short-scale waves that react to wind quickly and produces the best results. An example is shown in Fig.4.6and Fig.4.7. It can be seen in Fig.4.6that rain contaminates almost the whole image including the upwind direction, which is measured as 160.5° by anemometer. It may be noted that the curve fitting result of the 1D-SA-based method in Fig.4.7(b) shows peaks in directions where the radar backscatter is less contaminated by rain, and the wind direction is estimated as 220.5°. However, in the curve fitting result of the proposed method in Fig.4.7(a), although the data is relatively scattered from the fitted curve, the wind direction is estimated as 168.3°, which is close to the anemometer measurement. It should be noted that due to the high variance of the fitting in Fig.4.7(a), the method needs to be further refined to better identify the wind-induced wave signature from such heavily rain-contaminated data. The basic mechanism for wind direction retrieval is similar to that in [15], which is based on the fact that only one backscatter intensity peak exists in the upwind direction of an image collected with an HH-polarized X-band radar operating at grazing incidence [13]. For synthetic aperture radar (SAR)

or an altimeter operating at nearly-vertical incidence, ripples, whitecaps, and floating foam induced by local winds decrease the local surface reflectivity [107, 108]. However, X-band marine radar backscatter mainly results from the wind-induced ripples and foam. The intensity increases with wind speed and shows one peak in the upwind direction.

The scatter plots of the radar results and anemometer measurements for the proposed method and the 1D-SA-based method are shown in Fig.4.8. The root-mean-square (RMS) differences with respect to the reference for the proposed method and the 1D-SA-based method are 11.5° and 12.3°, respectively, for all the data. Furthermore, for the rain-free data, the RMS differences for both methods are 11.2°. For the rain-contaminated data, the RMS differences for the proposed method and the 1D-SA-based method are 12.9° and 17.8°, respectively. It is found that while these two methods produce almost the same wind direction results in rain-free cases, a significant improvement in rain cases is obtained by the proposed method.

4.4.4 Wind Speed Results

The training data for the proposed method and the 1D-SA based method in [19] are shown in Fig.4.9and Fig.4.10, respectively, for the Decca and Furuno radars. For comparison purposes, the training data for the Decca radar are the same as those in [19], i.e., they are taken from 12:00 to 23:00 on Nov. 27 and from 00:30 to 07:00 on Nov. 29. The training data for the Furuno radar are taken from 12:12, Nov. 29 to 12:04, Nov. 30. The remaining data are used for validation. It can be seen that while fitting results for the two methods are similar in Fig.4.10, the fitting result of the proposed method is better than that of the 1D-SA-based method in Fig.4.9. In addition, for high wind speeds (larger than around 10 m/s), M_{com} in Fig.4.9(a) is stable, but the spectral integrations in Fig.4.9(b) deviate from the fitted curve, leading to less reliable wind speed results. This is because when the wind speed is high, the spectral integration is not the same for rain-free and rain-contaminated data with similar wind speeds. An

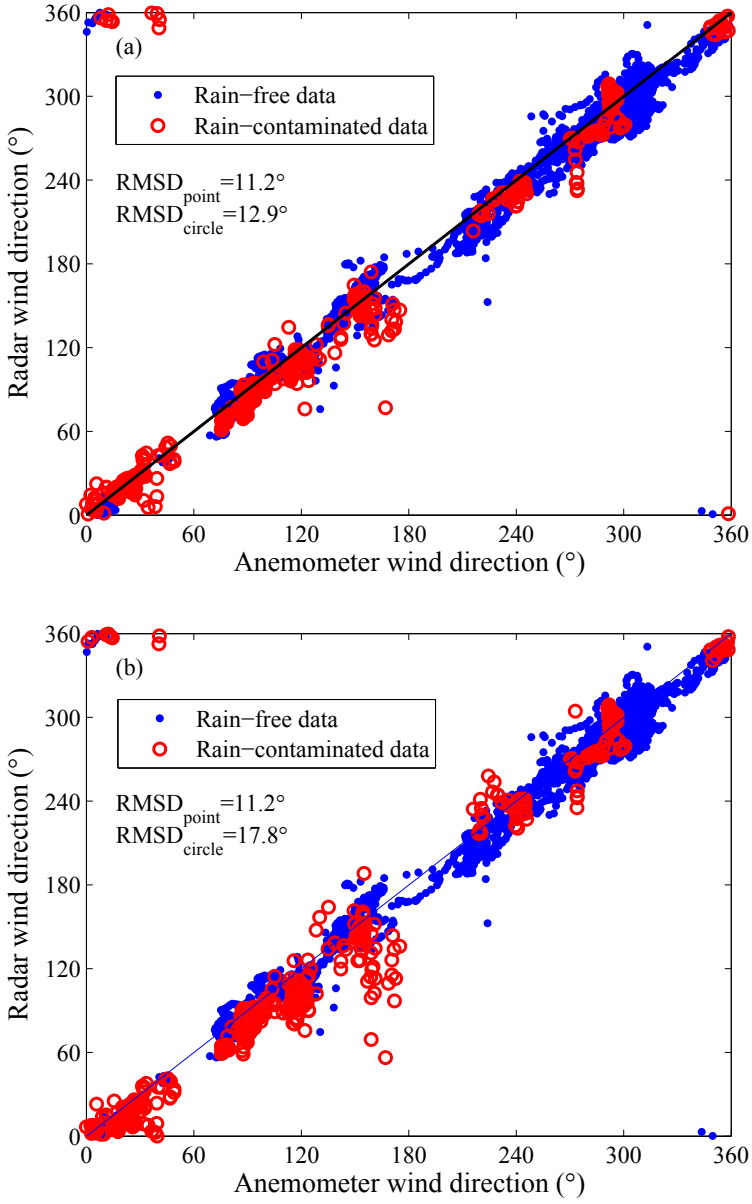

Fig. 4.8 Scatter plots of wind direction results: (a) proposed method; (b) 1D-SA based method.

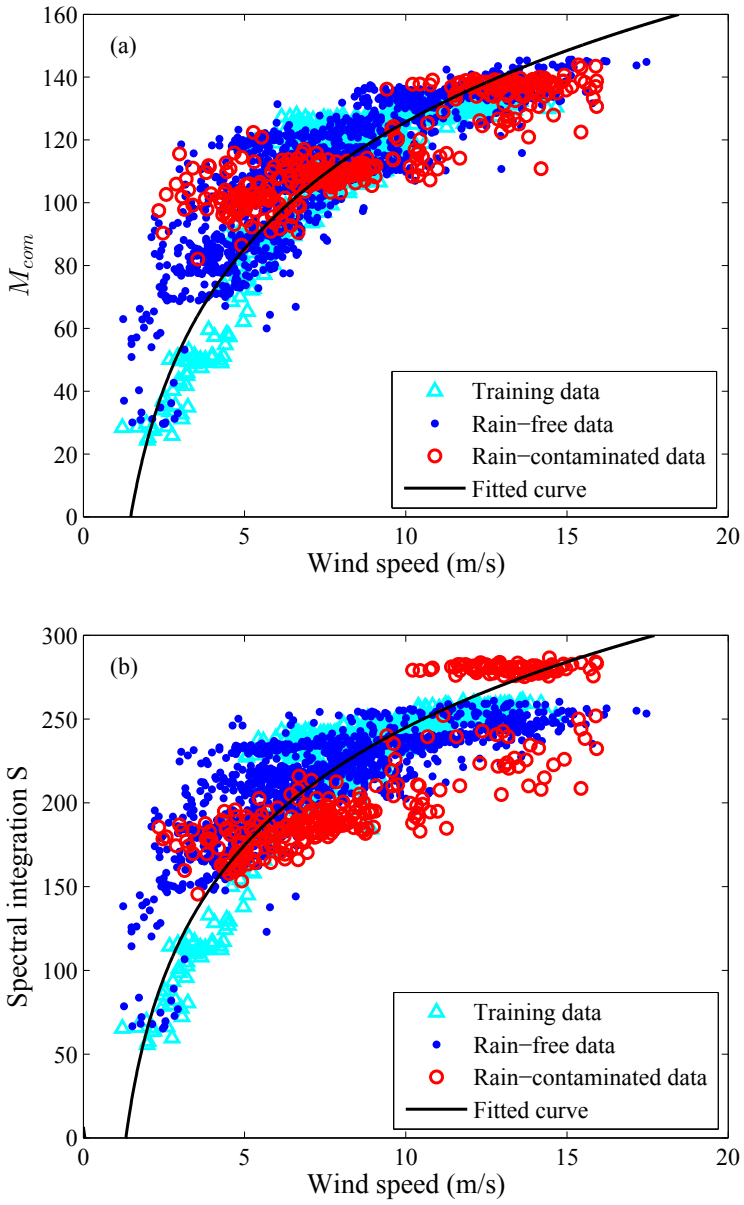

Fig. 4.9 Training processes for the Decca data. (a) Proposed method; fitted curve for training data: M_{com}=5.84+53.43ln(w-0.5708). (b) 1D-SA based method; fitted curve for training data: S=41.28+91.25ln(w-0.6839).

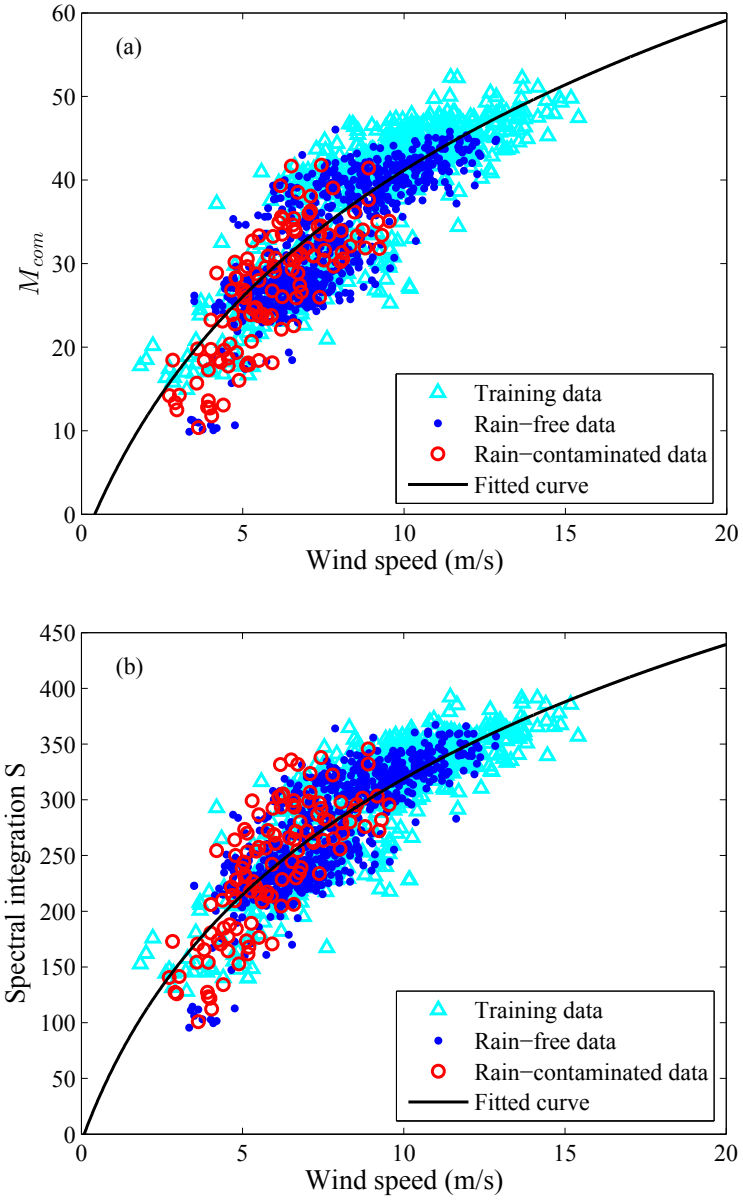

Fig. 4.10 Training processes for the Furuno data. (a) Proposed method; fitted curve for training data: M_{com}=-41.1+31.87ln(w+3.219). (b) 1D-SA based method; fitted curve for training data: S=-202.2+205.8ln(w+2.585).

example is shown from Fig.4.11to Fig.4.13. Fig.4.11(a) and Fig.4.11(b) show rain-contaminated and rain-free radar images, respectively, both of which are collected under similar high wind speeds. Their wavenumber spectra averaged over azimuths derived as in [19] are shown in Fig.4.12. It can be seen that since wind dominates in both cases, the non-zero-wavenumber spectral integrations are similar for them. However, the zero-wavenumber spectral strength for rain-contaminated data is higher than for rain-free data. Thus, although the wind speeds are similar, their spectral integrations are not the same, resulting in the scatter for high wind speeds seen in Fig.4.9(b). Fig.4.13 shows $a_1(\sim,n)$ and $G_J(\sim,n)$ averaged over azimuths for the images in Fig.4.11. It may be observed from the average $a_1(\sim,n)$ and $G_J(\sim,n)$ in Fig.4.13that m_a is larger for rain-free data and m_r is larger for rain-contaminated data. Moreover, after being scaled by the weight of 6, the change of m_a can be compensated for by the change of m_r, resulting in similar M_{com} for rain-free and rain-contaminated data. It should be noted that in Fig.4.9(b), some rain-contaminated data under high wind speed conditions have lower spectral integrations. Different rain rates may lead to different spectral integrations under high wind speeds. This observation may be addressed by considering rain rates in future work. When the wind speed is low (lower than around 5 m/s), the result from rain-contaminated data using the 1D-SA-based method in Fig.4.9(b) is more accurate than the proposed method in Fig.4.9(a). This may be due to the overall underestimation produced by the spectral integrations in the 1D-SA-based method when wind speeds are lower than around 10 m/s. In addition, it may be observed that the rain-contaminated data in Fig.4.9(b) deviates from the rain-free data, whereas the rain-contaminated data in Fig.4.9(a) is consistent with the rain-free data.

The wind speed results obtained using the method outlined here along with that in [19] are compared with the anemometer measurements in Fig.4.14. Again, the 1D-SA-based method in [19] is used for the comparison because it enables wind speed estimation under both rain and rain-free conditions. Both the anemometer and radar results are also moving-averaged over 10 minutes. It may be observed that the proposed

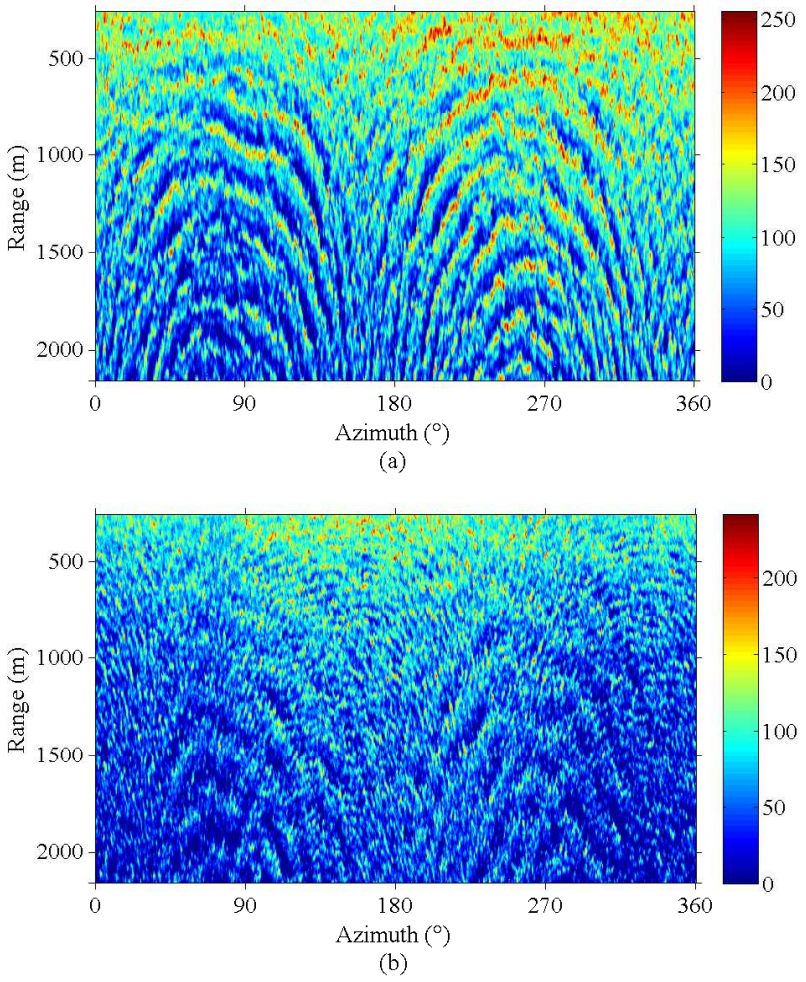

Fig. 4.11 (a) Rain-contaminated radar image collected at 8:22, Nov. 27. Anemometer-measured wind speed is 14.45 m/s. (b) Rain-free radar image collected at 11:01, Dec. 1. Anemometer-measured wind speed is 14.94 m/s.

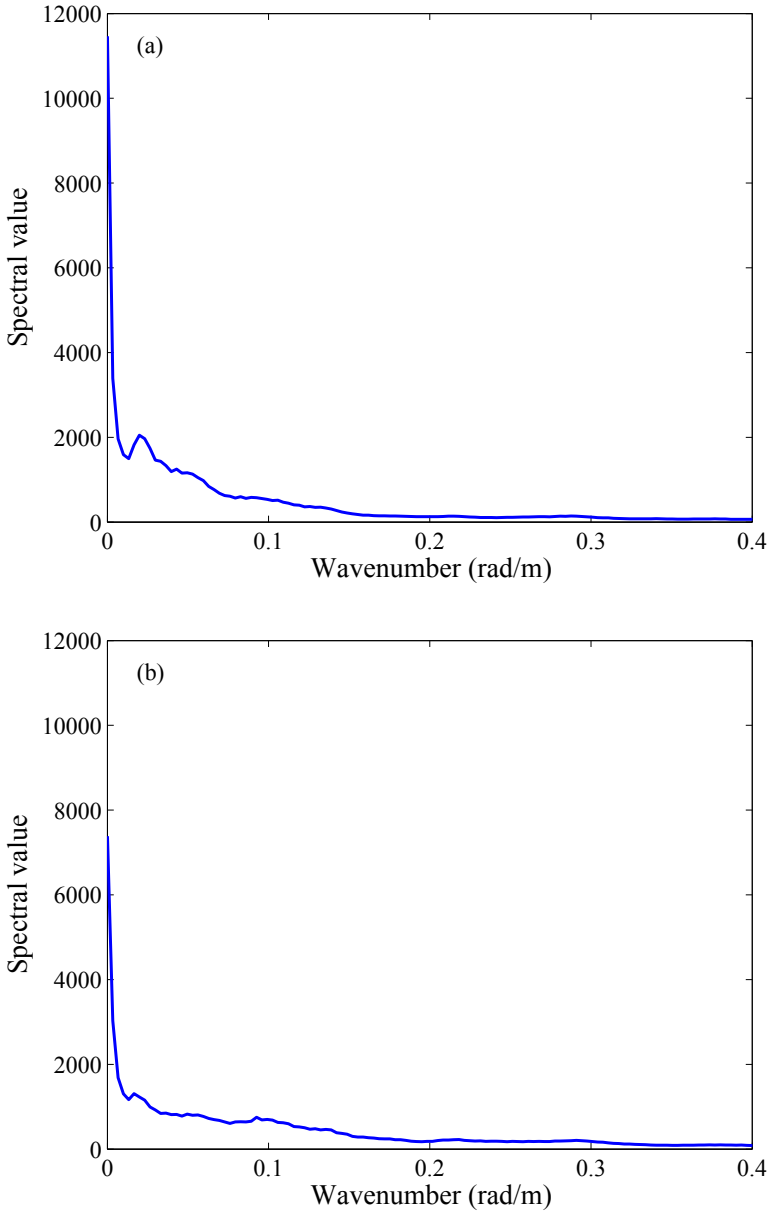

Fig. 4.12 Average wavenumber spectrum over azimuths of: (a) Fig.4.11(a) (zero-wavenumber strength is 11466 and non-zero-wavenumber integration is 49864); (b) Fig.4.11(b) (zero-wavenumber strength is 7384 and non-zero-wavenumber integration is 48695).

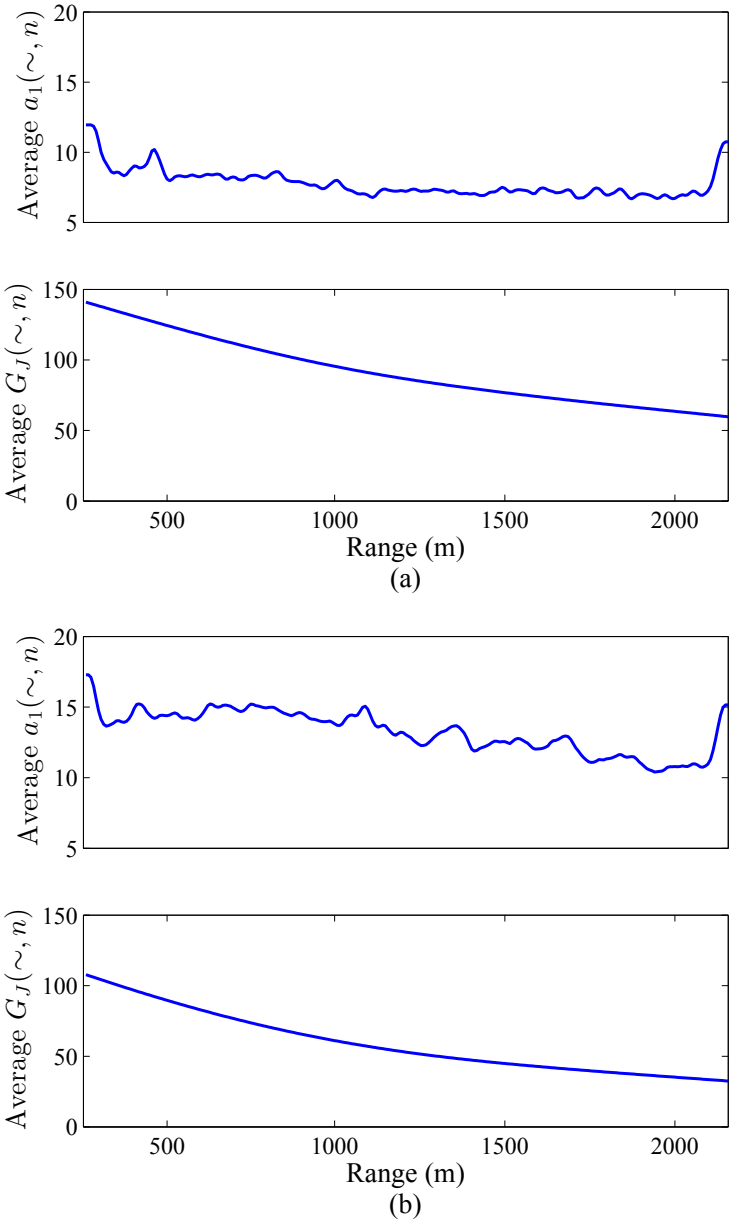

Fig. 4.13 Average $a_1(\sim,n)$ and $G_J(\sim,n)$ over azimuths of: (a) Fig.4.11(a); (b) Fig.4.11(b). The vertical axis represents gray level.

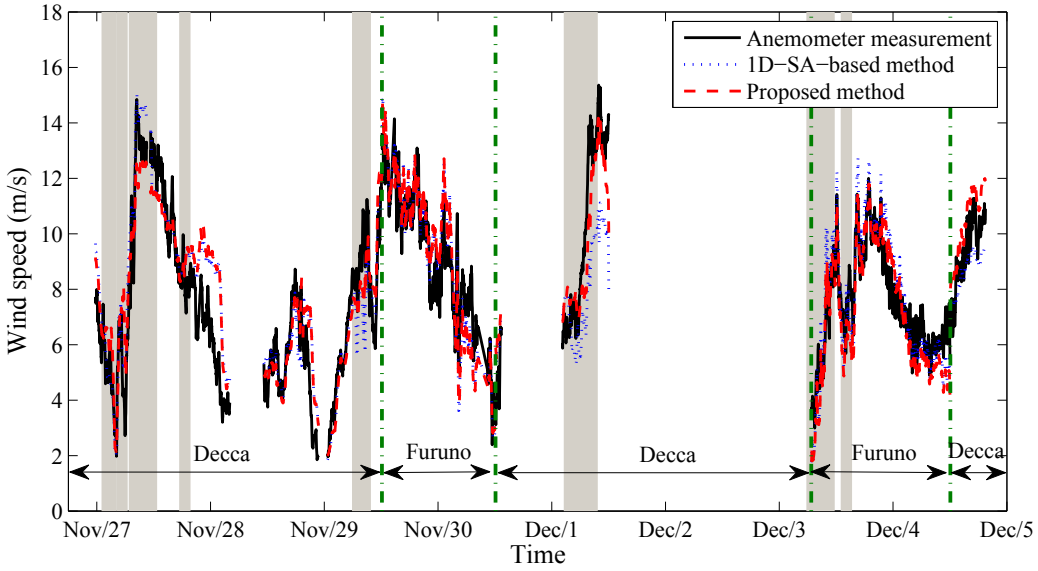

Fig. 4.14 Comparison of the sequences of wind speed results. The results from rain-contaminated data are indicated by the gray shadow.

method generally produces better results than the 1D-SA-based method, especially during the period on Dec. 1 where the wind speed is high. It should be noted that the radar results obtained using both methods deviate relatively significantly from the anemometer measurements for late Nov 27 and early Nov 28. This deviation is because swell-dominated seas existed during this period. The corresponding scatter plots of the radar results and anemometer measurements for these two methods are shown in Fig.4.15. The RMS differences with respect to the reference for the proposed method and the 1D-SA-based method are 1.31 m/s and 1.48 m/s, respectively, for all the data. Furthermore, for rain-free cases, the RMS differences for the proposed method and the 1D-SA-based method are 1.29 and 1.40 m/s, respectively. For rain-contaminated cases, the RMS differences for the proposed method and the 1D-SA-based method are 1.41 and 1.92 m/s, respectively. Improvements are achieved in both cases by the proposed method. The RMSDs displayed in Fig.4.15are only for the test data. It may also be seen from Fig.4.15(a) that, in the low-wind-speed rain cases, the differences between the wind speeds derived from the proposed method and the references are relatively large. This is due to the overestimated M_{com} in Fig.4.9(a) for rain-contaminated data. However, in

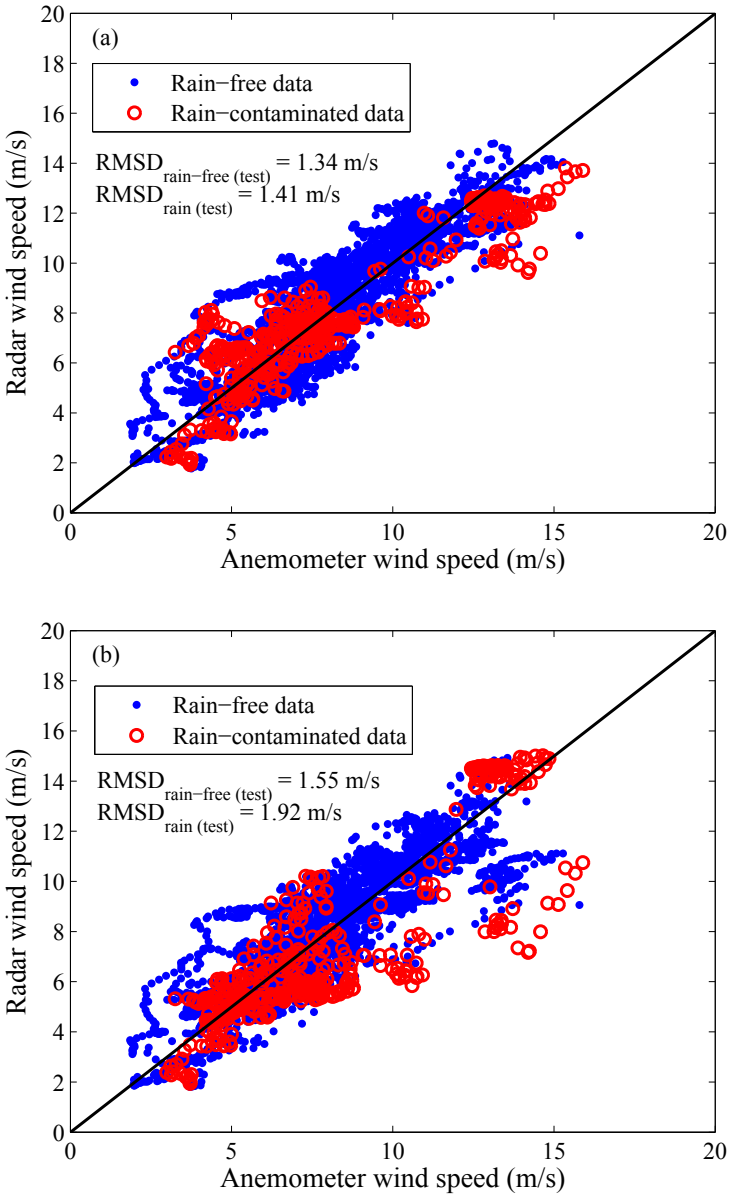

Fig. 4.15 Scatter plots of wind speed results: (a) proposed method; (b) 1D-SA based method. The RMSDs displayed are for test data only.

Table 4.2 Error Statistic Results for Wind Direction Estimation

	Bias total (°)	RMSD total (°)	Bias rain -free (°)	RMSD rain -free (°)	Bias rain (°)	RMSD rain (°)
SA Decca	-5.3	14.3	-4.5	13.1	-9.9	19.3
SA Furuno	-5.1	8.6	-4.8	8.1	-8.2	12.9
EEMD Decca	-5.0	13.2	-4.5	13.1	-7.4	13.5
EEMD Furuno	-4.8	8.4	-4.9	8.1	-3.5	11.3

Table 4.3 Error Statistic Results for Wind Speed Estimation

	Bias training (m/s)	RMSD training (m/s)	Bias testing (m/s)	RMSD testing (m/s)	Bias testing rain -free (m/s)	RMSD testing rain -free (m/s)	Bias testing rain (m/s)	RMSD testing rain (m/s)
SA Decca	0.10	1.05	-0.11	1.87	0.10	1.80	-0.87	2.11
SA Furuno	0.12	1.16	0.10	1.03	0.06	1.00	0.31	1.19
EEMD Decca	0.08	1.17	0.36	1.42	0.63	1.48	-0.18	1.54
EEMD Furuno	0.13	1.25	-0.41	1.03	-0.41	1.05	-0.42	0.95

high wind speed cases, the wind speed results are significantly improved by the proposed method. The biases and RMSDs of the wind speed and direction results for different methods and radar datasets are shown in Table4.2and Table4.3.

It should be noted that the method proposed here produces a similar accuracy to that of the improved intensity-level-selection (ILS) method in [17] for rain-free data. However, rain-contaminated data was discarded in [17]. The method proposed here is able to produce satisfactory results from rain-contaminated data by using the same model as for the rain-free data. Thus, an important advantage of the proposed method is that the rain-free and rain-contaminated data do not have to be trained separately. It is worth

mentioning that the accuracy of the proposed method differs from that in [56]. This difference is mainly due to: 1) The datasets used are different. The radar in [56] was deployed on a stationary platform, but the data analyzed here is from a shipborne system. Undoubtedly, the ship motion will have some effect on radar imaging and, thus, on the wind estimation. 2) The wind speeds determined from rain-contaminated data using the proposed method were included in the error statistics.

4.5 Chapter Summary

In this chapter, a method for estimating wind direction and speed from X-band nautical radar sea surface images based on EEMD and a normalization scheme is presented. The method is feasible for both rain and rain-free conditions. A data control strategy is proposed to separate rain-free and rain-contaminated data and to separate high-wind-speed and low-wind-speed data. EEMD is used to decompose the radar data into several IMFs and a residual. The normalization scheme is applied to the first IMF to obtain its AM part. In wind direction estimation, the residual is used for the rain-free and high-wind-speed rain-contaminated radar data, while the AM part of the first IMF is used for low-wind-speed rain-contaminated radar data. For wind speed measurement, both the residual and the AM part of the first IMF are used for both rain-free and rain-contaminated radar data.

The method is validated using radar and anemometer data collected in a sea trial off the east coast of Canada in late November and early December, 2008. The method is also compared with an earlier 1D-SA-based method described in [18, 19]. For wind direction estimation, it is found that for the proposed method as compared to the 1D-SA-based method, the wind direction results are similar for rain-free data but significantly improved for rain-contaminated data, with a reduction of about 4.9° in the RMS difference. For the proposed wind speed estimation method, the results are improved for both rain-free and rain-contaminated data with reductions of about 0.11 m/s and 0.51 m/s, respectively,

in the RMS differences. Specifically, for the proposed EEMD-based method, the bias and RMS difference of wind direction results are -4.9° and 11.5°, respectively; the bias and RMS difference of wind speed results are 0.14 m/s and 1.31 m/s, respectively.

Chapter 5

Significant Wave Height Estimation

In this chapter, an ensemble empirical mode decomposition (EEMD)-based algorithm and a modified shadowing-based method are proposed for significant wave height (H_S) estimation from X-band marine radar images. The results of both methods are compared with those from the signal-to-noise ratio (SNR)-based method [24]. This chapter proceeds as follows: Sections 5.1 and 5.2 contain the descriptions of the proposed EEMD-based and modified shadowing-based methods, respectively. The experimental results obtained from radar and buoy data are shown in Section 5.3. Section 5.4 contains a summary for the chapter.

5.1 EEMD-Based Algorithm

Before processing, a subarea located in the near half-range (from 240 m to 1200 m in this work) and $\pm 30^{\circ}$ around the upwind direction is extracted from the polar radar image. The reason for doing so is that the sea clutter signals in that region are strong, and can provide more distinct wave signatures. An example of a polar radar image is shown in Fig.5.1, in which the subarea used is marked by a red rectangle.

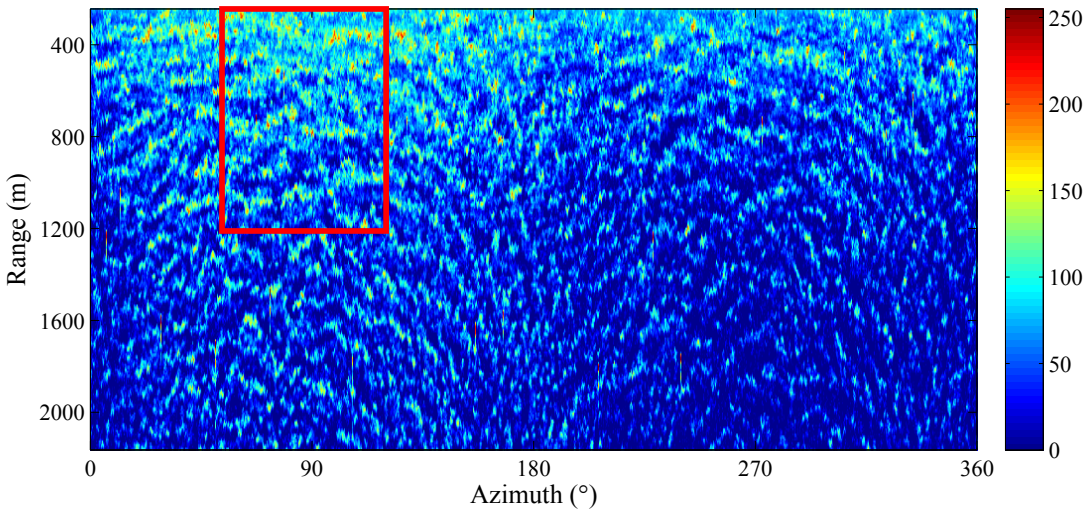

Fig. 5.1 An example of a polar radar image acquired at 0:36, Nov. 27, 2008. The subarea is within the red rectangle.

Then, for the $M' \times N'$ pixel intensities matrix, I_{sub}, of a subarea as given by

$$I_{sub} = \begin{pmatrix} i_{1,1} & i_{1,2} & \dots & i_{1,N'} \\ i_{2,1} & i_{2,2} & \dots & i_{2,N'} \\ \dots & \dots & \dots & \dots \\ i_{M',1} & i_{M',2} & \dots & i_{M',N'} \end{pmatrix}, \tag{5.1}$$

where M' is the number of range cells and N' is the number of azimuth directions. EEMD is applied to each column. Taking the n'th column to be

$$I_{sub}(\sim, n') = \begin{pmatrix} i_{1,n'} \\ i_{2,n'} \\ \dots \\ i_{M',n'} \end{pmatrix}, \tag{5.2}$$

for example, the corresponding EEMD result may be written as

$$I_{sub}(\sim,n') = \sum_{j=1}^{5} D_j(\sim,n') + R(\sim,n'), \tag{5.3}$$

where $D_j(\sim,n')$ is the jth IMF of $I_{sub}(\sim,n')$ expressed as

$$D_j(\sim,n') = \begin{pmatrix} d_{1,n',j} \\ d_{2,n',j} \\ \cdots \\ d_{M',n',j} \end{pmatrix}, \tag{5.4}$$

and $R(\sim,n')$ is the residual of $I_{sub}(\sim,n')$ which may be written as

$$R(\sim,n') = \begin{pmatrix} r_{1,n'} \\ r_{2,n'} \\ \cdots \\ r_{M',n'} \end{pmatrix}. \tag{5.5}$$

It should be noted that in this work, the radar data is decomposed into 5 IMFs (i.e., j ranges from 1 to 5) and a residual by the EEMD. Technically, the data can be decomposed into more than 5 IMFs, but it is not necessary because the magnitudes of additional IMFs are negligible compared to the first 5. To establish whether this number may be used as a rule of thumb will require further testing with data collected under a variety of conditions. An example of resultant IMFs derived from $I_{sub}(\sim,1)$ in Fig.5.1is shown in Fig.5.2. In order to indicate the insignificance of higher-order IMFs, the sixth IMF is shown in Fig.5.2as the red line.

Next, a normalization scheme [36] is applied to each IMF, $D_j(\sim,n')$, resulting in

$$D_j(\sim,n') = A_j(\sim,n') \circ F_j(\sim,n'), \tag{5.6}$$

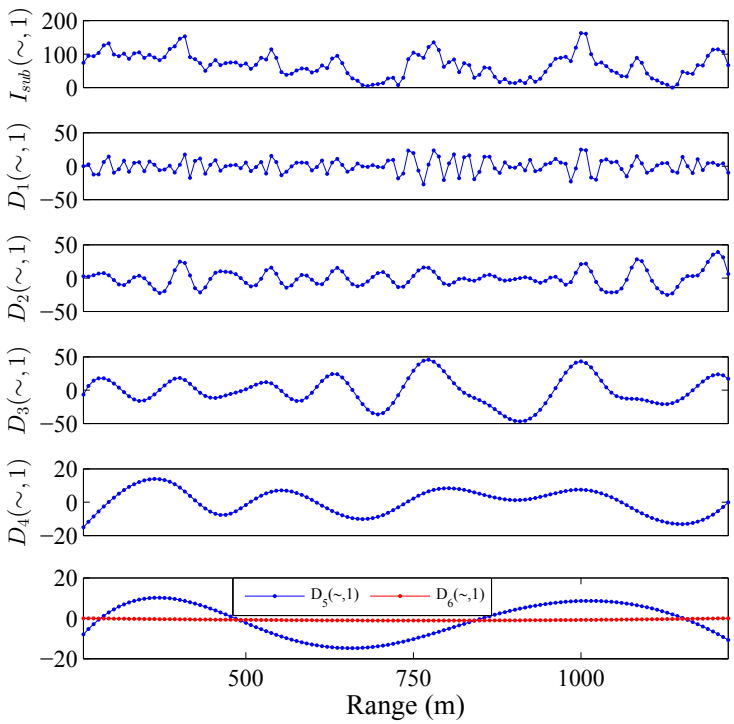

Fig. 5.2 An example of resultant IMFs derived from $I_{sub}(\sim,1)$ in Fig.5.1. The vertical axis represents gray level.

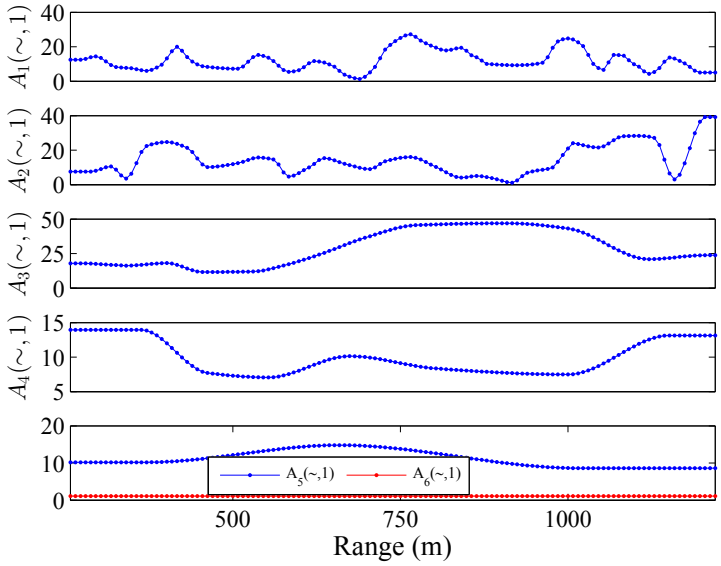

Fig. 5.3 An example of resultant AM portions derived from $C_j(\sim,1)$ in Fig.5.2. The vertical axis represents gray level.

where $\circ$ denotes the element-by-element multiplication of two vectors, and $A_j(\sim, n')$, expressed as

$$A_j(\sim, n') = \begin{pmatrix} a_{1,n',j} \\ a_{2,n',j} \\ \cdots \\ a_{M',n',j} \end{pmatrix}, \tag{5.7}$$

and $F_j(\sim, n')$, represented as

$$F_j(\sim, n') = \begin{pmatrix} f_{1,n',j} \\ f_{2,n',j} \\ \cdots \\ f_{M',n',j} \end{pmatrix}, \tag{5.8}$$

are the AM and FM portions, respectively, of $D_j(\sim, n')$. An example of the resultant AM portions derived from $D_j(\sim, 1)$ in Fig.5.2is shown in Fig.5.3. From Fig.5.3, it is clear that the AM portion of the sixth IMF is much lower than that of IMFs 2-5.

Finally, after the above procedure is conducted for each column of I_{sub}, a parameter, A_{SWH}, is defined as

$$A_{SWH} = \frac{1}{N'} \frac{1}{M'} \sum_{n'=1}^{N'} \sum_{m'=1}^{M'} \sum_{j=2}^{5} a_{m',n',j}. \tag{5.9}$$

Similarly as in [24], a linear relationship between H_S and A_{SWH} can be established through a curve-fitting process as

$$H_S = p_0 + p_1 \cdot A_{SWH}, \tag{5.10}$$

where p_0 and p_1 are coefficients determined by curve fitting A_{SWH} with H_S measured by buoy. After the coefficients are determined, H_S can be estimated from different A_{SWH} according to (5.10). It should be noted that only the AM portions from the second IMF to the fifth IMF are used for the H_S estimation. This choice was made purely on the

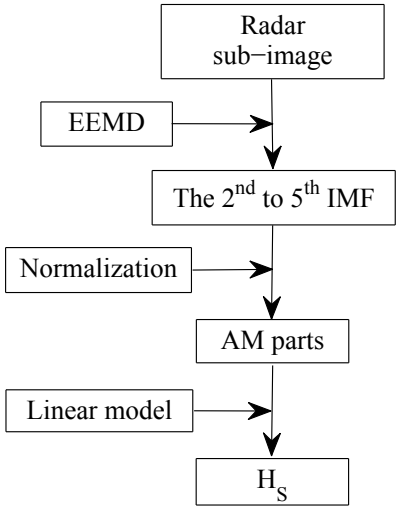

Fig. 5.4 Basic steps of the EEMD-based algorithm.

basis of the fact that, for the dataset used here, inclusion of the first IMF caused marginal reduction in the accuracy of the results. The underlying physical reason for this has not yet been determined and will likely require further investigation using more data collected under a greater variety of wave and wind conditions. The basic steps of the EEMD-based algorithm are depicted in Fig.5.4.

5.2 Modified Shadowing-Based Algorithm

Modifications made to the original shadowing-based algorithm [25] in order to improve the accuracy of the H_S estimation result are described in this section. Moreover, unlike [25], to make the algorithm fully independent of external sensors, the average zero-crossing wave periods derived from radar rather than buoy data are used for H_S calculation in this modified shadowing-based algorithm.

5.2.1 Subarea Selection

The intensity level difference of an edge pixel from its adjacent pixels depends on range and direction. This is because the backscatter signals are stronger and the intensity

level differences between shadow and no shadow are larger at near ranges and in the upwind direction. As described in Section 2.2.2.4-A, the shadow threshold intensity τ_S for the shadowing-based algorithm is selected based on the pixels with the highest B-percentile of intensity level differences. Applying such a uniform τ_S to the whole image may result in overestimation of shadowed areas for the portion in the far range or directions other than upwind. However, it will not significantly affect the edge detection for near ranges and upwind direction. Although the range dependency has been considered in the original shadowing algorithm in which the data from far ranges are not used for calculating illumination ratio, root-mean-square (RMS) surface slope and significant wave height [25], the average RMS surface slope is derived from all the azimuth directions in one shadow image. Because of the dependence of radar backscatter on wind direction, the image portions in the azimuths far from the upwind direction will have lower sea clutter intensities, and this may result in overestimation of shadowed areas and the corresponding wave height. Here, a single subarea is selected from the portion $\pm 5^\circ$ around the upwind direction in each shadow image for one RMS surface slope estimation since the clutter signal is stronger in those directions and more robust results may be obtained. The usual technique for determining the upwind direction is found in [15]. After obtaining all the RMS surface slopes from all the images in one time sequence, an average RMS surface slope is calculated.

5.2.2 Edge Pixel Intensity Histogram Smoothing

In [25], the shadow threshold is directly determined as the intensity value corresponding to the highest occurrence of the intensity histogram of edge pixels. This is viable when the distribution is smooth. However, in this work, the data has a small gray scale depth (8-bit, i.e. 0-255) and a relatively small number of pixels. Thus, the shadow threshold may not be correctly determined by seeking the highest occurrence of the histogram. In order to improve the accuracy of this threshold, a smoothing process using a spline function is

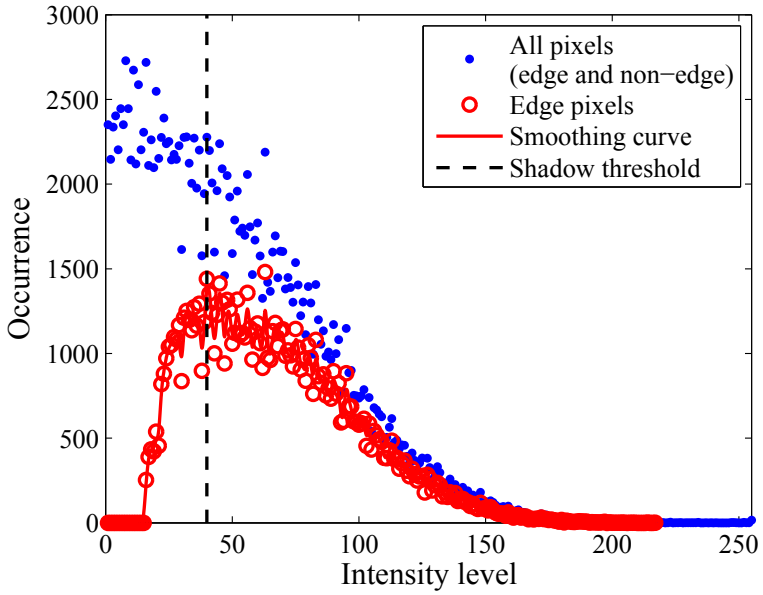

Fig. 5.5 Statistical distribution of the edge pixel gray level for the radar data collected at 0:01, Nov. 27, 2008.

first applied to the edge pixel intensity histogram, and the threshold is estimated from the smoothed result. The statistical distribution of the edge pixel gray level for the radar data used here is shown in Fig.5.5. The result from the figure was generated by one radar image. It can be seen from the figure that the smoothing procedure proposed in this work can achieve the accurate shadow threshold for the radar data, by excluding the outlier edge pixels located within the intensity level of 50 to 100.

5.3 Experimental Results

5.3.1 Data Overview

The same datasets as used in previous chapters are employed to test the proposed methods. During the data collection period, the sea was mainly dual-mode (wind and swell) sea. The reference H_S were measured by two free-floating Triaxys directional wave buoys deployed approximately 10 km away from the radar. From Section 5.1 it is clear that the proposed method is able to produce one H_S estimate from a single frame of the radar

images after the training procedure is completed. It should be noted that each radar image sequence of 32 images was recorded approximately every two minutes, and that only one image from each image sequence was used to estimate H_S. Since the buoys produced 30-minute-averaged H_S measurements, the radar-derived H_S were averaged over 30-minute intervals for comparison with the buoy references. 168 records of H_S pairs were used for the radar-buoy comparisons in this study.

5.3.2 Experimental Results

Radar and buoy data from 0:00, Nov. 27 to 2:50, Nov. 28 and from 12:30 to 19:30, Dec. 4 are used to train the linear relationship between H_S and A_{SWH}, as depicted in Fig.5.6(a). Note that the rain-affected data shown in Fig.5.6(a) are not included in the training and the following statistical analysis. Based on this relationship, the H_S results obtained by the EEMD-based method are compared with the buoy-measured H_S by means of a scatter plot shown in Fig.5.6(b). It can be seen that the H_S retrieved by the EEMD-based method agree well with the buoy references. The correlation coefficient is around 0.91 and the root-mean-square (RMS) difference is around 0.36 m. For the H_S results obtained using the modified shadowing-based method shown in Fig.5.6(c), the correlation coefficient is around 0.84 and the RMS difference is around 0.48 m.

For comparison purposes, the scatter plots of the H_S results determined using the SNR-based method [24] based on same data are shown in Fig.5.6(d). The SNR-based method is used in the comparison because it is the most widely accepted method for H_S estimation. It should be mentioned that the same set of training data is used for the calibration required for the SNR-based method. It can be seen that the proposed EEMD-based and modified shadowing-based methods outperform the SNR-based method in the H_S estimation, with improvements of about 0.30 and 0.23, respectively, in the correlation coefficient, and reductions of about 0.42 m and 0.30 m, respectively, in the RMS difference with respect to the buoy reference. Note that the training process and

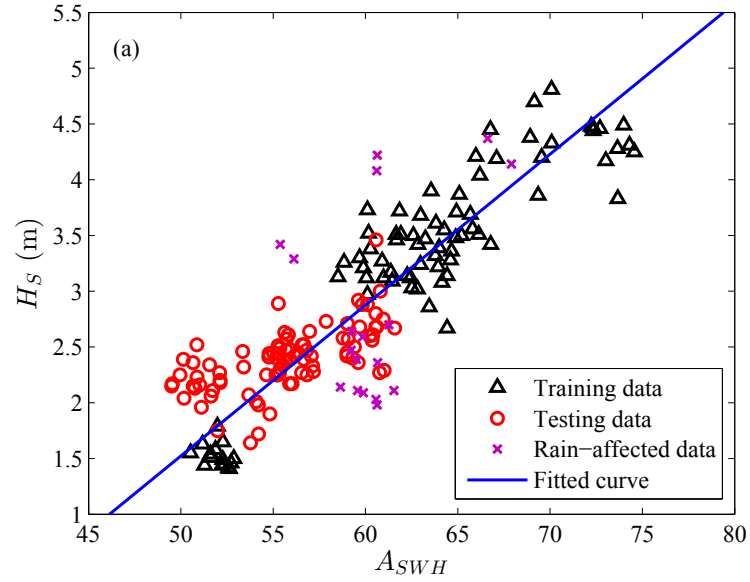
(a)
H_S (m)
A_{SWH}
Training data
Testing data
Rain−affected data
Fitted curve

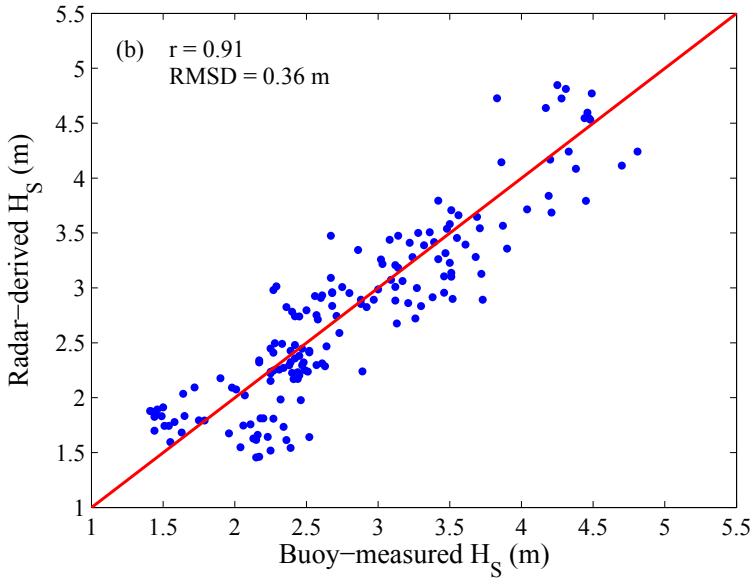
(b)
r = 0.91
RMSD = 0.36 m
Radar−derived H_S (m)
Buoy−measured H_S (m)

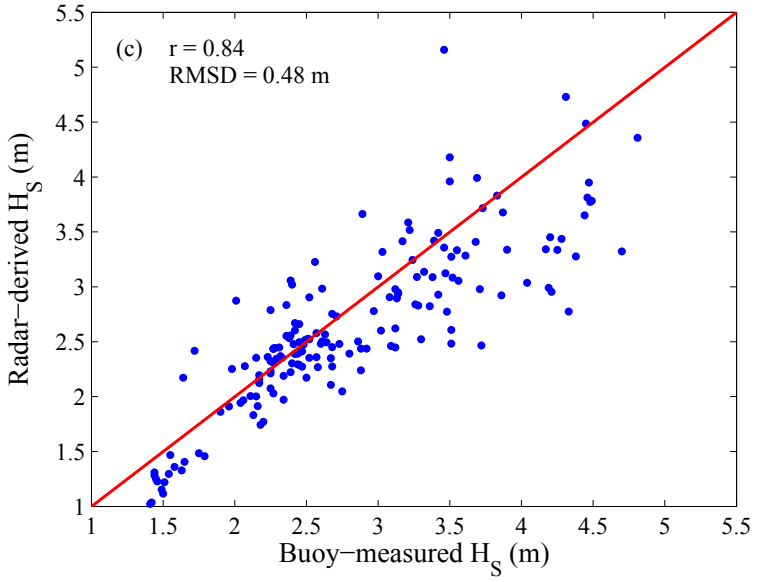
(c)
r = 0.84
RMSD = 0.48 m
Radar−derived H_S (m)
Buoy−measured H_S (m)
5.5
5
4.5
4
3.5
3
2.5
2
1.5
1
1
1.5
2
2.5
3
3.5
4
4.5
5
5.5

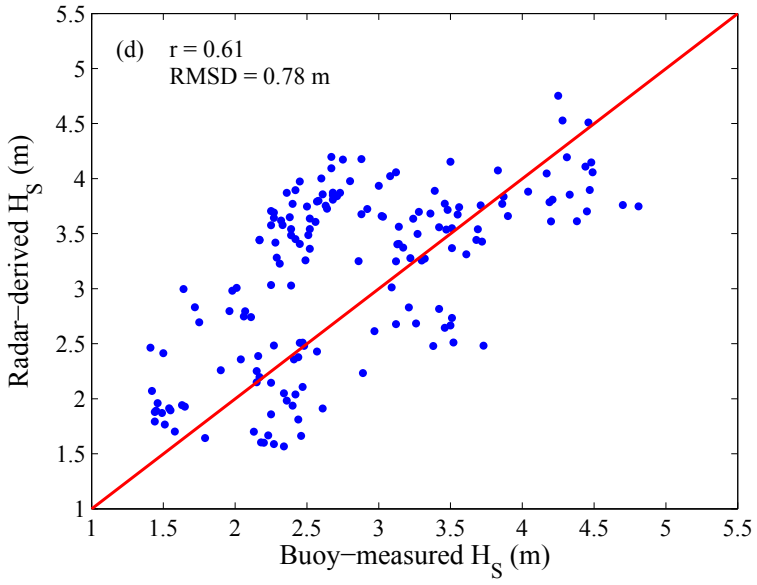
(d)
r = 0.61
RMSD = 0.78 m
Radar−derived H_S (m)
Buoy−measured H_S (m)
5.5
5
4.5
4
3.5
3
2.5
2
1.5
1
1
1.5
2
2.5
3
3.5
4
4.5
5
5.5

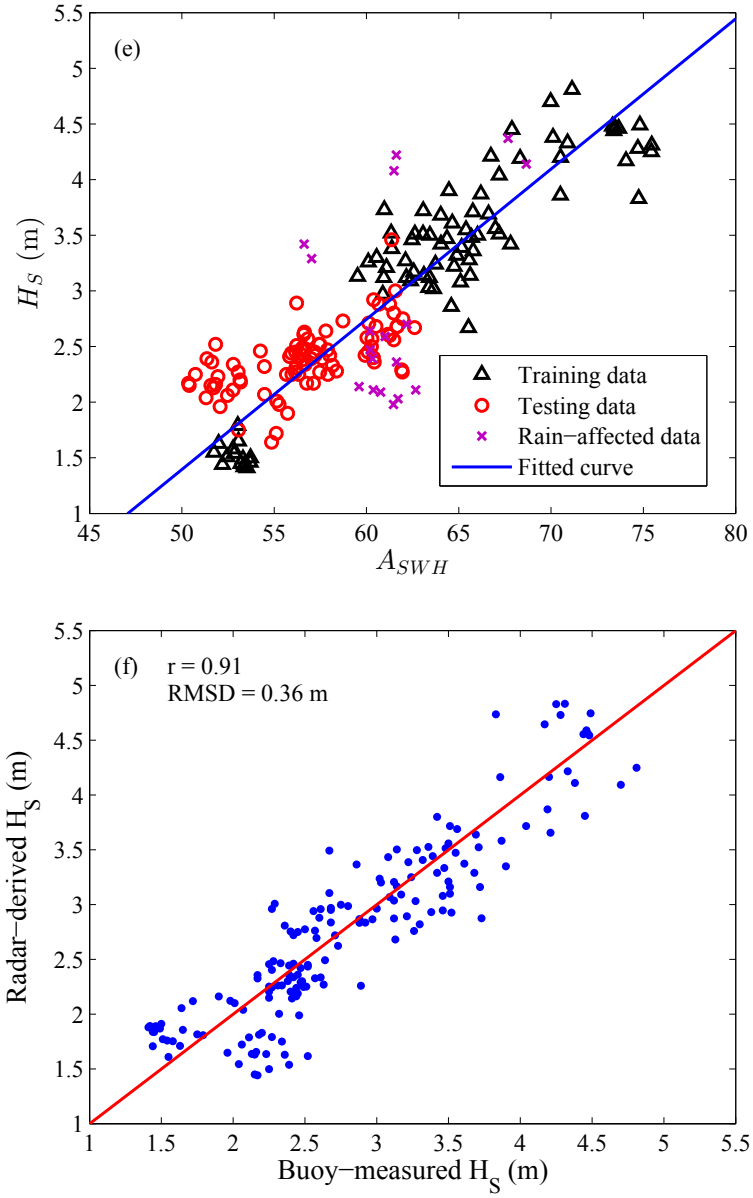

Fig. 5.6 (a) Linear relationship between H_S and A_{SWH}: H_S = -5.241 + 0.1353A_{SWH}; (b) scatter plot of the buoy-measured and radar-derived H_S; (c) modified shadowing-based method; (d) SNR-based method (calibration model: H_S = -0.09246 + 3.685$\sqrt{SNR}$); (e) Linear relationship between H_S and A_{SWH}: H_S = -5.355 + 0.135A_{SWH} (using IMF 2-6); (f) scatter plot of the buoy-measured and radar-derived H_S (using IMF 2-6).

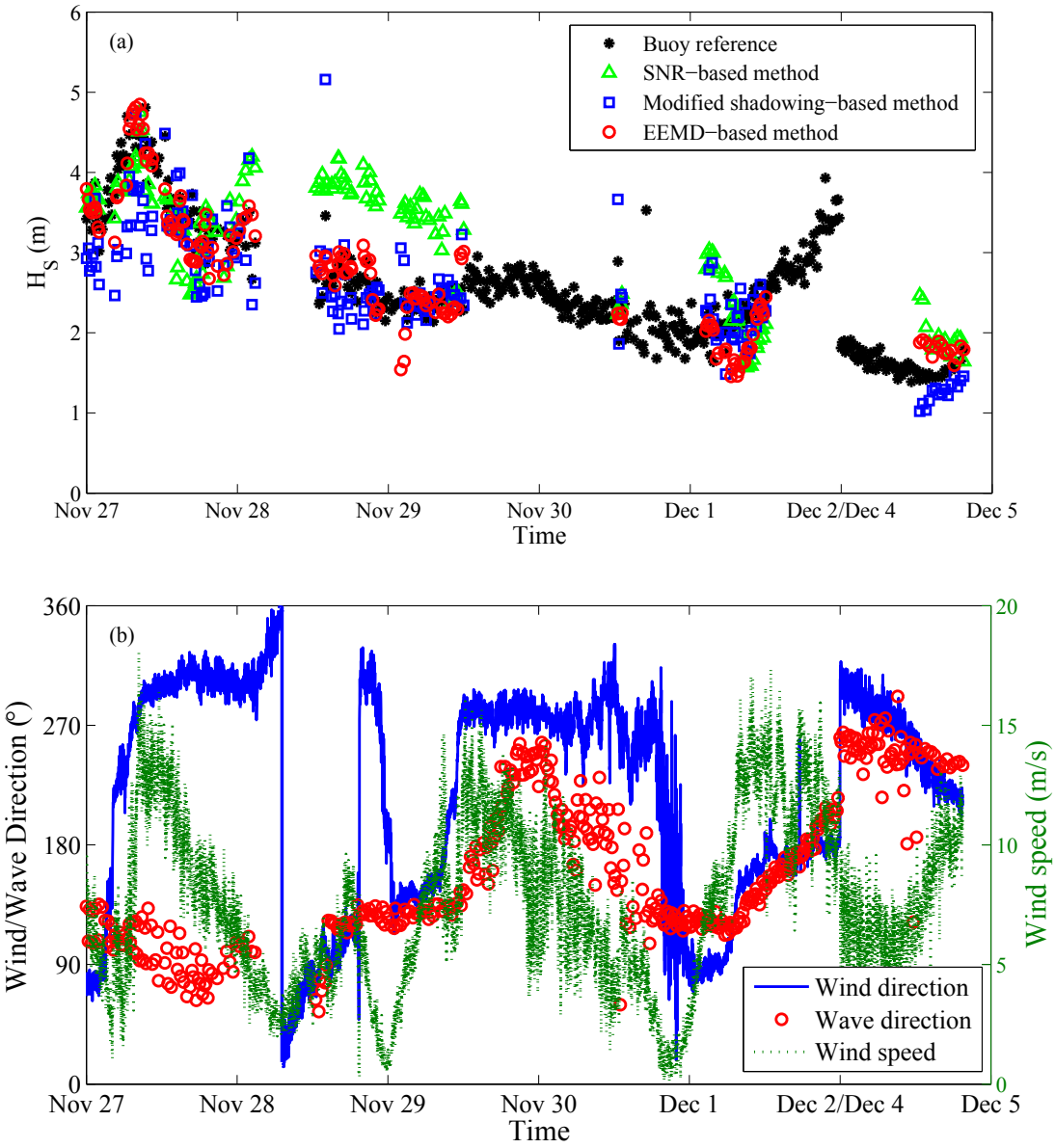

Fig. 5.7 (a) Time sequences of H_S results derived by the proposed EEMD-based method, the SNR-based method, and the modified shadowing-based method, comparing with buoy references. (b) Anemometer-measured wind speed and direction as well as buoy-measured wave direction.

Table 5.1 Inter-Comparison of H_S Estimation Methods

Methods	SNR-based	Modified shadowing-based	EEMD-based
Wave Spectrum Estimation	$\surd$	$\times$	$\times$
Wave Height Estimation	$\surd$	$\surd$	$\surd$
RMS Difference of H_S Estimation (m)	0.78	0.48	0.36
Calibration-Free	$\times$	$\surd$	$\times$
Images Required	Multiple	Single	Single

estimation results using more IMFs (2-6) are shown in Fig.5.6(e) and (f), respectively. It may be observed that they are similar to Fig.5.6(a) and (b) in which only IMFs 2-5 are used. Moreover, the time sequences of the H_S results derived using these three methods and the buoy data are shown in Fig.5.7(a). The gaps in Fig.5.7(a) are due to the removal of rain-contaminated data and the fact that no radar or buoy data were available. It may also be observed that the H_S results derived from shipborne radar data using the proposed methods agree better with the buoy references than those from the SNR-based method. Anemometer-measured wind speed and direction as well as buoy-measured wave direction are shown in Fig.5.7(b). It may be seen from Fig.5.7(b) that swell appeared for most of the experiment period, especially on Nov 27 when the wave heights were large. The inter-comparison of methods for H_S estimation is shown in Table5.1.

5.4 Chapter Summary

In this chapter, an EEMD-based method and a modified shadowing-based method to estimate H_S from X-band marine radar images are proposed. Satisfactory H_S results are obtained with a correlation coefficient of around 0.91 and a RMS difference of around 0.36 m for the EEMD-based method, and a correlation coefficient of around 0.84 and a RMS difference of around 0.48 m for the modified shadowing-based method, with

respect to the buoy reference. Moreover, an inter-comparison shows that the proposed methods outperform the SNR-based method with improvements of about 0.42 m and 0.30 m, respectively, in the RMS difference with respect to the buoy reference. This appears to indicate that the proposed methods are more robust than the SNR-based method for ship-borne radar applications.

Chapter 6

Wave Direction and Period Estimation

In this chapter, an algorithm based on the Radon transform (RT) is proposed to estimate wave parameters, including wave direction, peak wave period, and mean wave period, from X-band marine radar images. The chapter proceeds as follows: In Section 6.1, the proposed algorithm is described. The experimental results obtained from radar and buoy data are presented in Section 6.2. Section 6.3 contains a summary for the chapter.

6.1 RT-Based Algorithm

The RT is defined as [109]

$$f_{RT}(\xi, r_d) = \iint s(x,y)\delta(r_d - x\cos\xi - y\sin\xi)dxdy, \tag{6.1}$$

where $s(x,y)$ is the intensity level of an image at position (x,y) in the Euclidean domain, r_d is the normal distance from the center of the image to a straight line, ξ is the projection direction of the straight line, which is the angle between the orthogonal of the straight line and the x-axis, and δ is the Dirac delta function. The definition of the RT is illustrated in Fig.6.1.

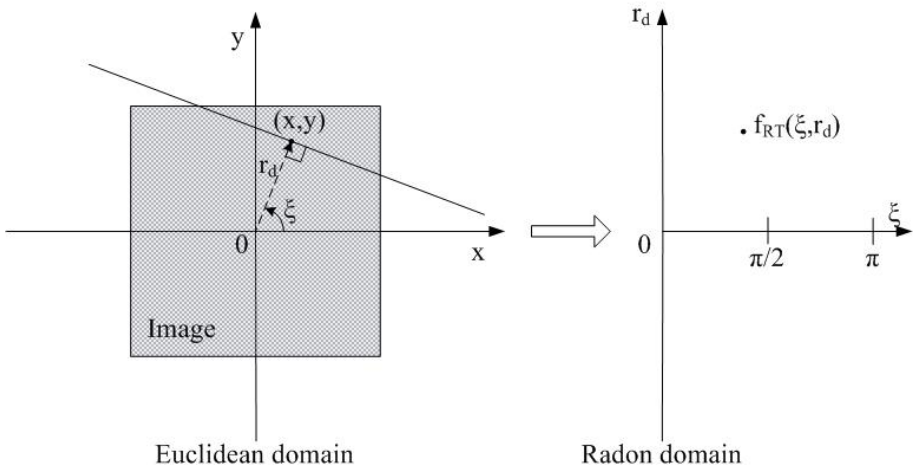

Fig. 6.1 Diagram for the definition of the RT.

6.1.1 Data Preprocessing

Before applying the RT to the radar data, some preprocessing is required. First, since they may obscure the wave signatures, noise lines due to interference from other marine radars are removed from the radar images as in Section 3.4.2. Secondly, since homogeneous radar images are required for the algorithm, radar backscatter heterogeneity observed in radar images due to range and azimuth dependence is removed using the methods presented in [44]. Thirdly, radar images are geo-referenced as in [110] since the radar in this work was mounted on a moving ship, and incorrect positions of the centres of radar images will negatively affect the estimation of wave parameters.

6.1.2 Initial Guess of Wave Direction

The first image of each radar image sequence is used to obtain an initial guess of the wave direction. As shown in Fig.6.2, 8 slightly overlapping sub-images, covering all mid-range azimuths, are extracted from the first image of an image sequence. Next, the RT is applied to each sub-image. Examples of one sub-image and its RT result are depicted in Figs.6.3(a) and6.3(b), respectively. Fig.6.3(c) is the standard deviation of the RT result as a function of projection direction for Fig.6.3(b). Then, as in [44], the standard deviations of the RT results as a function of projection direction for all

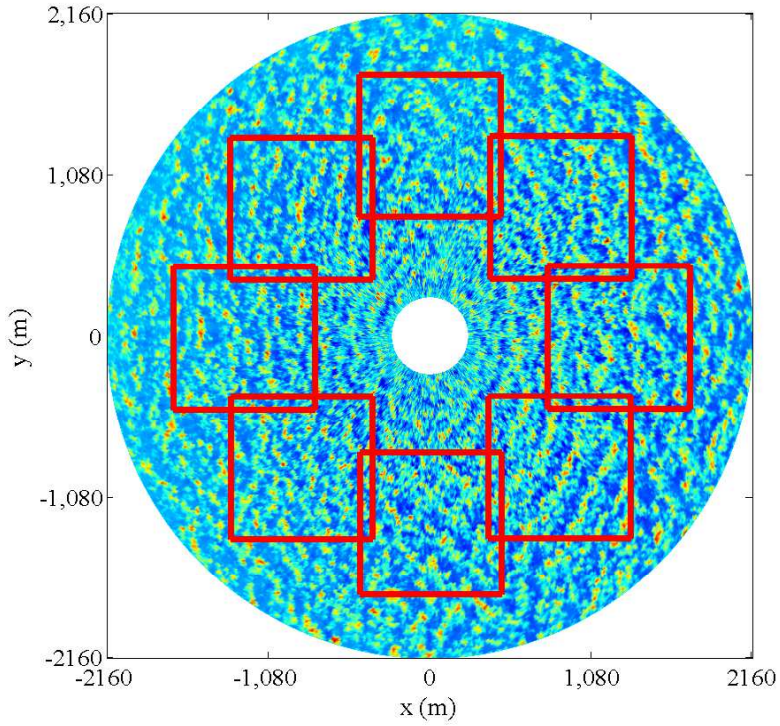

Fig. 6.2 Radar image with 8 sub-images shown as red squares.

sub-images are averaged, and the projection direction corresponding to the peak averaged standard deviation is considered as the initial guess for the wave direction. Note that an ambiguity of 180° exists in the estimation since whether the wave is propagating from or to that direction cannot be determined. This problem will be addressed in subsequent steps.

6.1.3 Wave Direction Update

Having obtained an initial guess for the wave direction, two sets of sub-images, one located in that direction and the other in the opposite direction, are extracted from each image of the image sequence. Then, the RT is applied to all these new sub-images, and the standard deviations of these transform results as a function of projection direction are averaged for each projection direction. The wave direction is updated as the

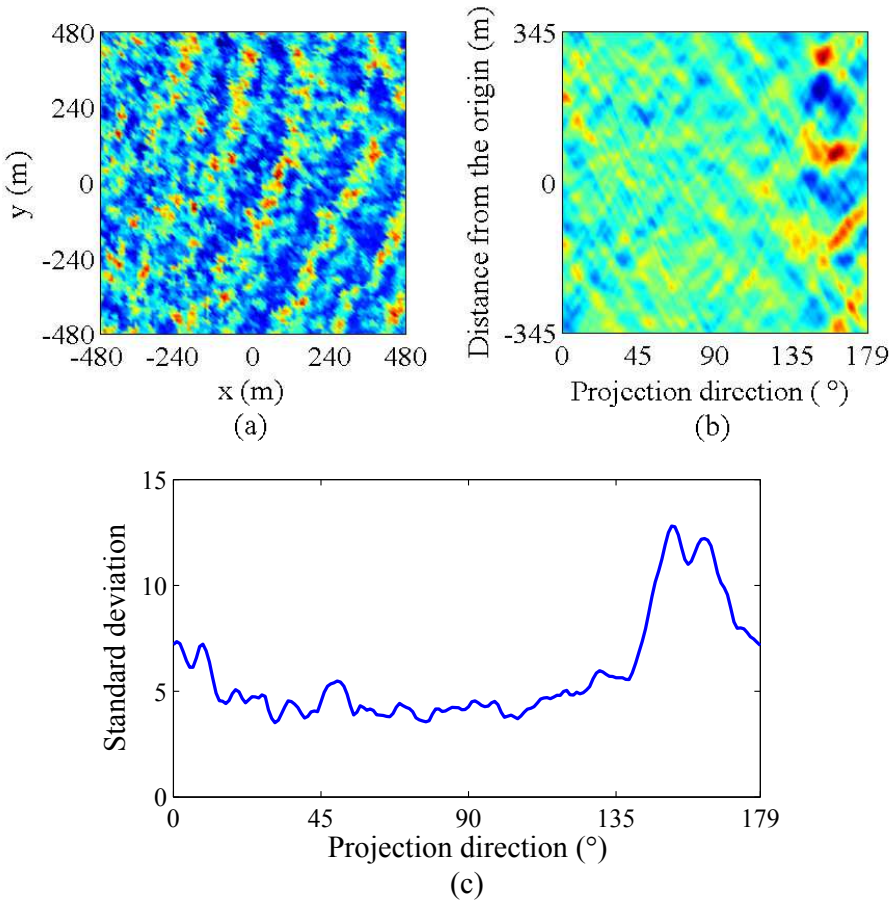

Fig. 6.3 (a) One sub-image from Fig.6.2. (b) RT result of the sub-image in Fig.6.3(a). (c) Standard deviation of the RT result as a function of projection direction for Fig.6.3(b).

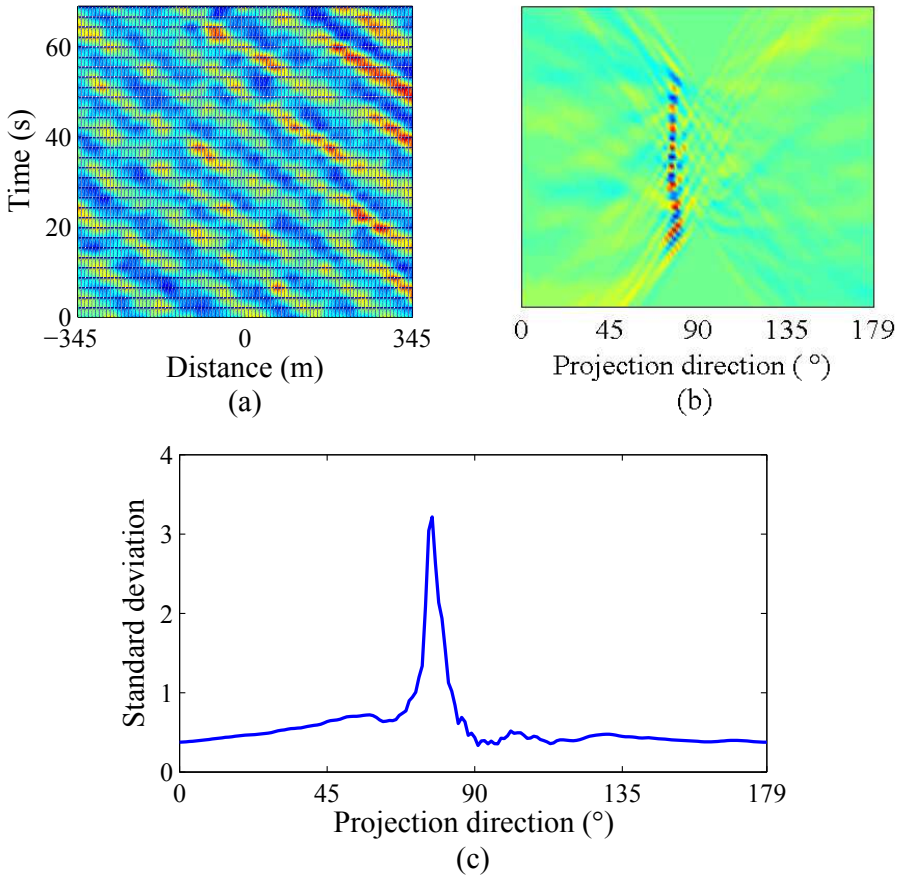

Fig. 6.4 (a) Construction of intensity sequences extracted along the wave direction from the RT results. (b) RT of the construction in Fig.6.4(a). (c) Standard deviation of the RT result as a function of projection direction for Fig.6.4(b).

projection direction corresponding to the peak averaged standard deviation, but still with an ambiguity of 180°.

6.1.4 Wave Direction Ambiguity Removal

For each set of sub-images, intensity sequences along the updated wave direction in all the RT results are extracted and arranged along the time axis as shown in Fig.6.4(a), from which the propagation of wave crests and troughs with time can be observed. From the intensity distribution over distance and time in Fig.6.4(a), it can be clearly seen that each wave crest (or trough) propagates from right to left with time. Thus, the ambiguity of 180° can be removed.

6.1.5 Dominant Wave Speed and Peak Wave Period

Wave speed can be trivially calculated as the ratio of the distance a wave travels to the time it takes the wave to travel that distance. Therefore, with the distance and time information, dominant wave speed can be obtained from the dominant projection direction of the wave signatures in Fig.6.4(a). In order to determine the dominant projection direction, the RT is applied to Fig.6.4(a), the result of which is shown in Fig.6.4(b), and the standard deviation of the RT result as a function of projection direction is shown in Fig.6.4(c). Again, the standard deviations of the RT results of two time-distance images (one for each set of sub-images) as a function of projection direction are averaged. Then, the dominant projection direction ξ_D is the projection direction corresponding to the peak averaged standard deviation, and the dominant wave speed v_D can be calculated from the dominant projection direction ξ_D as

$$v_D = |\tan \xi_D| . \tag{6.2}$$

Peak wave period T_p can then be calculated from the dominant wave speed v_D based on the wave dispersion relationship as

$$T_p = \frac{2\pi v_D}{g}, \tag{6.3}$$

where g is the gravitational acceleration.

6.1.6 Mean Wavelength and Mean Wave Period

Since each row of the time-distance image in Fig.6.4(a) represents a waveform at a time index, mean wavelength λ_M can be estimated by detecting the average distance between adjacent zero-crossings in each row of the time-distance images. Then, mean wave period T_{m02} can then be calculated from the mean wavelength λ_M based on the

wave dispersion relationship as

$$T_{m02} = \sqrt{\frac{2\pi\lambda_M}{g}}. \tag{6.4}$$

It should be noted that (6.3) and (6.4) can only be applied to deep ocean waves.

6.2 Experimental Results

6.2.1 Data Overview

The same datasets as used in previous chapters are employed to test the proposed algorithm. Two free-floating Triaxys directional wave buoys, which were deployed approximately 10 km away from the radar, were used to obtain reference wave parameters. Since the buoys provided averaged measurements every 30 minutes, the wave parameters derived from the radar data were also averaged every 30 minutes for comparison with the buoy references.

6.2.2 Results

The estimation results for wave direction, peak wave period, and mean wave period are shown in Figs.6.5,6.6, and6.7, respectively. The results derived from the traditional Fourier-based algorithm are also shown for comparison purposes because it is the most widely used approach for wave parameter estimation. The red rectangles in the time sequences of the figures indicate that the buoys did not work properly during those periods. Therefore, data in those periods are not included in the scatter plots and statistical analyses. It can be seen from the statistics that, compared to the traditional Fourier-based algorithm, the estimation results are improved by the RT-based algorithm with an increase of 0.01, 0.03, and 0.05 in the correlation coefficient and decrease of 1.2°, 0.15 s, and 0.40 s in the root-mean-square (RMS) difference for the wave direction, peak

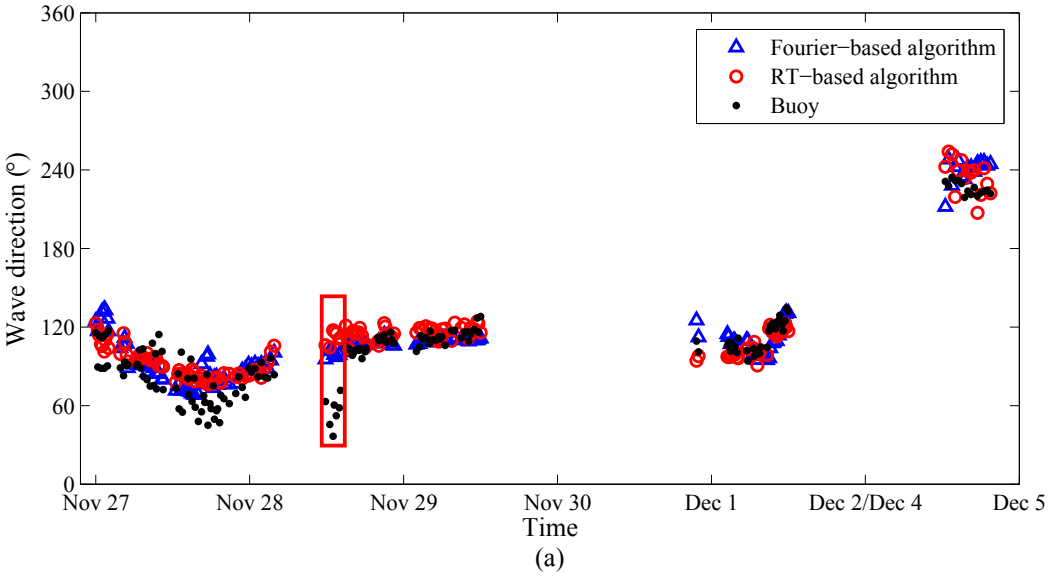
Fourier−based algorithm
RT−based algorithm
Buoy
Wave direction (°)
360
300
240
180
120
60
0
Nov 27
Nov 28
Nov 29
Nov 30
Dec 1
Dec 2/Dec 4
Dec 5
Time

(a)

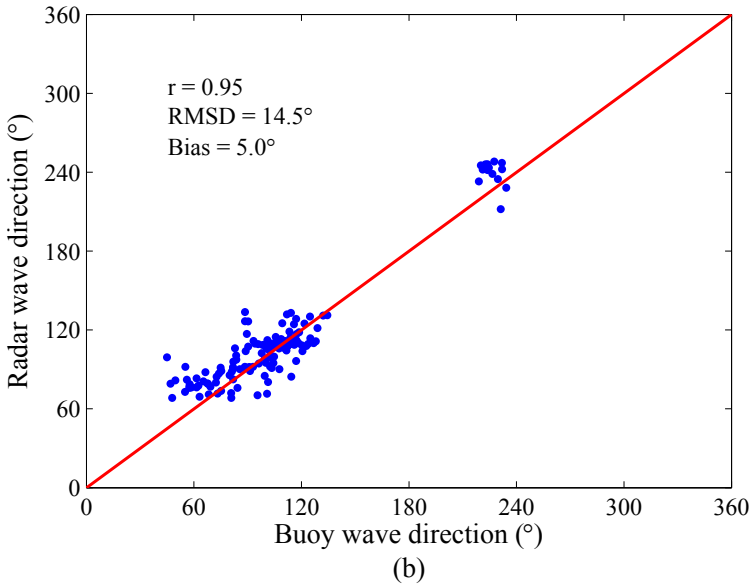
r = 0.95
RMSD = 14.5°
Bias = 5.0°
Radar wave direction (°)
Buoy wave direction (°)
0
60
120
180
240
300
360

(b)

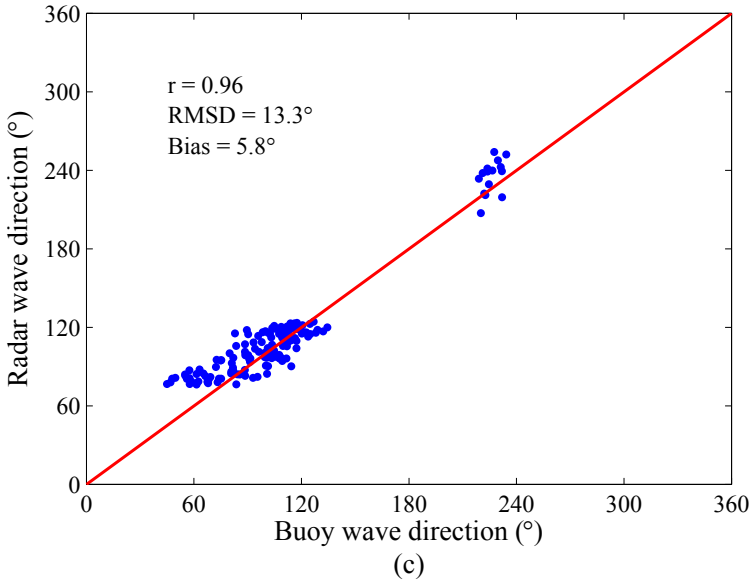

(c)

Fig. 6.5 (a) Comparison of time sequences of wave directions estimated from Fourier-based algorithm and RT-based algorithm. (b) Scatter plot of wave direction estimates from a Fourier-based algorithm. (c) Scatter plot of wave direction estimates from the RT-based algorithm.

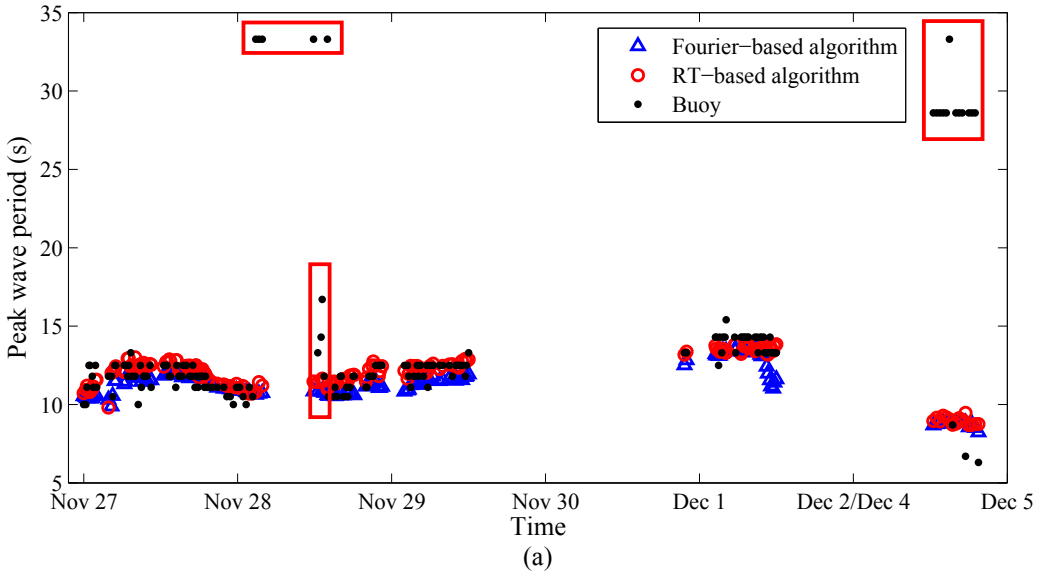

(a)

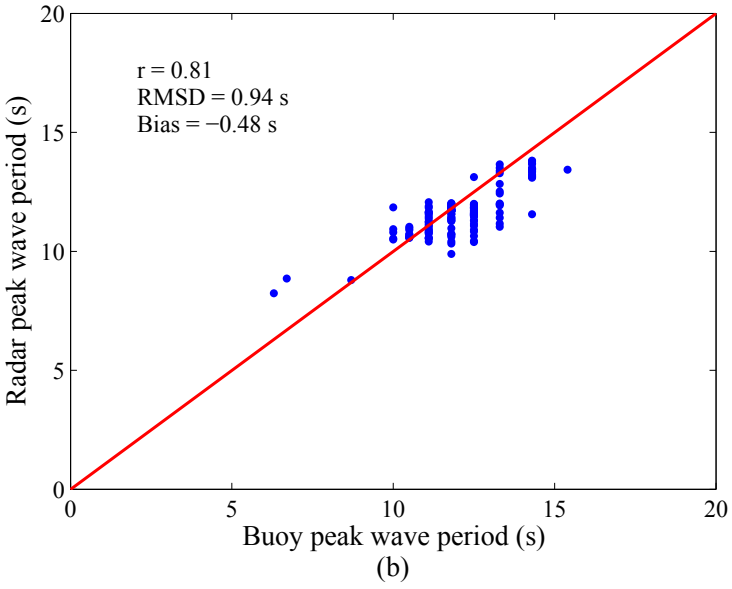

(b)

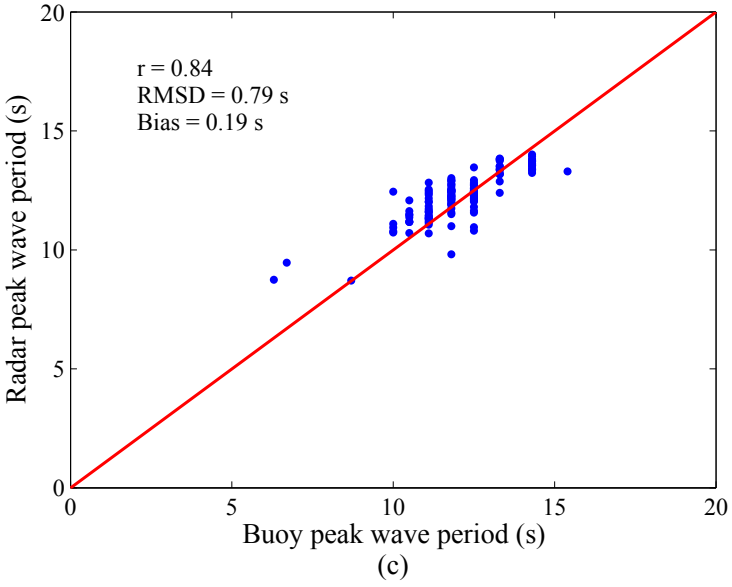

(c)

Fig. 6.6 (a) Comparison of time sequences of peak wave periods estimated from Fourier-based algorithm and RT-based algorithm. (b) Scatter plot of peak wave period estimates from a Fourier-based algorithm. (c) Scatter plot of peak wave period estimates from the RT-based algorithm.

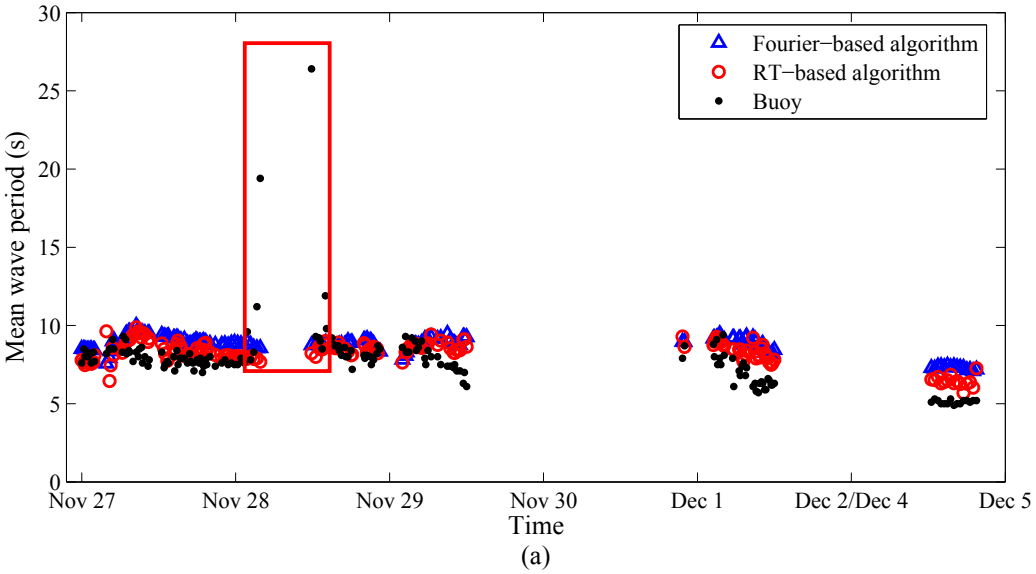
Fourier−based algorithm
RT−based algorithm
Buoy
Mean wave period (s)
0
5
10
15
20
25
30
Nov 27
Nov 28
Nov 29
Nov 30
Dec 1
Dec 2/Dec 4
Dec 5
Time

(a)

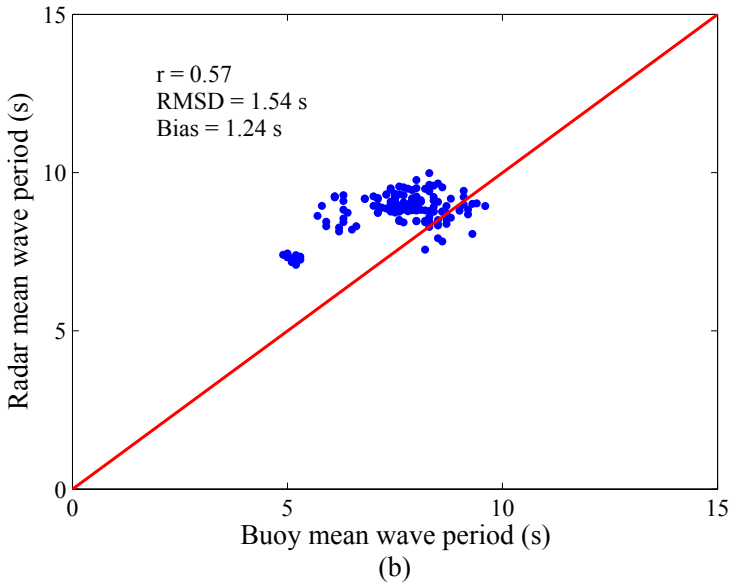
r = 0.57
RMSD = 1.54 s
Bias = 1.24 s
Radar mean wave period (s)
0
5
10
15
Buoy mean wave period (s)

(b)

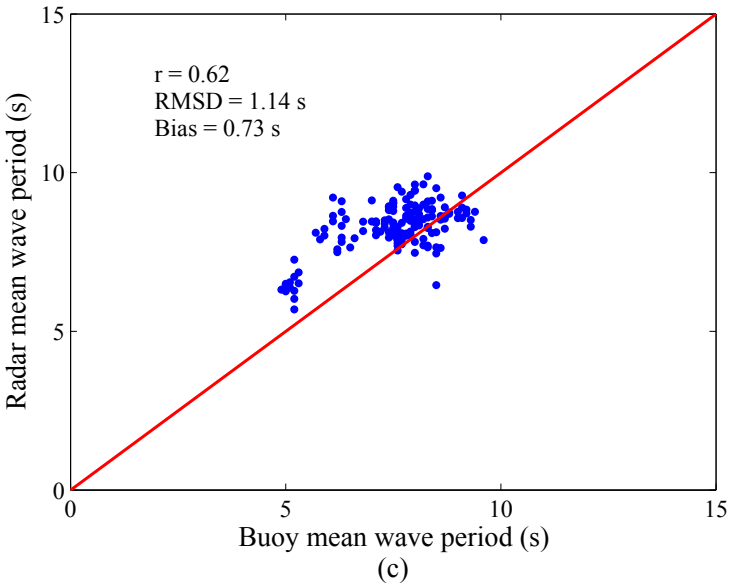

Fig. 6.7 (a) Comparison of time sequences of mean wave periods estimated from Fourier-based algorithm and RT-based algorithm. (b) Scatter plot of mean wave period estimates from a Fourier-based algorithm. (c) Scatter plot of mean wave period estimates from the RT-based algorithm.

wave period, and mean wave period, respectively. The RT-based algorithm works well mainly because it enables the detection of linear features in a noisy digital image. This is especially suitable for the detection of wave signatures in X-band marine radar images.

6.3 Chapter Summary

In this chapter, a Radon transform based algorithm for estimating wave direction, peak wave period, and mean wave period from X-band marine radar image sequences is proposed. Compared to the traditional Fourier-based algorithm, the estimation results are improved by the proposed algorithm with a reduction in the RMS difference with respect to buoy references of 1.2°, 0.15 s, and 0.40 s, respectively, for wave direction, peak wave period, and mean wave period. These results show promise for the application of the RT to X-band marine radar images for wave parameter retrieval.

Chapter 7

Conclusion

7.1 Summary

In this thesis, new algorithms are presented for the extraction of ocean wind and wave parameters from ship-borne X-band marine radar sea surface images. Wind parameter measurements from rain-contaminated radar data are improved using the proposed ensemble empirical mode decomposition (EEMD)-based algorithms. More robust significant wave height estimates are achieved by the EEMD-based and modified shadowing-based algorithms. Wave direction and periods are estimated by the Radon transform (RT)-based algorithm. The proposed algorithms are validated using radar, anemometer, and buoy data collected in a sea trial off the east coast of Canada in late November and early December, 2008.

Two new schemes, i.e., 1D- and 2D-EEMD-based methods are first proposed to retrieve wind direction from radar data contaminated by rain under low wind speeds. Each rain-contaminated radar image is decomposed into separate intrinsic mode function (IMF) components using 1D- or 2D-EEMD. The standard deviation of one IMF component, or the combination of several IMF components, as a function of azimuth is least-squares fitted to a harmonic function to determine the wind direction. Compared to the spectral-analysis-based method, both the 1D- and 2D-EEMD-based algorithms improve the

wind direction results in rain events under low wind speeds, showing a reduction of 7.4° and 8.7°, respectively, in the root-mean-square (RMS) difference with respect to the anemometer measurements. The reasons for the improvements lie in the adaptive nature of the EEMD which makes it particularly applicable in the analysis of non-linear and non-stationary data as is the case for the radar data used in this thesis. Instead of using a fixed wavenumber range of [0.01, 0.2] as in the spectral-analysis-based method, EEMD decomposes data adaptively into different IMF components and a residual. Rain contamination is mostly retained in the residual, and the IMF components which contain wind-induced wave signatures are used for wind direction estimation.

Next, wind direction and speed are retrieved from both rain-free and rain-contaminated radar data using EEMD incorporating normalization. A data control strategy is proposed to separate rain-free and rain-contaminated data and to separate high-wind-speed and low-wind-speed data. EEMD is applied to each radar image to obtain several IMFs and a residual. A normalization scheme is applied to the first IMF to obtain its amplitude modulation (AM) part. Based on curve-fitting a harmonic function, for the rain-free and high-wind-speed rain-contaminated data, wind direction is determined from the residual, while for the low-wind-speed rain-contaminated data, wind direction is determined from the AM part of the first IMF. Wind speed is determined from a combination of the residual and the AM part of the first IMF for both rain-free and rain-contaminated data using a logarithmic relationship. For wind direction estimation, it is found that compared to the spectral-analysis-based method, the wind direction results are similar for rain-free data but significantly improved for rain-contaminated data by the proposed method with a reduction of about 4.9° in the RMS difference. For wind speed estimation, the results are improved for both rain-free and rain-contaminated data using the proposed method with reductions of about 0.11 m/s and 0.51 m/s, respectively, in the RMS differences. Again, the superior results can be explained from the application of the EEMD. The first IMF and residual that are adaptively decomposed from the EEMD, representing the wind-induced small-scale wave signatures and overall image intensity, respectively,

are employed instead of the fixed wavenumber range of [0.01, 0.2] and 0 as in the spectral-analysis-based method.

Then, significant wave height, H_S, is estimated using the novel EEMD-based and the modified shadowing-based algorithms. In the EEMD-based algorithm, the data sequence in each radial direction of a radar sub-image is decomposed by the EEMD into several IMFs. The normalization scheme is then applied to the IMFs to obtain their AM parts. The sum of the AM parts from the second to the fifth IMFs is used to estimate the H_S by curve-fitting a linear model. In the modified shadowing-based algorithm, modifications including selecting a subarea along the upwind direction and smoothing the edge pixel intensity histogram are made to the original shadowing-based algorithm. An inter-comparison shows that the proposed EEMD-based and modified shadowing-based algorithms outperform the SNR-based method with improvements of about 0.42 m and 0.30 m, respectively, in the RMS difference with respect to the buoy reference. The traditional SNR-based method requires an empirical modulation transfer function (MTF), which is influenced by many factors including surrounding environmental conditions and radar set-up. Such an MTF may introduce inaccuracy in H_S estimation, especially for a ship-borne radar. The proposed algorithms, however, avoid the use of the MTF and produce robust results.

Finally, an algorithm based on Radon transform (RT) for estimating wave direction, peak wave period, and mean wave period is proposed. An initial guess of wave direction is first estimated from the first image of an image sequence by using the RT. Then, by using the RT again, sub-images located in the initial guess of wave direction from each image of an image sequence are used to determine wave parameters. Compared to the traditional Fourier-based algorithm, the estimation results are improved by the proposed RT-based algorithm with a reduction of 1.2°, 0.15 s, and 0.40 s, respectively, for wave direction, peak wave period, and mean wave period, in the RMS difference with respect to buoy references. The results show the promise of the application of RT to X-band marine radar images for wave parameters retrieval. This is due to the properties of the

RT which make it useful in detecting linear features from noisy images such as are used in this thesis.

7.2 Suggestions for Future Work

It should be noted that, during most of the data collection period, the area was dominated by dual-mode (wind and swell) sea. The performance of the proposed algorithms should be further investigated under more general wind and wave conditions. Furthermore, the algorithms should be further tested using data collected from a coastal installation for which the influence of platform motion on both radar and anemometer measurements will not be an issue. In addition, the dependency of the proposed algorithms on radar parameters such as range resolution and antenna beam width should be investigated. It should also be noted that the radar data used in this work do not contain targets such as islands or other ships. If such targets exist in the radar images, the proposed algorithms need to be modified to detect the targets and eliminate their effects.

Based on the data used in this work, for the wind direction estimation from rain-contaminated radar data under low wind speeds, the third IMF component generates the best result for the 1D-EEMD-based algorithm, but the first IMF component produces the best result for the 2D-EEMD-based algorithm. As with any experimentally deduced results, it will be useful to further validate these observations with more extensive and varied datasets. Since wind-induced wave signatures are mainly contained in the first several IMF components, whether only one or a combination of such IMF components should be used requires further investigation. While these wind direction results are encouraging, the computational costs for the EEMD-based algorithms are expensive, and their computational complexity requires further investigation. For the wind direction and speed estimation from both rain-free and rain-contaminated radar data, wind direction retrieval in the case of rain contamination existing in the whole radar image needs to be further analyzed by seeking a method that can better identify the wind-induced wave

signature from such data. The accuracy of wind speed estimation in low-wind-speed rain cases needs to be further improved. In addition, the effect of rain rates on radar data is worth investigating.

For wave parameter measurements, the proposed algorithms are applied to rain-free radar data only. Future work should focus on extending these algorithms to rain-contaminated radar data. For the shadowing-based algorithm, rain leads to wave height underestimation, and low wind speed results in wave height overestimation. Thus, further image processing efforts are required to address these concerns. Furthermore, the theoretical limitations (minimum wind, minimum wave height, antenna height, etc.) of the algorithms still need to be investigated. Shadowing modulation in the radar imaging mechanism may be further investigated, and the information from sea surface slopes that may be obtained from the radar backscattering model based on shadowing may be involved in the wave height estimation.

To date, various remote sensing technologies other than marine radar have been used for ocean wind and wave parameter estimation. These include synthetic aperture radar (SAR), high frequency (HF) radar, and S-band radar. Compared to SAR images, X-band marine radar images contain not only spatial information but also temporal evolution of the sea surface, which enables unambiguous directional wave spectrum estimation. Compared to HF radar, the cost of deployment and maintenance of X-band radar is low, and the compactness of the radar allows it to be easily installed on off-shore (stationary or moving) platforms. While, because its wavelength is longer than that of X-band radar, S-band works well for sea surface observation under rain conditions, it provides a coarser resolution and can underestimate high-frequency wave components. Moreover, its larger size also makes it inconvenient for ship-borne applications. More recently, coherent radar has become of interest in the ocean remote sensing community. This is because of its potential to be used in the estimation of wave height without requiring calibration using external sensors since it preserves the phase information of the returned signal. However, the phase information provided by the coherent radar can also increase the cost. Thus,

if robust techniques for rain contamination mitigation and calibration-free wave height estimation are improved for X-band marine radar, the utility of such radars for ocean observation will continue to be enhanced.

References

[1] B. I. Moat, M. J. Yelland, R. W. Pascal, and A. F. Molland, “The effect of ship shape and anemometer location on wind speed measurements obtained from ships," in *Proc. Int. Conf. Marine Comput. Fluid Dynam.*, Southampton, U.K., Mar. 2005, pp. 133–139.

[2] K. G. Hessner, J. C. Nieto-Borge, and P. S. Bell, “Nautical radar measurements in Europe: applications of WaMoS II as a sensor for sea state, current and bathymetry," *Remote Sens. European Seas.*, pp. 435-446, 2008.

[3] G. Engen and H. Johnsen, “SAR-ocean wave inversion using image cross spectra," *IEEE Trans. Geosci. Remote Sens.*, vol. 33, no. 4, pp. 1047-1056, Jul. 1995.

[4] S. Lehner, J. Schulz-Stellenfleth, B. Schattler, H. Breit, and J. Horstmann, “Wind and wave measurements using complex ERS-2 SAR wave mode data," *IEEE Trans. Geosci. Remote Sens.*, vol. 38, no. 5, pp. 2246-2257, Sep. 2000.

[5] H. Lin, Q. Xu, and Q. Zheng, “An overview on SAR measurements of sea surface wind," *Progr. Natural Sci.*, vol. 18, no. 8, pp. 913-919, Aug. 2008.

[6] B. J. Lipa, D. E. Barrick, J. Isaacson, and P. M. Lill, “CODAR wave measurements from a North Sea semisubmersible," *IEEE J. Ocean. Eng.*, vol. 15, no. 2, pp. 119-125, Apr. 1990.

[7] W. Huang, S. Wu, E. W. Gill, B. Wen, and J. Hou, “HF radar wave and wind measurement over the Eastern China Sea," *IEEE Trans. Geosci. Remote Sens.*, vol. 40, no. 9, pp. 1950-1955, Sep. 2002.

[8] L. R. Wyatt, J. J. Green, A. Middleditch, M. D. Moorhead, J. Howarth, M. Holt, and S. Keogh, “Operational wave, current, and wind measurements with the Pisces HF radar," *IEEE J. Ocean. Eng.*, vol. 31, no. 4, pp. 819-834, Oct. 2006.

[9] I. R. Young, W. Rosenthal, and F. Ziemer, “A three-dimensional analysis of marine radar images for the determination of ocean wave directionality and surface currents," *J. Geophy. Res.*, vol. 90, no. C1, pp. 1049-1059, Jan. 1985.

[10] J. C. Nieto-Borge, G. Rodriguez, K. Hessner, and P. Izquierdo, “Inversion of marine radar images for surface wave analysis," *J. Atmos. Ocean. Technol.*, vol. 21, no. 8, pp. 1291-1300, Aug. 2004.

[11] J. C. Nieto-Borge and C. Guedes, “Analysis of directional wave fields using X-band navigation radar," *Coastal Eng.*, vol. 40, no. 4, pp. 375-391, Jul. 2000.

[12] P. H. Y. Lee, J. D. Barter, E. Caponi, M. Caponi, C. L. Hindman, B. M. Lake, and H. Rungaldier, “Wind-speed dependence of small-grazing-angle microwave backscatter from sea surfaces," *IEEE Trans. Antennas Propag.*, vol. 44, no. 3, pp. 333-340, Mar. 1996.

[13] D. B. Trizna and D. J. Carlson, “Studies of dual polarized low grazing angle radar sea scatter in nearshore regions," *IEEE Trans. Geosci. Remote Sens.*, vol. 34, no. 3, pp. 747-757, May 1996.

[14] H. Dankert, J. Horstmann, and W. Rosenthal, “Ocean wind fields retrieved from radar-image sequences," *J. Geophys. Res., Oceans*, vol. 108, no. C11, pp. 3353-3362, Nov. 2003.

[15] B. Lund, H. C. Graber, and R. Romeiser, “Wind retrieval from shipborne nautical X-band radar data," *IEEE Trans. Geosci. Remote Sens.*, vol. 50, no. 10, pp. 3800-3811, Oct. 2012.

[16] R. Vicen-Bueno, J. Horstmann, E. Terril, T. De Paolo, and J. Dannenberg, “Real-time ocean wind vector retrieval from marine radar image sequences acquired at grazing angle," *J. Atmos. Ocean. Technol.*, vol. 30, no. 1, pp. 127-139, Jan. 2013.

[17] Y. Liu, W. Huang, E. W. Gill, D. K. Peters, and R. Vicen-Bueno, “Comparison of algorithms for wind parameters extraction from shipborne X-band marine radar images," *IEEE J. Sel. Topics Appl. Earth Observ. Remote Sens.*, vol. 8, no. 2, pp. 896-906, Feb. 2015.

[18] Y. Wang and W. Huang, “An algorithm for wind direction retrieval from X-band marine radar images," *IEEE Geosci. Remote Sens. Lett.*, vol. 13, no. 2, pp. 252-256, Feb. 2016.

[19] W. Huang and Y. Wang, “A spectra-analysis-based algorithm for wind speed estimation from X-band nautical radar images," *IEEE Geosci. Remote Sens. Lett.*, vol. 13, no. 5, pp. 701-705, May 2016.

[20] C. M. Senet, J. Seemann, and F. Ziemer, “The near-surface current velocity determined from image sequences of the sea surface," *IEEE Trans. Geosci. Remote Sens.*, vol. 39, no. 3, pp. 492-505, Mar. 2001.

[21] K. Hessner and P. S. Bell, “High resolution current & bathymetry determined by nautical X-band radar in shallow waters," in *Proc. MTS/IEEE Oceans*, Bremen, Germany, May 2009.

[22] F. Serafino, C. Lugni and F. Soldovieri, “A novel strategy for the surface current determination from marine X-band radar data," *IEEE Geosci. Remote Sens. Lett.*, vol. 7, no. 2, pp. 231-235, Apr. 2010.

[23] W. Huang, R. Carrasco, C. Shen, E. W. Gill, and J. Horstmann, “Surface current measurements using X-band marine radar with vertical polarization," *IEEE Trans. Geosci. Remote Sens.*, vol. 54, no. 5, pp. 2988-2997, May. 2016.

[24] J. C. Nieto-Borge, K. Hessner, P. Jarabo-Amores, and D. de la Mata-Moya, “Signal-to-noise ratio analysis to estimate ocean wave heights from X-band marine radar image time series," *IET Radar Sonar Navig.*, vol. 2, no. 1, pp. 35-41, 2008.

[25] R. Gangeskar, “An algorithm for estimation of wave height from shadowing in X-band radar sea surface images," *IEEE Trans. Geosci. Remote Sens.*, vol. 52, no. 6, pp. 3373-3381, Jun. 2014.

[26] Z. Chen, Y. He, B. Zhang, Z. Qiu, and B. Yin, “A new algorithm to retrieve wave parameters from marine X-band radar image sequences," *IEEE Trans. Geosci. Remote Sens.*, vol. 52, no. 7, pp. 4083-4091, Jul. 2014.

[27] J. An, W. Huang, and E. W. Gill, “A self-adaptive wavelet-based algorithm for wave measurement using nautical radar," *IEEE Trans. Geosci. Remote Sens.*, vol. 53, no. 1, pp. 567-577, Jan. 2015.

[28] X. Liu, W. Huang, and E. W. Gill, “Comparison of wave height measurement algorithms for ship-borne X-band nautical radar," *Can. J. Remote Sens.*, vol. 42, no. 4, pp. 343-353, Apr. 2016.

[29] C. Craeye, P. W. Sobieski, L. F. Bliven, and A. Guissard, “Ring-waves generated by water drops impacting on water surfaces at rest," *IEEE J. Ocean. Eng.*, vol. 24, no. 3, pp. 323-332, Jul. 1999.

[30] N. Braun, M. Gade, and P. A. Lange, “The effect of artificial rain on wave spectra and multi-polarisation X band radar backscatter," *Int. J. Remote Sens.*, vol. 23, no. 20, pp. 4305-4323, Oct. 2002.

[31] J. Tournadre and Y. Quilfen, “Impact of rain cell on scatterometer data: 1. Theory and modeling," *J. Geophys. Res.*, vol. 108, no. C7, pp. 18-1-18-14, Jul. 2003.

[32] N. E. Huang, Z. Shen, S. R. Long, M. C. Wu, H. H. Shih, Q. Zheng, N. Yen, C. C. Tung, and H. H. Liu, “The empirical mode decomposition and the Hilbert spectrum for nonlinear and non-stationary time series analysis," *Proc. Roy. Soc. London A*, vol. 454, no. 1971, pp. 903-995, Mar. 1998.

[33] N. E. Huang, Z. Shen, and S. R. Long, “A new view of nonlinear water waves: the Hilbert spectrum," *Ann. Rev. Fluid Mech.*, vol. 31, pp. 417-457, Jan. 1999.

[34] Z. Wu and N. E. Huang, “Ensemble empirical mode decomposition: a noise-assisted data analysis method," *Adv. Adapt. Data Anal.*, vol. 1, no. 1, pp. 1-41, Jan. 2009.

[35] Z. Wu, N. E. Huang, and X. Chen, “The multi-dimensional ensemble empirical mode decomposition method," *Adv. Adapt. Data Anal.*, vol. 1, no. 3, pp. 339-372, Jul. 2009.

[36] N. E. Huang, Z. Wu, S. R. Long, K. C. Arnold, X. Chen, and K. Blank, “On instantaneous frequency," *Adv. Adapt. Data Anal.*, vol. 1, no. 2, pp. 177-229, Apr. 2009.

[37] P. Izquierdo, C. Guedes-Soares, J. C. Nieto-Borge, and G. R. Rodriguez, “A comparison of sea-state parameters from nautical radar images and buoy data," *Ocean Eng.*, vol. 31, no. 17-18, pp. 2209-2225, Dec. 2004.

[38] L. Cui, Y. He, H. Shen, and H. Lu, “Measurements of ocean wave and current field using dual polarized X-band radar," *Chin. J. Oceanol. Limnol.*, vol. 28, no. 5, pp 1021-1028, Sep. 2010.

[39] J. C. Nieto-Borge, K. Reichert, and J. Dittmer, “Use of nautical radar as a wave monitoring instrument," *Coastal Eng.*, vol. 37, no. 3-4, pp. 331-342, Aug. 1999.

[40] L. M. Murphy, “Linear feature detection and enhancement in noisy images via the Radon transform," *Pattern Recognit. Lett.*, vol. 4, no. 4, pp. 279-284, Sep. 1986.

[41] A. C. Copeland, G. Ravichandran, and M. M. Trivedi, “Localized Radon transform-based detection of ship wakes in SAR images," *IEEE Trans. Geosci. Remote Sens.*, vol. 33, no. 1, pp. 35-45, Jan. 1995.

[42] V. Onana, E. Trouve, G. Mauris, J. P. Rudant, and E. Tonye, “Detection of linear features in synthetic-aperture radar images by use of the localized Radon transform and prior information," *Appl. Opt.*, vol. 43, pp. 264-273, Jan. 2004.

[43] R. J. Ramos, B. Lund, and H. C. Graber, “Determination of internal wave properties from X-band radar observations," *Ocean Eng.*, vol. 36, no. 14, pp. 1039-1047, Oct. 2009.

[44] B. Lund, H. C. Graber, J. Xue, and R. Romeiser, “Analysis of internal wave signatures in marine radar data," *IEEE Trans. Geosci. Remote Sens.*, vol. 51, no. 9, pp. 4840-4852, Sep. 2013.

[45] L. Cui, “Study on remote sensing mechanism and retrieval method of ocean wave and current with X-band radar," Ph.D. dissertation, Inst. Oceanol., Chin. Acad. Sci., Qingdao, Shandong, China, 2010.

[46] W. Alpers and K. Hasselmann, “Spectral signal to clutter and thermal noise properties of ocean wave imaging synthetic aperture radars," *Int. J. Remote Sens.*, vol. 3, no. 4, pp. 423-446, Jan. 1982.

[47] F. Ziemer and J. Dittmer, “A system to monitor ocean wave fields," in *Proc. IEEE Oceans*, Brest, France, Sep. 1994.

[48] J. C. Nieto-Borge, K. Hessner, and K. Reichert, “Estimation of the significant wave height with X-band nautical radars," in *Proc. 18th Intern. Conf. Offshore Mech. Arctic Eng.*, St. John’s, NL, Canada, Jul. 1999.

[49] E. M. Thornhill and D. C. Stredulinsky, “Real time local sea state measurement using wave radar and ship motions," in *Proc. AGM Conf. SNAME*, vol. 118, pp. 248-259, Bellevue, WA, USA, Jan. 2010.

[50] D. C. Stredulinsky and E. M. Thornhill, “Ship motion and wave radar data fusion for shipboard wave measurement," *J. Ship Res.*, vol. 55, no. 2, pp. 73-85, Jun. 2011.

[51] J. Horstmann, J. C. Nieto-Borge, J. Seemann, R. Carrasco, and B. Lund, “Wind, wave, and current retrieval utilizing X-band marine radars," in *Coastal Ocean Observing Systems: Advances and Syntheses*, 1st ed. London, U.K.: Academic, 2015, ch. 16, pp. 281-304.

[52] H. Hatten, J. Seemann, J. Horstmann, and F. Ziemer, “Azimuthal dependence of the radar cross section and the spectral background noise of a nautical radar at grazing incidence," in *Proc. Geosci. Remote Sens. Symp.*, vol. 5, pp. 2490-2492, Seattle, WA, USA, Jul. 1998.

[53] J. Horstmann, W. Koch, S. Lehner, and R. Tonboe, “Ocean winds from RADARSAT-1 ScanSAR," *Can. J. Remote Sens.*, vol. 28, no. 3, pp. 524-533, Jun. 2002.

[54] W. Koch, “Directional analysis of SAR images aiming at wind direction," *IEEE Trans. Geosci. Remote Sens.*, vol. 42, no. 4, pp. 702-710, Apr. 2004.

[55] H. Dankert, J. Horstmann, and W. Rosenthal, “Wind- and wave-field measurements using marine X-band radar-image sequences," *IEEE J. Ocean. Eng.*, vol. 30, no. 3, pp. 534-542, Jul. 2005.

[56] H. Dankert and J. Horstmann, “A marine radar wind sensor," *J. Atmos. Ocean. Technol.*, vol. 24, no. 9, pp. 1629-1642, Sep. 2007.

[57] H. Dankert, J. Horstmann, and W. Rosenthal, “Ocean surface winds retrieved from marine radar-image sequences," in *Proc. Int. Geosci. Remote Sens. Symp.*, Anchorage, Alaska, Sep. 2004, pp. 1903-1906.

[58] B. Jähne, H. Haußecker, and Peter Geißler, *Handbook of Computer Vision and Applications*, Academic Press, 1999.

[59] W. Huang and E. W. Gill, “Ocean remote sensing using X-band shipborne nautical radar—Applications in eastern Canada," in *Coastal Ocean Observing Systems: Advances and Syntheses*, 1st ed. London, U.K.: Academic, 2015, ch. 14, pp. 248-264.

[60] W. Huang, Y. Liu, and E. W. Gill, “Texture-analysis-incorporated wind parameters extraction from rain-contaminated X-band nautical radar images," *Remote Sens.*, vol. 9, no. 2, Feb. 2017.

[61] Z. Chen, Y. He, B. Zhang, and Z. Qiu, “Determination of nearshore sea surface wind vector from marine X-band radar images," *Ocean Eng.*, vol. 96, pp. 79-85, Mar. 2015.

[62] P. Izquierdo and C. G. Soares, “Analysis of sea waves and wind from x-band radar," *Ocean Eng.*, vol. 32, no. 11-12, pp. 1404-1419, Aug. 2005.

[63] B. Lund, C. O. Collins, H. C. Graber, E. Terrill, and T. H. C. Herbers, “Marine radar ocean wave retrieval’s dependency on range and azimuth," *Ocean Dyn.*, vol. 64, no. 7, pp. 999-1018, Jul. 2014.

[64] R. Vicen-Bueno, C. Lido-Muela, and J. C. Nieto-Borge, “Estimate of significant wave height from non-coherent marine radar images by multilayer perceptrons," *EURASIP J. Adv. Signal Process.*, vol. 2012, no. 84, pp. 1-20, Dec. 2012.

[65] W. Huang, E. W. Gill, and J. An, “Iterative least-squares-based wave measurement using X-band nautical radar," *IET Radar Sonar Navig.*, vol. 8, no. 8, pp. 853-863, Oct. 2014.

[66] W. Huang and E. W. Gill, “Surface current measurement under low sea state using dual polarized X-band nautical radar," *IEEE J. Sel. Topics Appl. Earth Observ. Remote Sens.*, vol. 5, no. 6, pp. 1868-1873, Dec. 2012.

[67] Z. Chen, B. Zhang, Y. He, Z. Qiu, and P. William, “A new modulation transfer function for ocean wave spectra retrieval from X-band marine radar imagery," *Chin. J. Oceanol. Limnol.*, vol. 33, no. 5, pp. 1132-1141, Sep. 2015.

[68] J. Qiu, B. Zhang, Z. Chen, and Y. He, “A new modulation transfer function with range and azimuth dependence for ocean wave spectra retrieval from X-band marine radar observations," *IEEE Geosci. Remote Sens. Lett.*, vol. 14, no. 8, pp. 1373-1377, Aug. 2017.

[69] *The Wave and Surface Current Monitoring System (WaMoS) II Operating Manual*, 4 ed.; OceanWaves GmbH: Luneburg, Germany, May, 2012.

[70] A. Al-Habashneh, C. Moloney, E. W. Gill, and W. Huang, “An adaptive method of wave spectrum estimation using X-band nautical radar," *Remote Sens.*, vol. 7, no. 12, pp. 16537-16554, Dec. 2015.

[71] L. Wang, X. Wu, X. Yue, K. Ma and Y. Tian, “A novel algorithm in estimating signal-to-noise ratio for ocean wave height inversion from X-band radar images," *IEEE Geosci. Remote Sens. Lett.*, vol. 13, no. 3, pp. 344-348, Mar. 2016.

[72] L. Wang, X. Wu, K. Ma, Y. Tian, and Y. Fei, “Elimination of the impact of vessels on ocean wave height inversion with X-band wave monitoring radar," *Chin. J. Oceanol. Limnol.*, vol. 34, no. 5, pp. 1114-1121, Sep. 2016.

[73] L. Z. H. Chuang, L. C.Wu, D. J. Doong, and C. C. Kao, “Two-dimensional continuous wavelet transform of simulated spatial images of waves on a slowly varying topography," *Ocean Eng.*, vol. 35, no. 10, pp. 1039-1051, Jul. 2008.

[74] L. C. Wu, L. Z. H. Chuang, D. J. Doong, and C. C. Kao, “Ocean remotely sensed image analysis using two-dimensional continuous wavelet transform," *Int. J. Remote Sens.*, vol. 32, no. 23, pp. 8779-8798, Dec. 2011.

[75] J. P. Antoine, R. Murenzi, P. Vandergheynst, and S. T. Ali, *Two Dimensional Wavelets and Their Relatives.* Cambridge, U.K.: Cambridge Univ. Press, 2004.

[76] J. An, W. Huang, and E. Gill, “2-D continuous wavelet based algorithm for extracting wave information from nautical radar images," in *Proc. IEEE RadarCon*, Ottawa, ON, Canada, May 2013, pp. 1–6.

[77] K. Ma, X. Wu, X. Yue, L. Wang, and J. Liu, “Array beamforming algorithm for estimating waves and currents from marine X-band radar image sequences," *IEEE Trans. Geosci. Remote Sens.*, vol. 55, no. 3, pp. 1262-1272, Mar. 2017.

[78] B. D. Van Veen and K. M. Buckley, “Beamforming: A versatile approach to spatial filtering," *IEEE ASSP Mag.*, vol. 5, no. 2, pp. 4-24, Apr. 1998.

[79] X. Huang, Z. Wang, and G. Hou, “New method of estimation of phase, amplitude, and frequency based on all phase FFT spectrum analysis," in *Proc. Int. Symp. Intell. Signal Process. Commun. Syst. (ISPACS)*, pp. 284-287, Dec. 2007.

[80] M. D. Henschel, J. R. Buckley, and F. W. Dobson, “Estimates of wave height from low incidence angle sea clutter," in *Proc. ICWHF*, Banff, AB, Canada, 1995.

[81] J. R. Buckley and J. Aler, “Estimation of ocean wave height from grazing incidence microwave backscatter," in *Proc. IEEE IGARSS*, Singapore, 1997, vol. 2, pp. 1015-1017.

[82] L. B. Wetzel, “Electromagnetic scattering from the sea at low grazing angles," in Surface Waves and Fluxes. Boston, MA, USA: Kluwer, 1990, pp. 109-172.

[83] J. R. Buckley and J. Aler, “Enhancements in the determination of ocean surface wave height from grazing incidence microwave backscatter," in *Proc. IEEE IGARSS*, Seattle, WA, USA, 1998, vol. 5, pp. 2487-2489.

[84] R. Gangeskar, “Wave height derived by texture analysis of X-band radar sea surface images," in *Proc. IEEE IGARSS*, Honolulu, HI, USA, 2000, vol. 7, pp. 2952-2959.

[85] R. Gangeskar, “An adaptive method for estimation of wave height based on statistics of sea surface images," in *Proc. IEEE IGARSS*, Honolulu, HI, USA, 2000, vol. 1, pp. 255-259.

[86] H. Dankert and W. Rosenthal, “Ocean surface determination from X-band radar-image sequences," *J. Geophys. Res., Oceans*, vol. 109, no. C4, pp. C04016, Apr. 2004.

[87] W. K. Pratt, *Digital Image Processing.* Hoboken, NJ, USA: Wiley, 1991, pp. 497-518.

[88] B. G. Smith, “Geometric shadowing of a random rough surface," *IEEE Trans. Antennas Propag.*, vol. AP-15, no. 5, pp. 668-671, 1967.

[89] J. C. Lagarias, J. A. Reeds, M. H. Wright, and P. E. Wright, “Convergence properties of the Nelder-Mead simplex method in low dimensions," *SIAMJ. Optim.*, vol. 9, no. 1, pp. 112-147, 1998.

[90] Y. Wei, Z. Lu, G. Pian, and H. Liu, “Wave height estimation from shadowing based on the acquired X-band marine radar images in coastal area," *Remote Sens.*, vol. 9, no. 8, pp. 859-878, Aug. 2017.

[91] S. Salcedo-Sanz, J. C. Nieto-Borge, L. Carro-Calvo, L. Cuadra, K. Hessner, and E. Alexandre, “Significant wave height estimation using SVR algorithms and shadowing information from simulated and real measured X-band radar images of the sea surface," *Ocean Eng.*, vol. 101, pp. 244-253, Jun. 2015.

[92] A. J. Smola and B. Scholkopt, “A tutorial on support vector regression," *Stat. Comput.*, vol. 14,, no. 3, pp. 199-222, Aug. 2004.

[93] H. Björnsson and S. A. Venegas, “A manual for EOF and SVD analyses of climatic data," McGill Univ., Montreal, QC, Canada, CCGCR Rep. 97-1, 1997.

[94] A. H. Monahan, J. C. Fyfe, M. H. P. Ambaum, D. B. Stephenson, and G. R. North, “Empirical orthogonal functions: the medium is the message," *J. Clim.*, vol. 22, no. 24, pp. 6501–6514, Dec. 2009.

[95] D. Mulally and H. W. Paik, “Power spectral density estimation simulation using the maximum entropy method," in *Proc. 36th Midwest Symp. Circuits Syst.*, Detroit, MI, USA, 1993, vol. 1, pp. 578–581.

[96] T. Yu, W. Xie, and S. Zhang, “Improved algorithm for estimation of significant wave height from X-band radar image sequences," *J. Appl. Remote Sens.*, vol. 10, no. 4, pp. 1-12, Nov. 2016.

[97] S. Zhang, Z. Song, and Y. Li, “An advanced inversion algorithm for significant wave height estimation based on random field," *Ocean Eng.*, vol. 127, pp. 298-304, Nov. 2016.

[98] Z. Chen, Y. He, and B. Zhang, “An automatic algorithm to retrieve wave height from X-band marine radar image sequence," *IEEE Trans. Geosci. Remote Sens.*, vol. 55, no. 9, pp. 5084-5092, Sep. 2017.

[99] M. S. Longuet-Higgins, “On the joint distribution of wave periods and amplitudes in a random wave field," *Proc. Roy. Soc. London Ser. A*, vol. 389,, no. 1797, pp. 241-258, 1983.

[100] F. Sun, “The joint distribution of ocean wave periods and ocean wave heights," (Chinese), *Acta Oceanol. Sinica*, vol. 10, no. 1, pp. 10-15, 1988.

[101] R. Carrasco, J. Horstmann, and J. Seemann, “Significant wave height measured by coherent X-band radar," *IEEE Trans. Geosci. Remote Sens.*, vol. 55, no. 9, pp. 5355-5365, Sep. 2017.

[102] D. R. Lyzenga and D. T. Walker, “A simple model for marine radar images of the ocean surface," *IEEE Geosci. Remote Sens. Lett.*, vol. 12, no. 12, pp. 2389-2392, Dec. 2015.

[103] H. Y. Cheng and H. Chien, “Implementation of S-band marine radar for surface wave measurement under precipitation," *Remote Sens. Environ.*, vol. 188, pp. 85-94, Jan. 2017.

[104] F. Xu, X. Li, P. Wang, J. Yang, W. G. Pichel, and Y. Q Jin, “A backscattering model of rainfall over rough sea surface for synthetic aperture radar," *IEEE Trans. Geosci. Remote Sens.*, vol. 53, no. 6, pp. 3042-3054, Jun. 2015.

[105] X. Liu, Q. Zheng, R. Liu, M. A. Sletten, and J. H. Duncan, “A model of radar backscatter of rain-generated stalks on the ocean surface," *IEEE Trans. Geosci. Remote Sens.*, vol. 55, no. 2, pp. 767-776, Feb. 2017.

[106] Y. Wang, C. Yeh, H. V. Young, K. Hu, and M. Lo, “On the computational complexity of the empirical mode decomposition algorithm," *Physica A*, vol. 400, pp. 159-167, Jan. 2014.

[107] E. P. Carratelli, F. Dentale, and F. Reale, “Numerical pseudo-random simulation of SAR sea and wind response," in *Proc. SeaSAR*, Frascati, Italy, Jan. 2006.

[108] F. Reale, F. Dentale, and E. P. Carratelli, “Numerical simulation of whitecaps and foam effects on satellite altimeter response," *Remote Sens.*, vol. 6, no. 5, pp. 3681-3692, Apr. 2014.

[109] J. Radon, “Über die Bestimmung von Funktionen durch ihre Integralwerte längs gewisser Mannigfaltigkeiten," *Math. Phys. Klasse*, vol. 69, pp. 262-277, Apr. 1917.

[110] P. S. Bell and J. C. Osler, “Mapping bathymetry using X-band marine radar data recorded from a moving vessel," *Ocean Dyn.*, vol. 61, no. 12, pp. 2141-2156, Dec. 2011.